$V_2O_3(0001)/Au(111)$ and $/W(110)$: Growth, Electronic Structure and Adsorption Properties

D i s s e r t a t i o n

zur Erlangung des akademischen Grades

d o c t o r   r e r u m   n a t u r a l i u m

(dr. rer. nat.)

im Fach Physik

eingereicht an der

Mathematisch-Naturwissenschaftlichen Fakultät I

Humboldt-Universität zu Berlin

von

Ingénieure Anne-Claire Dupuis

geboren am 02.11.1974 in Caen(Frankreich)

Präsident der Humboldt-Universität zu Berlin:

Prof. Dr. J. Mlynek

Dekan der Mathematisch-Naturwissenschaftlichen Fakultät I:

Prof. Dr. M. Linscheid

Gutachter: 1. Prof. Dr. Horst Niehus

2. Prof. Dr. Hans-Joachim Freund

3. Prof. Victor E. Henrich

eingereicht am: 19. Juni 2002

Tag der mündlichen Prüfung: 17. Oktober 2002

Another important characteristic of science is its objectivity. It is necessary to look at the results of observation objectively, because you, the experimenter, might like one result better than another. You perform the experiment several times, and because of irregularities, like pieces of dirt falling in, the result varies from time to time. You do not have everything under control. You like the result to be a certain way, so the times it comes out that way, you say, "See, it comes out this particular way." The next time you do the experiment it comes out different. Maybe there was a piece of dirt in it the first time, but you ignore it.

Richard Feynman, *The Meaning of It All*

iv

Acknowledgement

I wish to express my gratitude towards Prof. Hans-Joachim Freund for the opportunity he gave me to pursue this PhD work in his laboratory and especially for the time he took to discuss my results. Many thanks to Prof. Horst Niehus who accepted to be the official director of my thesis. Also to Helmut Kuhlenbeck who supervised this work and gave me his invaluable help with technical problems.

I gratefully acknowledge the cooperation of many members of the Fritz-Haber-Institute with the daily problems with the machine. They include Bettina Tepper, Kai Wolter, Norbert Magg, Thomas Schröder and Ingo Meusel. I was very fortunate to have the support of Bodo Richter during the two weeks spent at Bessy. I would especially like to thank Martin Frank for proof-reading this document.

Scientists I met at conferences provided invaluable help to me. By showing me their interest and encouragement, they allowed me to find new ideas to further develop my work. Thanks to all of them particularly Prof. Victor Henrich and Fabio Finocchi.

I would like to mention music which plays an important part in my life besides physics. I am most indebted to Anne Katrin Ossenkop, my singing teacher, for helping to compensate for the frustration every scientist knows with her positive words relative to my singing.

I wish to thank my friends and family for their words of support and encouragement throughout my 4 years of study.

Diese Arbeit wurde im Zeitraum von Oktober 1998 bis Juni 2002 am Fritz-Haber-Institut der Max-Planck-Gesellschaft, Abteilung Chemische Physik, unter Anleitung von Herrn Prof. Dr. H.-J. Freund erstellt.

Contents

Chapter 1

Introduction

1.1 Motivation

Physics and chemistry of metal oxide surfaces are of great interest because
these systems have such varied properties that they find wide technological
applications. Transition metal oxides exhibit an enormous range of electronic
properties, due to the presence of d electrons, they may be good insulators,
semiconductors, metals or supraconductors. Many compounds show transi-
tions from a metallic to a non-metallic state as a function of temperature
and/or pressure and/or composition. Their optical and magnetic behav-
ior can differ because of their different electronic structure. These different
properties form the basis for many important applications. This range of
properties also constitutes a challenge for the solid state physicist in terms
of scientific understanding.

Vanadium oxides are a good example to demonstrate the complexity of
transition metal oxides. Their complex phase diagram shows the existence of
many stoichiometric compounds like VO, V_2O_3, VO_2 and V_2O_5 (see appendix
A). Most of them undergo a metal-to-insulator transition as function of the
temperature. This property can be used for example for the realization of
temperature sensors. Furthermore, VO_2 and V_2O_5 are widely used catalysts
in industry for oxidation reactions.

The purpose of this work is to study the reactivity of the $V_2O_3(0001)$ surface. It is generally accepted that lower oxidation states of vanadium of the V_2O_5 surface play an important role in the catalytic process, [1, 2]. V_2O_3 has been the object of many theoretical and experimental studies over the last years because of its paramagnetic metallic (PM) to antiferromagnetic insulator (AFI) phase transition at 150K. Up to this date this quite complex transition is still not completely understood.

1.2   Plan

This work is organized as follows.

In **chapter 2**, the most important physical concepts are introduced.

In **chapter 3**, the experimental methods used are explained.

The experimental set-up is presented in **chapter 4**.

As mentioned above, most of the vanadium oxides are insulators below a certain temperature. Therefore, one may have some difficulty to apply electron spectroscopy at low temperatures since the surface then tends to charge. In order to circumvent this problem, one can grow a thin film of the vanadium oxide on a metallic substrate. Three metallic substrates were used for the growth of vanadium oxide: Au(100), Au(111) and W(110). The topic of **chapter 5** is the epitaxial growth of vanadium oxide films on these substrates. There, it is shown how the stoichiometry, the geometric and electronic structures of these films are characterized with spectroscopic methods. This characterization allows one to be certain that the thin film surface presents the same geometric and electronic properties as a single crystal surface. We will show that two terminations of the $V_2O_3(0001)$ surface exist.

Chapter 6 focusses on the electronic structure of $V_2O_3(0001)$ on Au(111) and W(110) probed with UV photoelectron spectroscopy (UPS), x-ray photoelectron spectroscopy (XPS) and near edge x-ray absorption fine structure spectroscopy (NEXAFS). We will show that the electronic structure strongly depends on the surface termination.

Chapter 7 presents the phonon structure of the thin film studied with high resolution electron energy loss spectroscopy (HREELS).

The adsorption properties of H_2O, CO_2 and CO of the $V_2O_3(0001)$ surface for both terminations are studied in **chapter 8, 9** and **10**, respectively. The behavior of the surface upon adsorption is characterized using photoemission and vibration spectroscopy.

Chapter 11 summarizes our principal results and proposes further work on $V_2O_3(0001)$ thin films.

Finally, **appendix A** constitutes a short review of the different vanadium oxides and their crystal structures.

Chapter 2

Physical Concepts

2.1 Heteroepitaxy

2.1.1 Introduction

As already mentioned in the introduction, we want to grow a thin film of vanadium oxide on a metallic substrate in order to be able to apply electron spectroscopy. The ordered growth of material on a substrate of a different nature is called heteroepitaxy. In this section, we would like to present the theory of this process.

2.1.2 Criteria for Good Epitaxy

On the basis of experimental observations of epitaxial growth of ionic crystals one on top of the other, Royer (see [3]) formulated rules for the occurrence of epitaxy. The most important one is maybe: the crystal planes in contact must have close lattice parameters. The accommodation of the lattice misfit results in homogeneous strain (pseudomorphism) or periodic strain (dislocation) [3]. The orientation of the substrate determines the epitaxial orientation ; more exactly the structure and hence the energy of the epitaxial interface plays a significant role [3]. The thermic dilatation and elasticity coefficients of substrate and epitaxial layer also have to be close to assure structural stability of the heterogeneous system. And finally, a good thermal stability is required,

i.e no reaction, alloying and interdiffusion between the compounds should occur.

2.1.3   Growth Modes

One can distinguish three growth modes, the layer or Frank-van der Merwe growth, the island or Volmer-Weber growth and the intermediate "layer plus island" or Stranski-Krastanov growth [4]. In the case of a thermodynamically controlled growth, these distinctions can be understood in terms of relative surface energies, γ_A, $\gamma*$ and γ_B. If the substrate is A and the deposit B, the condition $\gamma_B + \gamma* < \gamma_A$, where $\gamma*$ is the interfacial energy, leads to layer growth. The inverse condition leads to island growth. However, it is often the case that the effective interfacial energy $\gamma*$ increases with thickness of the layer, for example due to strain. This leads to the intermediate growth [4].

2.1.4   Thermodynamic and Kinetic Approaches

When the metal is evaporated onto a substrate under oxygen atmosphere, the epitaxial growth of a metal oxide can be regarded as the reaction:

$$xMe(g) + \frac{y}{2}O_2(g) \rightleftharpoons Me_xO_y(s) \tag{2.1}$$
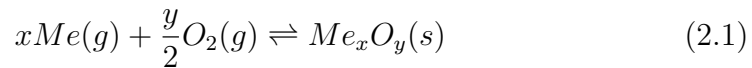
The reaction constant then is $K = \frac{(P_{Me})^x \cdot (P_{O_2})^{y/2}}{a_{Me_xO_y}}$, where P denotes the partial pressure of the corresponding gas and a is the activity of the metal oxide. The difference of free Gibbs energy is $\Delta G = x\mu_{Me} + \frac{y}{2}\mu_{O_2} - \mu_{Me_xO_y} = \Delta G^o + RT \ln K$. The condition for the equilibrium is $\Delta G = 0$ and thus one can determine possible temperature and vapor pressures of metal and oxygen to have epitaxial growth. In most cases, however, growth is a non-equilibrium process. In such a process, one or more steps are rate-limiting. These processes are adsorption and desorption, surface diffusion of adatoms and binding nucleation [3, 4]. The growth rate then corresponds to the difference between the fluxes of adsorbing and desorbing particles. The capture rate of the surface depends on its nature and structure and controls the adsorption. The adatoms diffuse and come together and form nuclei which can

develop into islands when they have reached a critical size [4]. This process controls the desorption.

2.2 Electronic Structure of Transition-Metal Oxides

In this section we present a short review of the different ways to model the electronic structure of transition-metal oxides and how their insulating states can be explained. Since V_2O_3 undergoes a metal-to-insulator transition at 150K, these concepts are of great importance for the understanding of its electronic properties. Furthermore, the changes of the electronic structure at the surface will be introduced. This shall provide insight into the phenomena discussed in chapter 6.

2.2.1 Bulk

From the ionic picture to band theory

Consider a metal oxide Me_xO_y. In a ionic picture it consists of O^{2-} and $Me^{\frac{2y}{x}+}$ ions, see figure 2.1 the example of MgO.

In the gas phase, this ionic charge distribution is not stable and to be stabilized the ions have to be put in a lattice, so that they experience an electrostatic Madelung potential [5, 6]. This depends on summation of long-range Coulomb potentials from the ions of the lattice. Thus the electrons on the anions will experience a positive potential and those on the cations a negative one. Therefore the Madelung potential lowers the anion levels and raises the cation levels [5]. Other effects have to be taken into account for an estimation of the energy levels in the oxide. The first is the electrostatic polarization resulting from the deformation of electron distributions in an electric field. It lowers the energy of empty (metal) levels and raises that of filled (oxygen) levels. The other effect is the bandwidth. It originates from the coupling between the atomic levels of the ions of the lattice. Consider an electron subject to the action of these ions. When the distance between
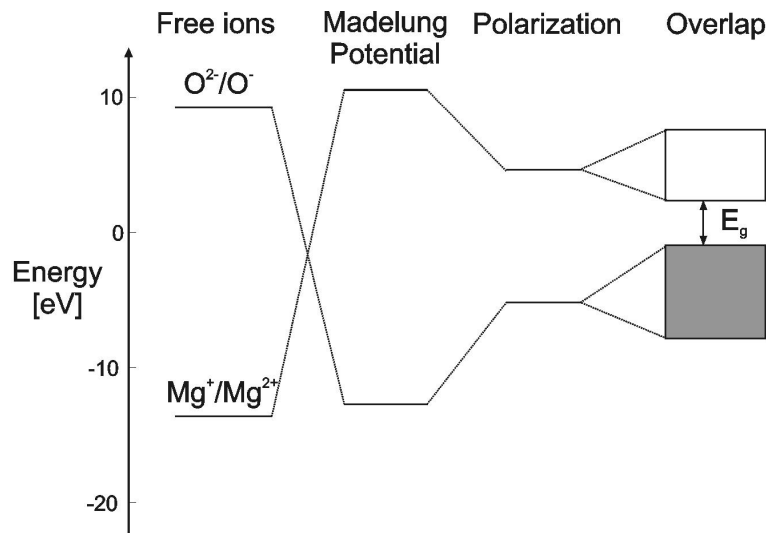
Figure 2.1: Ionic picture to the electronic structure of a metal oxide, for the example MgO. The free ions energies are corrected by the Madelung potential and the electrostatic polarization and give rise to bands by overlap

them is small enough, the electron can pass from one ion to another by the tunnel effect and the degeneracy of the levels is removed, leading to the formation of bands for a very large number of ions [7]. This pure ionic model can be regarded as a qualitative framework and allows one to understand the formation of valence- and conduction-band based on the filled O 2p and on the empty metal valence orbitals respectively. This model works well for the simple non-transition-metal-oxide MgO where the conduction band corresponds to the empty Mg 3s states. In the transition-metal-oxides, however, the valence orbitals are of d symmetry, which leads to some complications.

The d orbitals of transition metals have five-fold degeneracy in the free ions. The ion in a lattice is surrounded by a three-dimensional array of ligands. This gives rise to a new term in the Hamiltonian of one electron on a cation, corresponding to the ligand field. By treating this term as a perturbation , it can be shown that the degeneracy of the d orbitals is removed [8]. The perturbation energy depends on the symmetry of the ligands and is different for each d orbital [8]. This can be viewed as an effect of the different directional properties of the d orbitals that give rise to different
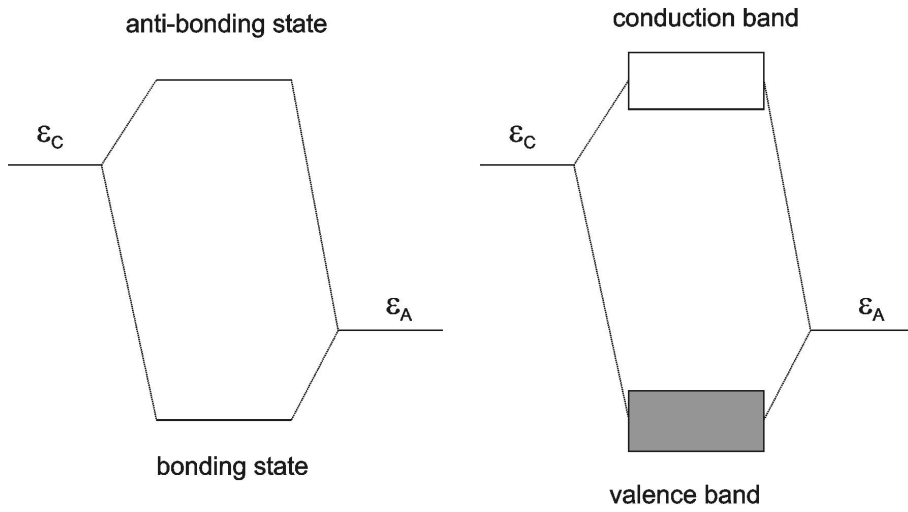
Figure 2.2: Bonding and anti-bonding states of an hetero-polar diatomic molecule (left) and broadening of these states, leading to the formation of the valence and conduction bands in the crystal (right)

bonding interactions with nearby atoms [6]. For a metal cation in a octahedral field, the five-fold degenerate d level splits in a two-fold degenerate (e_g) and a three-fold degenerate (t_{2g}) level. The e_g orbitals have lobes of maximum density pointing directly towards the ligand whereas the t_{2g} orbitals point away. Thus an electron in a e_g orbital experiences a stronger repulsion due to the ligand than when it occupies a t_{2g} orbital and so the e_g orbitals correspond to the higher level [5, 8, 9].

This crystal theory in the ionic picture has to be improved since it is known that the electrons of the central metal ion do drift on to the ligands [9]. This justifies an attempt to explain the electronic structure of transition metal complexes in terms of a molecular orbital (MO) scheme as shown in figure 2.2. In the simplest quantum approach of the case of a diatomic molecule, one can use a one-electron Hamiltonian H and consider a single outer orbital per site, of energy ϵ_A and ϵ_C for the anion and cation, respectively. The atomic orbitals are assumed to be orthogonal and non-degenerate. The resonance (or hopping) integral associated with electron delocalization between neighboring atoms is $\beta = \langle A|H|C \rangle$. The bonding and anti-bonding states of the AC

molecule are represented by the summation of the two atomic orbitals:

$$|\Psi\rangle = x|A\rangle + y|C\rangle \tag{2.2}$$

and their eigenenergies E are [10, 11]:

$$E_{B,AB} = \frac{\epsilon_A + \epsilon_C}{2} \mp \frac{1}{2}\sqrt{(\epsilon_C - \epsilon_A)^2 + 4\beta^2} \tag{2.3}$$

In the bonding state, the anion and cation electron number N_A and N_C respectively are $N_A = 1 + Q$ and $N_C = 1 - Q$, where Q is equal to:

$$Q = \frac{\epsilon_C - \epsilon_A}{\sqrt{(\epsilon_C - \epsilon_A)^2 + 4\beta^2}} \tag{2.4}$$

and determines the ionic charge. $Q = 0$ in the covalent limit (the two electrons have equal probability of being located on each atom) and $Q = 1$ in the ionic limit (the two electrons are located on the anion) [10]. This result can be generalized for a mixed iono-covalent material and one can show that the ratio $(\epsilon_C - \epsilon_A)^2/[(\epsilon_C - \epsilon_A)^2 + 4Z_A\beta^2]$ characterizes its ionicity [10]. We shall assume that the electron, when it is bound to a given ion, has only one possible state, denoted $|\phi_q\rangle$. As for a diatomic molecule, each molecular orbital in the solid is expanded in the atomic orbitals basis set $\{\phi\}$:

$$|\Psi\rangle = \sum c_q|\phi_q\rangle \tag{2.5}$$

The simplest cluster models treat a single metal atom interacting with its surrounding oxygens. There, one considers the possible linear combinations of the oxygen orbitals that have appropriate symmetry to be able to mix with the metal orbitals [5, 9]. Mixing between these oxygen 2p and the metal 3d orbitals produces bonding MOs, localized more on oxygen, and anti-bonding MOs with more metal character. One can improve the MO method by taking mixtures of different MO configurations, chosen to give a better representation of the wave function than a single orbital configuration [5]. This method, called configuration interaction (CI), is widely used to interpret photoemission spectra [12, 13].

We shall now focus on the periodicity of the crystal and thus of the potential created by the ions. As already stated above, an eigenvector of H for

an electron in a periodic array of positive ions can be written as a sum of atomic orbitals, see equation 2.5. The non-diagonal elements of H express the possibility for an electron to move from one ion to another and have already been defined above as $\beta = \langle \phi_q | H | \phi_{q\pm1} \rangle$. Here, we shall take into account only the matrix elements between nearest neighbors. Taking the coefficients in equation 2.5 of the form:

$$c_q = e^{ikqa} \tag{2.6}$$

where a is the lattice parameter and k a constant, one may solve the eigenvalue equation $H|\Psi\rangle = E|\Psi\rangle$ and find:

$$E(k) = E_o + 2\beta \cos ka \tag{2.7}$$

where k is required to belong to the "first Brillouin zone", that is to satisfy $-\frac{\pi}{a} \leq k < +\frac{\pi}{a}$ (two values of k differing by $2\pi/a$ give all the c_q the same value) [7]. Since the state $|\phi_q\rangle$ can be obtained from the state $|\phi_o\rangle$ by a translation of qa, we have for the associated wave functions $\phi_q(x) = \phi_o(x - qa)$. One then finds for the wave function associated with the state $|\Psi\rangle$:

$$\Psi_k(x + a) = e^{ika}\Psi_k(x) \tag{2.8}$$

This is equivalent to:

$$\Psi_k(x) = e^{ikx}u_k(x) \tag{2.9}$$

with $u_k(x + a) = u_k(x)$. This is the Bloch theorem: an eigenvector of the Hamiltonian of an electron in a periodic potential can be written as a function of type 2.9, called a Bloch function [14]. We have so far considered an infinite chain of ions. When one considers a finite linear chain of length L, boundary conditions, called Born-Von Karman conditions, may be applied. They require the wave function to take on the same value at both ends of the chain. This yields $e^{ikL} = 1$ and consequently $k_n = n\frac{2\pi}{L}$ where n is an integer. So the available values for the constant k are quantized and k can be ragarded as a quantum number for crystal orbitals, known as the wavevector. Since L may be very large, one speaks of "pseudo continuum". The above results can be generalized for the three dimensional case. The conditions on k then read:

$$k_{x,y,z} = n_{x,y,z}\frac{2\pi}{L_{x,y,z}} \tag{2.10}$$

The band theory can be connected with the ionic picture, considering that each atomic orbital such as the metal 3d or oxygen 2p, would give one band. The mixing between the orbitals is governed by symmetry constraints and so by the phase factor $c_q = e^{iqka}$ in equation 2.5. Therefore, there are values for k for which the mixing will be large and values for which no mixing occurs. From such simple symmetry considerations, one can deduce the shape of the band-structure E(k) with a basis of two orbitals such as for example Me 3d and O 2p [5, 15]. This is given in the band theory by equation 2.7. From this, one can deduce that the band width is 4β and therefore proportional to the strength of the coupling, as predicted by the simple molecular orbital model. The different bands are separated by regions where no possible value for the energy of the electron exists. These are the so-called forbidden bands or gaps. Within a nearly-free electron model, the E(k) corresponds to:

$$E(k) = V_o + \frac{\hbar^2 k^2}{2m^*} \tag{2.11}$$

This approximation is often valid near the extremum of the band. m^* is the effective mass of the electron in the band and corresponds to the reverse of the bend of the curve (second derivative) [16]. The density of states (DOS) z(E) is defined so that z(E)dE is the number of available states in the energy range (E,E+dE). The number of occupied states in this energy range depends on the occupation probability f(E) of the level E and reads:

$$n(E)dE = z(E)f(E)dE \tag{2.12}$$

The Fermi level is the level for which the occupation probability f(E) is 1/2 and corresponds to the chemical potential [16].

Insulating States

The ionic picture assumes that the electrons are frozen around the ionic cores (localized model) - and thus cannot make any prediction on the electron transport properties - while band theory predicts a metallic state when the Fermi level lies within an allowed band (delocalized model) - a model that in many cases breaks down. In the case of a d^0 compound, the bonding

band with mainly O 2p character is full, while the anti-bonding one is empty. The Fermi level lies between them in the gap and the oxide is an insulator. Both the ionic picture and the band theory are valid. The electronic excitation of lowest energy determines the gap width [10]. In this case, this is a charge-transfer excitation and corresponds to the transfer of an electron from the anion to the cation. The charge-transfer energy is denoted Δ. In a partially occupied shell system, however, the oxide may be insulating though the band theory predicts a metallic state. This is because the representation of the repulsion between electrons by an average effective potential is not a good approximation anymore when electron correlation becomes important. This term describes the way electrons move in order to avoid each other and has to be taken into account especially in very narrow bands. The Hubbard model describes this insulating state introducing the Hubbard energy U. This is the energy U required for the exchange of an electron between two cations, yielding the formation of two bands: the lower and the upper Hubbard sub-bands. The correlation competes with the delocalization due to the interatomic overlap. At a critical value around W (band width) $\sim$ U, the upper and lower states overlap and the gap vanishes [5]. Zaanen et al. have classified the insulators using both parameters Δ and U in a phase diagram [17]. For a Mott-Hubbard insulator where $E_{gap} \propto U$ ($U < \Delta$), both holes and electrons move in d bands and are heavy, while for a charge-transfer insulator with $E_{gap} \propto \Delta$ ($U > \Delta$) the holes are light (anion valence band) and electrons are heavy (d bands). There are intermediate regions between these two limiting cases.

2.2.2   Surface

A surface represents a breaking of the periodicity in the direction perpendicular to it. Geometrical changes may be induced like relaxation, rumpling or reconstruction effects. Furthermore, as one can deduce from the discussion above, the breaking of anion-cation bonds perturbs the electronic structure in the surface layers through changes in the electrostatic potentials and the orbital hybridization [10]. Tasker [18] classified the surfaces into three types:

type 1 is neutral, type 2 is charged but without dipole moment perpendicular to the surface and type 3 is charged with a dipole moment perpendicular to the surface. The first two surface types should have modest surface energies and may be stable. They are called non-polar surfaces. The third surface type corresponds to the so-called polar surfaces. Their surface energy diverges and so this surface cannot exist without modification. We will divide our discussion into the case of the non-polar surfaces and the case of the polar ones.

Non-Polar Surfaces

The surface may be introduced simply by setting the hopping integral β equal to zero for all bonds crossing the surface plane. The electronic levels of the semi-infinite solid are then the same bonding and anti-bonding levels as in the bulk, together with an atomic level at the energy of the free atom. The latter state -a so-called surface state- has a degeneracy equal to the number of surface dangling bonds [11]. Nevertheless, surface states are rare for metal oxides with octahedral environment since each cation is hybridized with many anions and thus the breaking of one of these bond may not lead to surface states [10]. However more dramatic changes might occur at a surface than the arising of surface states. The bond breaking is quantitatively included in the Madelung constants at the surface, yielding the electrostatic potential at the surface. It will decrease as the coordination number decreases. As we have shown, the Madelung potential renormalizes the atomic energies and thus its change at the surface leads to changes of the atomic energies. The first consequence can be a gap narrowing since the valence band will raise and the conduction band lower [10]. Band narrowing can also be a consequence of this decrease of the coordination number [10]. Charge redistribution through change in the ionicity of the anion-cation band can take place at the surface and is a result of the competition between the reduction of the number of bonds and the decrease of the atomic energy difference [10]. All these effects can be modified by the structure distortions which take place at the surface. Generally, surface relaxation competes with the other surface phenomena so

that the band gap may be the same as in the bulk [10].

Polar Surfaces

Consider two layers bearing positive and negative charge densities equal to $\pm\sigma$ at $z = -a$ and $z = +a$ respectively. An electrostatic treatment of the dipole created by these two charged layers yields for the electric field $\overrightarrow{E}$ [19]:

$$\overrightarrow{E} = E\overrightarrow{z} = \begin{cases} \sigma/\epsilon_o\overrightarrow{z} & \text{for } -a\langle z\langle +a \\ 0 & \text{otherwise} \end{cases} \tag{2.13}$$

For N layers bearing alternatively $+\sigma$ and $-\sigma$, the solution for the electric field is the superposition of solutions of the above type. The field turns out to be σ/ϵ_o inside a double-layers and to zero between two double-layers. Its mean value in the slab is, therefore, non-zero: $\overline{E} = \sigma/(2\epsilon_o)$ and the electrostatic potential increases from one side of the slab to the other. Hence the total electrostatic energy is proportional to the slab thickness. This is the origin of the surface instability [10]. One can show that surface charge modifications such that the charge densities on the two outer planes are equal to $\sigma/2$ allow a cancellation of $\overline{E}$ [10]. Yet, since the mean value of V is non-zero, the energy remains proportional to the slab thickness. The addition of a dipole density $\sigma'R' = \frac{\sigma R}{4}$ yields oscillations of V around zero, so that the macroscopic electrostatic energy of the system vanishes [10]. The required charge density modification may be induced by charge defects, atomic redistribution or electron redistribution, due either to the bond-breaking process, to the change of ionicity of the anion-cation bond or to a metallization of the surfaces [10]. The electronic structure of the surface may be different than in the bulk due to these large charge redistributions.

2.3 Phonons

The normal modes of vibration of atoms or ions in a crystal can be described either classically, in terms of the relative motion of each atom with respect to the other atoms, or quantum mechanically, in terms of fundamental exci-

tations called phonons. Phonons are characterized by their wave-vectors $\overrightarrow{k}$, determining the wavelength and direction of propagation within the crystal. For a crystal structure having N atoms per unit cell, there are always three acoustic phonon branches and if $N > 1$, there are (3N-3) optical branches [6]. Phonons are called transverse when the atomic motion is perpendicular to the wave-vector and longitudinal when it is parallel. Dielectric materials become polarized when the electrons move from their equilibrium position relative to the atoms in response to an electric field ; this is the electronic polarization. In ionic compounds such as metal oxides, positive and negative ions will moreover move relative to each other in an electric field ; this is the ionic polarization [20]. For optical phonon modes positive and negative ions in each unit cell move out of phase with one another and therefore couple very strongly to externally applied electric fields [6]. The dielectric function shows how the dielectric constant varies with the frequency of the applied electric field and can be expressed as [6]:

$$\epsilon(\omega) = \epsilon_\infty + \sum_i \frac{Z_i}{\omega_i^2 - \omega^2 - i\omega\gamma_i} \tag{2.14}$$

ϵ_∞ is the high-frequency value of the dielectric function and corresponds to the value of the dielectric function for the limit case where the excitation frequency is so high that the ions cannot follow and so do not move. The sum is over the different distinct groups of optical phonon modes: Z_i is a parameter proportional to the dipole strength of the mode i, ω_i the frequency of the transverse optical mode and γ_i a damping factor associated with anharmonic effects. For an ionic crystal, the real part of the dielectric function can be approximated to [10, 20]:

$$Re(\epsilon(\omega)) = \epsilon_\infty \frac{\omega_{LO}^2 - \omega^2}{\omega_{TO}^2 - \omega^2} \tag{2.15}$$

where ω_{LO} and ω_{TO} are the frequencies of the long-wavelength bulk longitudinal and transversal optic modes, respectively. Fuchs and Kliewer [21] have predicted the existence of macroscopic surface optic modes in ionic crystals. They are associated with the roots of equation:

$$1 + Re(\epsilon(\omega_s)) = 0 \tag{2.16}$$

Taking equation 2.15 into account, one obtains:

$$\omega_s = \omega_{TO} \sqrt{\frac{\epsilon_0 + 1}{\epsilon_\infty + 1}} \tag{2.17}$$

where ϵ_0 is the static dielectric constant [20].

2.4 Adsorption

The bonding-process between metal-oxide surfaces and atoms and molecules from a liquid or gas phase is called adsorption. Different forces accompany this interaction and so one differentiates between physisorption and chemisorption. Physisorption is characterized by a weak van der Waals energy. When a solid surface and a molecule are brought close together, the electron clouds experience a slight displacement, leading to formation of a dipole. A dipole interaction between the surface and the molecule takes place, yielding the van der Waals energy. When instead a chemical bond is formed between the surface and the molecule, the adsorption process is called chemisorption. The molecule can then dissociate or react with the solid surface [22]. Figure 2.3 displays the energy curve for both adsorption processes as function of the distance between the surface and the adsorbed molecule for dissociative chemisorption. The dissociation process yields an activation energy for the chemisorption, as one can see in the figure 2.3. There are different types of gas-surface interaction that occur on metal-oxide surfaces. The first one occurs in the case of the physisorption aforementioned and is of weak electrostatic type. In the case of chemisorption, the relatively ionic nature of oxides leads to a predominance of acid-base, or donor-acceptor, interactions. Surface cations act as Lewis-acid sites and oxide ions as basic sites. Another important feature of molecule-oxide interactions is the involvement of lattice oxygens. Oxygen may be added to an adsorbate in the form of a neutral atom, accompanied by a corresponding reduction of the substrate. This is one type of oxidation/reduction reaction that can take place on metal-oxide surfaces. The other involves only electron transfer between the surface and the adsorbate [23]. Another important concept in the reactivity of oxide surfaces is coordinative unsaturation. Coordinatively unsaturated ions can act
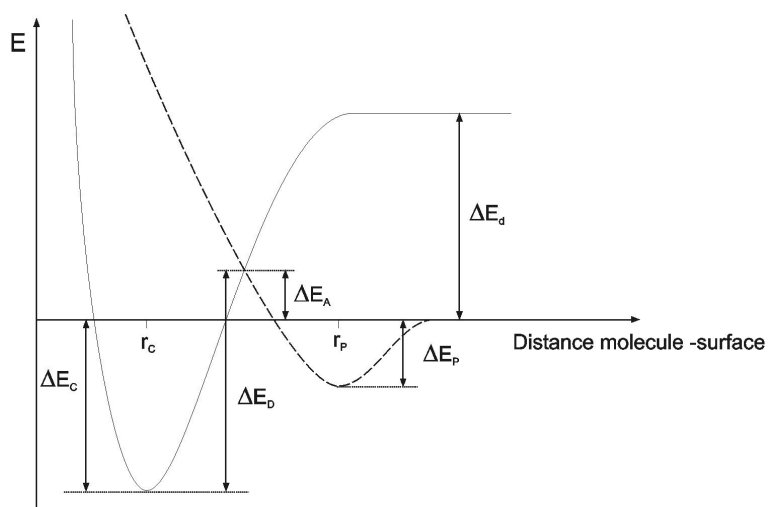
Figure 2.3: Schematic representation of physisorption (dashed line) and chemisorption (solid line) of the molecule after dissociation. ΔE_d is the dissociation energy, ΔE_A the activation energy, ΔE_D the desorption energy and ΔE_P and ΔE_C the physisorption and chemisorption energy, respectively.

as acidic or basic adsorption sites, but their bonding to the lattice is also weaker than that of coordinatively saturated ions and thus they can be more easily removed [23]. Step and defect sites necessarily exhibit a greater degree of coordinative unsaturation and may therefore lead to greater reactivity.

Chapter 3

Experimental Methods

3.1 Control of the Epitaxial Growth

3.1.1 Auger Electron Spectroscopy (AES)

The AES method uses electron transitions between core levels to characterize elements present in the sample. These electron transitions are induced by X-ray photons or electrons and are schematically shown in figure 3.1.

The first excited electrons leaves a hole behind which will be filled by another electron of an upper level, leading to the emission of a third electron, called Auger electron. Hence three levels are concerned: the level X of the first excited electron, the level Y of the electron that fills the hole left behind by the first excited electron and the level Y' of the Auger electron. The kinetic energy of the detected Auger electron then is:
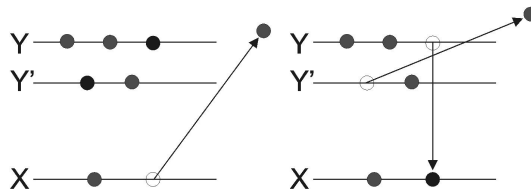
$$E_{kin} = W_X - W_Y - W'_{Y'} - e\phi \tag{3.1}$$

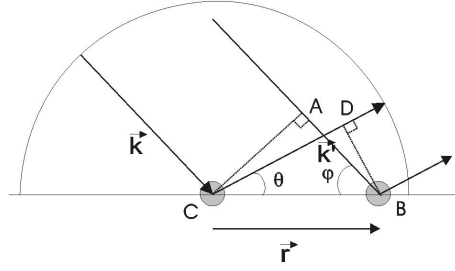Figure 3.1: Emission of an Auger electron as secondary excitation process

Figure 3.2: Bragg interpretation of diffraction: $\delta = AB - CD = r.(\cos\varphi - \cos\theta) = n\lambda$

where W denotes the ionization energy (positive) and W' the second ionization energy of the concerned level. One sees that the energy of the Auger electron does not depend on the primary energy but only on the three core levels X, Y and Y', which are element specific. Since the electron escape depth for a kinetic energy range of 10 to 2000 eV is only a few Å, AES like all other spectroscopic methods involving low energy electrons is a surface sensitive method [24]. The Auger peaks in the N(E) curves generally show very weak intensity, so that an electronic derivation method has been developed. The measured curve then is dN(E)/dE and the peaks exhibit a typical derivative shape.

3.1.2   Low Energy Electron Diffraction (LEED)

The LEED method is based on the phenomenon of propagation of slow electrons (energy in the range 0-400 eV) through ordered arrays of atoms. For this energy range, the electrons are absorbed already after few layers. Their reflection pattern is therefore only determined by the structure of the last layers [14]. The electron wave incident on the crystal shows strong reflection when the Bragg condition is satisfied. This can be obtained in a simple manner (see figure 3.2), considering that the path difference must be an integer of the wave length: $\delta = r(\cos\varphi - \cos\theta) = n\lambda$. Since $\vec{k}\cdot\vec{r} = k\cdot r\cdot\cos\varphi$ and $k = 2\pi/\lambda$ one obtains: $(\vec{k'} - \vec{k})\cdot\vec{r} = \vec{\Delta k}\cdot\vec{r} = n2\pi$. This corresponds to the definition of a vector of the Fourier transformed space, the reciprocal space, and so the diffraction condition is $\vec{\Delta k} = \vec{G}$. Note that this expresses the
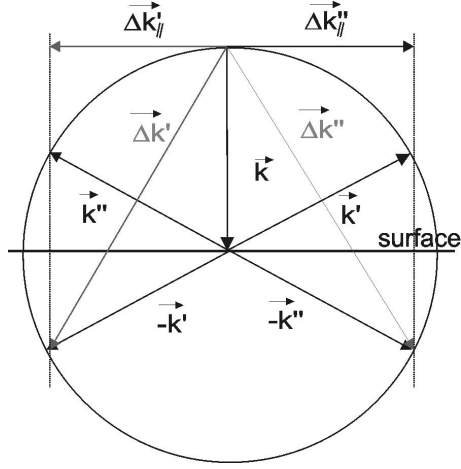
Figure 3.3: Diffraction by LEED

conservation of momentum. Since diffraction by low-energy electrons occurs only in the surface area, the dimension normal to the surface plays little role in the diffraction condition [14]. Consider now a two-dimensional lattice vector in real space: $\vec{r} = n_1\vec{a_1} + n_2\vec{a_2}$ where $\vec{a_1}$ and $\vec{a_2}$ are the primitive vectors of the surface unit cell. The definition of a vector in a reciprocal space then reads $\vec{r} \cdot \vec{G_\parallel} = n2\pi$ since $\vec{r} \cdot \vec{G_\perp} = 0$. $\vec{G_\parallel} = n_1'\vec{a_1^*} + n_2'\vec{a_2^*}$ with $\vec{a_1^*}$ and $\vec{a_2^*}$ primitive vectors of the surface unit cell in reciprocal space. Writing down the definition $\vec{r} \cdot \vec{G_\parallel} = n2\pi$ and taking into account that $\vec{a_i} \cdot \vec{a_j^*} = 2\pi\delta_{ij}$, one finds the relationship between the primitive vectors of the surface unit cell in real space and in reciprocal space:

$$[a^*] = 2\pi[[a]^T]^{-1} \tag{3.2}$$

where $[a^*]$ and $[a]$ correspond to the matrix notation of the primitive vectors $\vec{a^*}$ and $\vec{a}$, respectively. As LEED operates in two-dimensional space, only the component of the vector $\vec{\Delta k}$ parallel to the surface is important. This and the fact that the electron beam is incident perpendicular onto the surface are the reasons why the LEED spots correspond to the reciprocal lattice of the surface, as figure 3.3 shows. LEED can then be used in a simple qualitative way to determine the crystallographic structure of the surface.

3.2 Photoemission

3.2.1 Theory of Photoemission

Here, we shall present a one-electron picture of the photoemission (PE) process which allows one to interpret photoemission spectra in a relatively simple fashion. In the next sections, we will see how many-electron effects can be taken into account. In the Three-Step Model, the complicated photoemission process is divided into three steps: the excitation of a photoelectron, its passage through the solid to the surface and its penetration through the surface into the vacuum, where it is detected.

Excitation of a photoelectron

To describe the optical excitation of an electron from an initial state into a final state within the crystal, one shall first consider an electron in the crystal interacting with the incident radiation. The Hamiltonian of this system reads:

$$H = \frac{1}{2m}[\overrightarrow{P} - q\overrightarrow{A}]^2 + V(R) - \frac{q}{m}\overrightarrow{S}.\overrightarrow{B} \qquad (3.3)$$

where $\overrightarrow{P}$ is the momentum of the electron, $\overrightarrow{A}$ the vector potential of the exciting electromagnetic field, V the potential created by the lattice nuclei, $\overrightarrow{S}$ the spin of the electron and $\overrightarrow{B}$ the magnetic induction field of the light. One can write:

$$H = H_o + H'(t) \qquad (3.4)$$

with

$$H_o = \frac{\overrightarrow{P}^2}{2m} - V(R) \qquad (3.5)$$

and

$$H'(t) = -\frac{q}{m}\overrightarrow{P}.\overrightarrow{A} - \frac{q}{m}\overrightarrow{S}.\overrightarrow{B} = H'_I - H'_{II} \qquad (3.6)$$

where the A^2 term in $H'(t)$ has been neglected. One can show [7] that for the used light sources, one has:

$$\frac{H'_{II}}{H'_I} \ll 1 \qquad (3.7)$$

Therefore one can neglect the term H'_{II} and treat the term $H' = H'_I$ as a perturbation of H_o. Consider for the radiation a monochromatic plane wave propagating along the y-axis with $\overrightarrow{E}$ parallel to the z-axis and $\overrightarrow{B}$ to the x-axis. One can choose a vector potential such as the scalar potential is equal to zero, so that $\overrightarrow{A}$ can be written as:

$$\overrightarrow{A}(\overrightarrow{r}, t) = A_o \overrightarrow{e_z} e^{i(ky-\omega t)} + A_o^* \overrightarrow{e_z} e^{-i(ky-\omega t)} \tag{3.8}$$

Thus one can find the following expression for $H'(t)$ [7]:

$$H'(t) = \frac{q\xi}{m\omega} P_z \sin \omega t \tag{3.9}$$

where ξ is the amplitude of the electrical field $\overrightarrow{E}$ of the light. This expression for H' for the perturbation induced by a radiation is called the electric dipole approximation. The probability of the radiative transition between an initial state $|\varphi_i\rangle$ and a final state $|\varphi_f\rangle$ is described by the matrix element $\langle\varphi_f|H'(t)|\varphi_i\rangle$. The commutation relations $[Z, H_o] = [Z, \frac{P_z^2}{2m}] = i\hbar\frac{P_z}{m}$ yield

$$\langle\varphi_f|H'(t)|\varphi_i\rangle = iq\frac{\omega_{fi}}{\omega}\xi \sin \omega t \langle\varphi_i|Z|\varphi_f\rangle \tag{3.10}$$

where $\omega_{fi} = \frac{E_f - E_i}{\hbar}$. Note that the operator Z in equation 3.10 corresponds to the orientation of the vector potential $\overrightarrow{A}$ parallel to the z-axis and so to the orientation of the electrical field $\overrightarrow{E}$ since $\overrightarrow{E} = -\frac{\partial\overrightarrow{A}}{\partial t}$. Within a perturbation treatment for the Hamiltonian $H = H_o + H'$ one finds a coupling between two states $|\varphi_i\rangle$ and $|\varphi_f\rangle$ when $\omega \simeq \pm\omega_{fi}$ corresponding to absorption and emission of a photon, respectively [7]. The transition probability between initial and final state then reads:

$$w_{fi} = \frac{2\pi}{\hbar}|\langle\varphi_f|H'|\varphi_i\rangle|^2\delta(E_f - E_i - \hbar\omega) \tag{3.11}$$

Equation 3.11 is called Fermi's Golden Rule. We have established the transition matrix in the electric dipole approximation but not discussed its value. Group theory uses symmetry considerations to decide when integrals are necessarily zero. It says that an integral will be necessarily zero unless the integrand is a basis for the totally symmetric irreducible representation (irrep) of the group [9, 25] or equivalently if the irrep $\Gamma^{H'\varphi_f}$ contains the irrep

Γ^{φ_i}. When the system contains a mirror plane, it is possible to classify the wavefunctions and H' as even or odd with respect to the mirror plane. One can therefore predict when emission should occur or not. When spin-orbit coupling is important, odd and even states are mixed and the polarization rule is no longer strictly valid [26]. Nevertheless, we will see in section 3.2.4 that it is helpful in the case of adsorbates. In the case of emission from solids, one shall consider crystal states defined by the quantum number $\overrightarrow{k}$. We shall consider in a first approximation direct transitions where only electrons and photons participate in the interaction, whereas in indirect transitions other elementary excitations participate, e.g. phonons [25, 26]. Not only energy but momentum conservation has to be fulfilled: $k_f = k_i + k_{ph}$. Since $k_{ph} \simeq 0$ within the energy range considered, one has $k_f \simeq k_i$ [27]. One can regard the quantum number as a label for the irrep and show that $\overrightarrow{k}$ and $\overrightarrow{k} + \overrightarrow{G}$ ($\overrightarrow{G}$ being a lattice vector of a reciprocal space) label the same irrep, that is to say that they are indistinguishable from the group-theoretical point of view [28]. This corresponds to the Bloch theorem discussed in section 2.2 of chapter 2. The crystal lattice can therefore furnish momentum in quantities of $\overrightarrow{G}$ and so allows direct transitions in the reduced zone scheme [24, 29]. This demonstrates that photoemission is accompanied by diffraction against the crystal lattice [27, 29]. One has therefore:

$$\overrightarrow{K_f} = \overrightarrow{k_i} + \overrightarrow{G} \tag{3.12}$$

$\overrightarrow{K_f}$ denotes the wave vector in the extended zone scheme.

Transport to the Surface

A large number of electrons undergoes inelastic scattering processes, repeatedly losing energy by electron-plasmon or electron-phonon scattering. They may finally emerge as low-energy electrons, constituting the true secondary background for valence photoelectron spectra [26, 30] or the inelastic tail in core level photoelectron spectra [24].
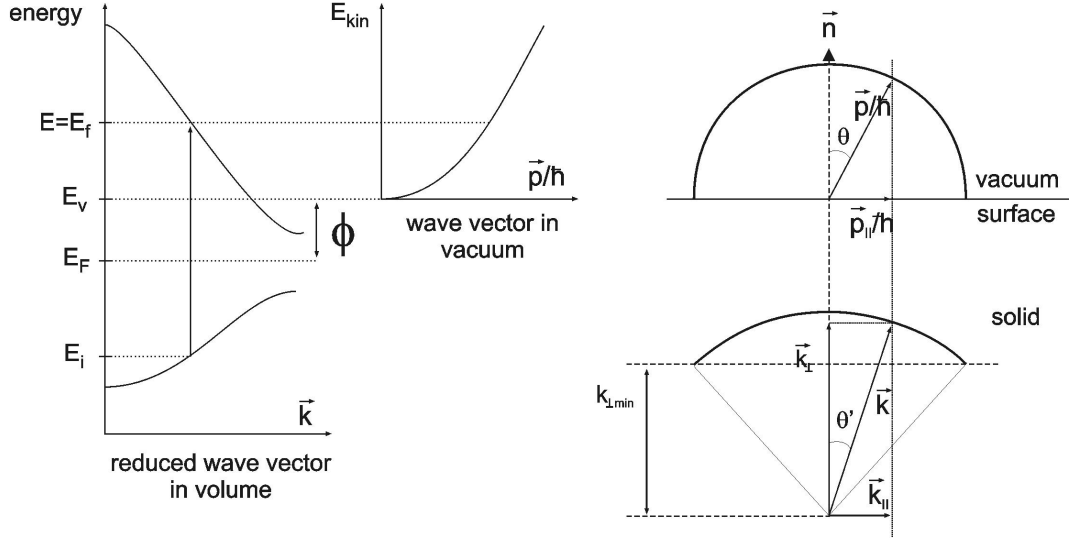
Figure 3.4: Free-electron final-state model for photoemission and escape condition [24].

Escape into Vacuum

The transmission of the photoexcited electrons into vacuum can be described as the scattering of a Bloch electron wave from the surface-atom potential with translational symmetry parallel but not perpendicular to the surface [26]. This yields:

$$\overrightarrow{p}_\parallel/\hbar = \overrightarrow{K}_{f\parallel} + \overrightarrow{G}_S = \overrightarrow{k}_{i\parallel} + \overrightarrow{G}_\parallel + \overrightarrow{G}_S \qquad (3.13)$$

Here $\overrightarrow{p}$ is the momentum of the photoelectron in vacuum, $\overrightarrow{K}$ is its wave vector inside the solid, $\overrightarrow{k}$ is the wave vector in the reduced zone scheme, $\overrightarrow{G}$ is the reciprocal lattice vector of equation 3.12 and $\overrightarrow{G}_S$ is a reciprocal lattice vector of the surface. The subscript $\parallel$ denotes the component parallel to the surface. The escaping electrons are those for which the component of the kinetic energy normal to the surface is sufficient to overcome the surface potential barrier ϕ (the work function); the other electrons are totally reflected back into the bulk. This yields the escape-cone argument, as shown in fig 3.4. One sees that the threshold $K_{\perp min}$ has been reached when $\overrightarrow{K}_\parallel = \overrightarrow{p}/\hbar$

and so:

$$K_{\perp min} = [\frac{2m}{\hbar^2}E_v]^{1/2} \tag{3.14}$$

The relation between the angles θ and θ' is given writing $k_{f\parallel} = |\vec{k}|\sin\theta' = \frac{|\vec{p}|}{\hbar}\sin\theta$. It yields:

$$\sin\theta(\frac{2m}{\hbar^2}E_{kin})^{1/2} = \sin\theta'(\frac{2m}{\hbar^2}E_f)^{1/2} \tag{3.15}$$

From these equations it is clear that an experiment taken at any $\vec{k_\parallel}$ does not allow the determination of the full wave vector $\vec{k}$ of the crystal state because $\vec{k_\perp}$ remains undetermined. To obtain $\vec{k_\perp}$ for example for the determination of the band structure, one has to apply more elaborate methods that we shall not develop here. One can summarize the above statements with the following expression for the angle-resolved photoelectron energy spectrum:

$$N(E, \vec{K_\parallel}, \hbar\omega) = \sum_{i,f} |H'_{fi}|^2.\delta(E_f(\vec{k_f}) - E_i(\vec{k_i}) - \hbar\omega).\delta(E - [E_f(\vec{k_f}) - \phi])$$
$$\times \delta(\vec{k_i} + \vec{G} - \vec{K}).\delta(\vec{K_\parallel} - \vec{p_\parallel}(\theta,\varphi)/\hbar) \tag{3.16}$$

The direction (θ, φ) of the electron emission has been indicated for the case of an angle-resolved experiment.

3.2.2 Valence Band Spectra

Density of States and Band Structure

To probe the valence band states with photoemission, the photon energy range used corresponds to the ultra violet region and so one speaks of ultra violet photoelectron spectroscopy (UPS). When the light beam, the sample and the spectrometer can be moved relative to each other, one can perform angle-resolved measurement and one speaks of angle-resolved UPS (ARUPS). Here, we shall discuss some points on the interpretation of the ARUP spectra.

The measured kinetic energy of the photoelectrons is related to their binding energy through $E_{kin} = \hbar\omega - E_B - e\phi$. The binding energy is synonymous with the ionization potential $E_B = I_P = E(N-1) - E(N)$, E(N) and E(N-1)
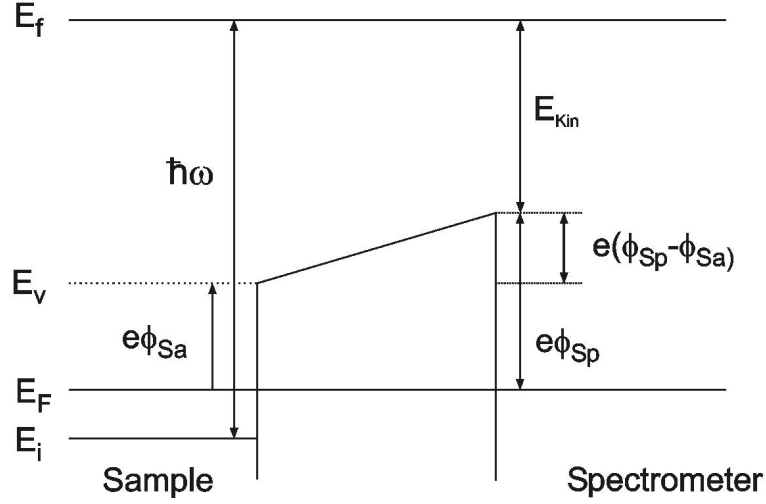
Figure 3.5: Energy level diagram for photoelectron spectroscopy

denote the energies of the system with N and N-1 electrons, respectively [27]. The population of the valence bands can therefore be studied with photoemission. But as already outlined before, the photoemission process is not that simple. Let us begin with localized electrons. Polarization dependence measurements may be qualitatively explained within the model of localized electrons described by atomic-like orbitals and assuming that the final state is a plane wave $\varphi_f = e^{i\vec{k_f}.\vec{r}}$. Fermi's Golden Rule then reads [29, 31]:

$$w_{fi} \propto |\vec{A}.\vec{k}|^2 |F_{nl}(\rho)|^2 Y_{lm}^2(\theta, \varphi) \delta(E_f - E_i - \hbar\omega) \qquad (3.17)$$

where $F_{nl}(\rho)$ is the Fourier transform of the radial part of the wave function of the initial state and Y_{lm} contains its angular dependence. For delocalized states, however, the above relation is not valid anymore and the peaks in the spectra will move in energy as a function of $\vec{k}_\parallel$: they show dispersion. Since the final states appear in Fermi's Golden Rule, one has to take into account what final states can contribute to the photoemission process to interpret the UPS data with the dipole selection rules [24, 32]. The nature of the final states will play an important role in the shape of the photoelectron spectrum N(E). But with increasing final-state energy a continuum of final states becomes available and thus photoionization for all initial states becomes possible and the spectrum displays the density of (occupied) states

(DOS) [30]. To probe the band structure of the sample through the observed dispersion, one has to vary the wave vector $\overrightarrow{k}$. One therefore has two possibilities: to vary the photon energy or to vary the detection angle (see [24] for more details).

Work Function

The low energy cutoff gives us information about the work function of the material. The kinetic energy of the photoelectrons in the vacuum is

$$E_{kin-vac} = \hbar\omega - E_B - e\phi_{Sa} \qquad (3.18)$$

where E_B is the binding energy as shows figure 3.5. But since the spectrometer has a different work function than ϕ_{Sp} as the sample (ϕ_{Sa}), the measured kinetic energy is:

$$E_{kin-meas} = \hbar\omega - E_B - e\phi_{Sp} \qquad (3.19)$$

ϕ_{Sp} can be determined by taking a spectrum of a metal which exhibits a sharp Fermi level. Considering now the photoelectrons for which $E_B = \hbar\omega - e\phi_{Sa}$, i.e. the electrons that have just enough energy to overcome the surface potential barrier, and replacing it in 3.19, one obtains

$$E_{kin-meas} = e(\phi_{Sa} - \phi_{Sp}) \qquad (3.20)$$

for the lowest energetic electrons. Since this energy is negative when $\phi_{Sp} > \phi_{Sa}$, one will detect these electrons only when $\phi_{Sa} > \phi_{Sp}$.

3.2.3 Core Levels

XPS

To photoionize electrons originating from core levels, photon energies in the X-ray range are required and thus one speaks of X-ray photoelectron spectroscopy (XPS). This spectroscopy allows one to identify the elements present in the sample by determining the binding energies of the various photoelectron core peaks in the spectrum using equation 3.19. Moreover, one can determine the chemical state (i.e. oxidation state, lattice sites, molecular

environment etc) of the element considered measuring the so-called chemical shift of its core level binding energy. The physical basis for chemical shifts is easily illustrated by the charge potential model which describes the binding energy E_i of a particular core level on atom i in terms of an energy reference E_i^o, its charge q_i and point charges on the surrounding atoms j [27]:

$$E_i = E_i^o + kq_i + \sum_j q_j/r_{ij} \tag{3.21}$$

r_{ij} is the separation between atoms i and j and k is a proportionality constant. Here the atom i is considered to be a hollow sphere on the surface of which the charge q_i of the valence electrons is distributed. One sees that the binding energies of all core levels should be affected to the same extent by a change in q_i.

Although core level photoelectron peaks from solids show characteristic binding energies of the element involved and also chemical shifts as just discussed, they do not show simple lifetime-broadened Lorentz profiles [30]. Since the electrons interact with each other via the Coulomb and exchange interaction, the emission of an electron after the photoexcitation process leads to excitations in the remaining system [24]. These excitations yield extra structure in the photoemission spectrum besides the main line, the satellites. One can define the spectral function $A(E_f)$ by the delta function in equation 3.11 and thus obtain for the photoelectron current:

$$I \propto \sum_{i,f} |\langle \varphi_f | H' | \varphi_i \rangle|^2 A(E) \tag{3.22}$$

The result is actually valid far beyond the one-electron approximation used in section 3.2.1 because the spectral function can be related to the Green's function and then describe the interaction between the core hole and the surrounding electron cloud [33]. The spectral function for an interacting hole is then given by:

$$A(E) = \frac{1}{\pi} Im G_i(E) \tag{3.23}$$

where $G_i(E_f)$ is the Green's function for an interacting core hole:

$$G_i(E) = \frac{1}{E_f - E_i^o - i \sum_i(E)} \tag{3.24}$$

The self-energy $\sum_i(E)$ includes everything that can happen to a core hole and represents a generalized energy correction to the energy in the noninteracting system [33]. This theoretical model describes an interacting electron system where a core hole is created at a specific instant of time and destroyed at a later time. The Green's function can be separated into two parts. The first one is similar to the result for the noninteracting system and describes a slightly modified electron, called a quasiparticle. This leads to the coherent part of the spectrum (main line). The second one gives rise to the incoherent part of the spectrum (satellites) [24].

There are many interaction effects of the core hole with the system that may give rise to satellite structures in the photoemission spectrum. These are the "final state effects"

Exciting an electron from a closed-shell with an orbital momentum $\neq 0$ (say a p electron) leads to multiple final states depending whether the spin of the electron that left is parallel or antiparallel to its orbital momentum ($p_{3/2}$ and $p_{1/2}$) [27]. This effect is called multiplet splitting.

In a correlated system where electrons try to avoid each other, the electron density in the neighbourhood of any given electron will be disturbed. This leads to virtually excited states above the Fermi level. The photoemission process may then leave the residual ion in an excited state and lead to satellites due to ground-state correlations (Fermi sea correlations effects) [33].

When an electron leaves the core region, the surrounding electron cloud will contract in response to the change in the potential in order to screen out the positive charge of the core hole and this results in a relaxation shift of the core level energy [33]. This reorganization of the electronic structure may also lead to the formation of excited states. If an electron is excited to higher-lying bound states, the corresponding satellite lines in the spectrum are called "shake-up" satellites [27]. There is also the possibility of the primary electron becoming "captured", giving off its excess energy to the shake-off electron, leading to a different satellite spectrum than the ordinary shake-up process [33]. In metals, the photoelectron peaks may become asymmetric due to such multi-electrons events.

In transition-metal compounds the core hole screening process can be explained by charge transfer from filled ligand orbitals to empty metal orbitals. For these compounds, there is a considerable overlap between ligand and metal orbitals and one should rather argue in terms of polarization of molecular orbitals than of ligand-to-3d charge screening [33]. Nevertheless, we shall discuss here this screening phenomenon using a simple molecular orbital model as already presented in section 2.2 of chapter 2. Within the configuration interaction theory the ground-state can be described in a simple case by a mixture of the d^n and $L^{-1}d^{n+1}$ configurations, where L^{-1} denotes a hole in the ligand orbitals. There are therefore two possible photoexcited final states: $c^{-1}d^n$ and $c^{-1}L^{-1}d^{n+1}$. c^{-1} denotes the core hole left behind. This constitutes an additional Coulomb interaction for electrons at higher levels and therefore lowers their energy. The $c^{-1}L^{-1}d^{n+1}$ configuration will then be more lowered than the $c^{-1}d^n$ configuration. This lowering is described by the Coulomb interaction between the core hole and the d electron U_{cd}. Then if $\Delta < U_{cd}$ the $c^{-1}L^{-1}d^{n+1}$ configuration has the lowest energy and corresponds to the main line. The satellite line corresponds to the $c^{-1}d^n$ configuration. The lines are separated by the energy $\Delta - U_{cd}$ when one neglects the coupling between both configurations [24].

NEXAFS

In near edge X-ray absorption fine structure spectroscopy (NEXAFS) one studies the absorption of X-rays in an energy range around the absorption threshold of the considered level of the element under study. As already discussed above, the absorption of a photon leads to emission of a photoelectron if its kinetic energy is sufficient to overcome the potential barrier. A secondary process may occur with the filling of the core hole left behind by another electron which leads to emission of a fluorescent photon and eventually emission of an Auger electron as discussed in section 3.1.1. In this work, we performed NEXAFS using the Auger detection yield and this is why we shall here only discuss this recording method. The other detection methods are partial and total electron yield detection and fluorescence yield

detection. The Auger yield detection consists of recording the intensity of the Auger peak signal as function of the photon energy. Since the emission of an Auger electron depends firstly on the creation of a hole on the considered shell, the intensity of the Auger signal will follow the X-ray absorption cross section of this shell, which is clearly dependent of the photon energy [34] and will reflect the density of empty states, if one neglects reaction with the core hole [12]. The Auger signal is therefore used only as a fingerprint of the X-ray absorption of a particular shell of an element one wants to study. In NEXAFS, the photoelectron is not a free electron as in XPS but is just above the Fermi level. The dipole transition thus poses strong selection rules to the final state that read [12]:

$$\Delta l_i = \pm 1$$
$$\Delta s_i = 0$$

(3.25)

For 3d transition metal compound, the metal 2p or L edge X-ray absorption corresponds to the transition from the 2p level to an unoccupied 3d level. This can be formally expressed by $2p^6 3d^n \rightarrow 2p^5 3d^{n+1}$ in a purely ionic picture. Figure 3.6 shows the spectrum obtained for such a transition. The top curve corresponds to a case without electronic interaction where the peak energy is determined by the energy difference between the initial and final states. Because of the creation of the hole on the 2p level, 2p spin-orbit may split the initial state into $2p_{3/2}$ and $2p_{1/2}$ and this effect is shown in the middle curve. This results in two L-edge features labeled L_{III} and L_{II} respectively. Finally, for the bottom curve octahedral ligand-field splitting has been taken into account, which splits both L_{III} and L_{II} features into doublet features corresponding to the splitting of the d-states into t_{2g} and e_g [35]. The actual shape of the L-edge spectra may differ from the one of the bottom curve obtained within the single-particle scheme. Because of the 2p core hole in the final state, many-electrons effects, as for XPS, have to be theoretically treated to interpret L-edge spectra. This is the purpose of the atomic multiplet calculations. They consist of three steps. First, the energy levels in the initial-state $3d^n$ multiplet and the final-state $2p^5 3d^{n+1}$ multiplet are calculated in O(3) symmetry. Then the atomic multiplet spectrum
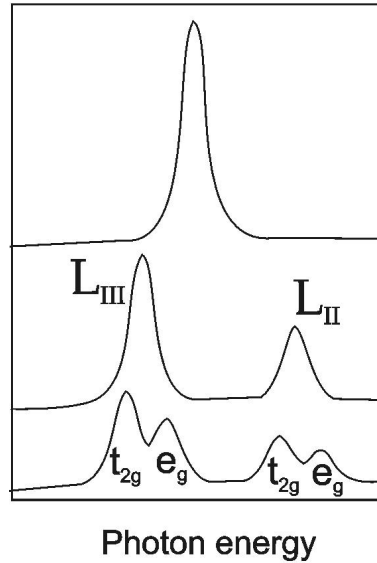
Figure 3.6: NEXAF spectrum for a metal L-edge transition $2p^6 3d^n \rightarrow 2p^5 3d^{n+1}$

is calculated by means of the dipole transition from the ground state to all final states. The third part is the projection of the O(3) multiplets to cubic (O_h) symmetry [36]. The Hamiltonian of the ground and final multiplet-states of the first step contains terms describing the many-electrons effects such as the 3d-3d Coulomb interaction and the 2p-3d Coulomb and exchange interaction. The spin-orbit coupling of the 2p core hole and the crystal-field are also included. For more details concerning this calculation method the reader is referred to [12].

The oxygen 1s or K-edge spectrum corresponds to the transition from the 1s level to unoccupied 2p levels according to the dipole selection rules 3.25. Therefore, to a first-order approximation, the K-edge spectrum can be envisioned as an image of the p-projected unoccupied density of states [35]. For a transition metal oxide, the absorption intensity for a 1s → 2p transition should be very weak in a purely ionic picture since the 2p level of the oxygen is full. Thus the signal intensity provides a good indication of covalency effects which give the unoccupied 3d orbitals a 2p character [37]. Figure 3.7 shows how to interpret the features observed in K-edge spectra
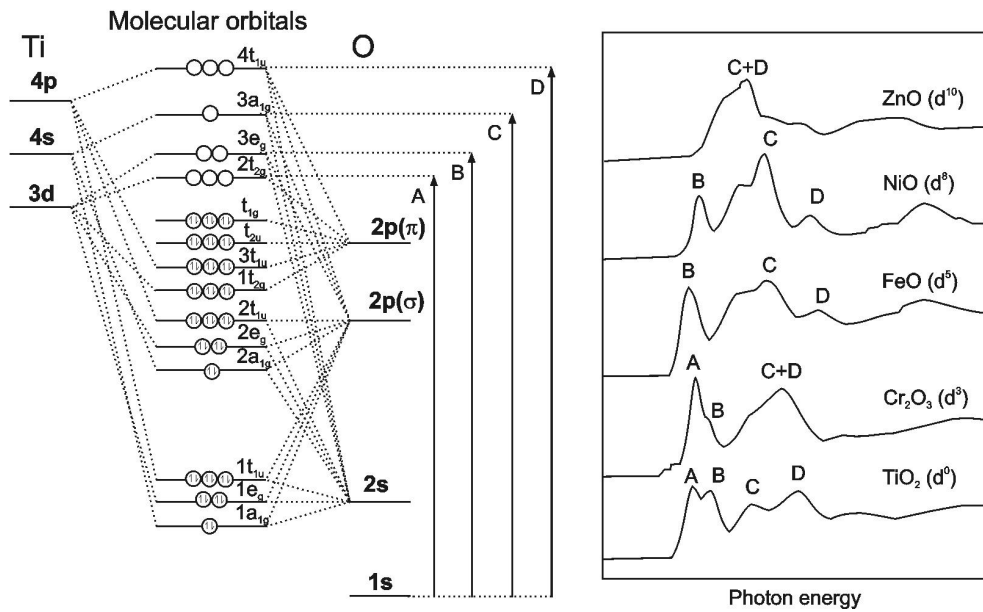
Figure 3.7: Schematics of molecular orbitals of a TiO_6^{-8} cluster modelling TiO_2 in an octahedral symmetry (left) and oxygen K-edge NEXAF spectra of several 3d transition metal oxides from [35] (right)

within the simple molecular orbitals model. The four O K-edge features A,B,C, and D can be assigned to the one electron transition from the O 1s orbital to the $2t_{2g}$, $3e_g$, $3a_{1g}$ and $4t_{1u}$ orbitals of TiO_2, respectively. Similarly, the one-electron excitation scheme can be used to explain the features of the spectra for the other oxides in figure 3.7 taking into account that the first two molecular orbitals are partially occupied.

3.2.4   Study of Adsorbates - Angular distribution

We shall now discuss the case of a system constituted of a substrate and molecules adsorbed on its surface.

UPS

Since UPS is a surface sensitive technique it is especially suited for the investigation of molecules adsorbed on solid surfaces. The molecules may adsorb in a preferred orientation depending on the substrate surface orientation.

The photoelectron spectrum will consequently show an angular distribution specific to the orientation of the molecules. This constitutes a great difference compared to spectra obtained from gas molecules where averaging over all possible molecular orientations takes place.

In section 3.2.1, we have shown that photoemission is governed by Fermi's Golden Rule given in equation 3.11. Consider the matrix element $\langle \Psi_f | H' | \Psi_i \rangle$. Ψ_f and Ψ_i here are the many-electrons wave function of the final state and initial state of the photoemission process, respectively. Thus Ψ_f consists of the ion state $^{N-1}\Psi_{e,E}$ and the emitted electron $\varphi_e(n)$. Since H' is a one electron operator, the matrix element can be rewritten as [38]:

$$I \propto | \sum_{k,e} \langle \varphi_e(n) | H' | \varphi_k(n) \rangle \langle ^{N-1}\Psi_{e,E} | a_k \Psi_i \rangle |^2 \qquad (3.26)$$

where a_k and $\varphi_k(n)$ are the annihilation operator and the one-electron initial wavefunction of the emitted electron (before excitation), respectively. The first matrix element determines the angular distribution pattern, the second matrix element defines the absolute value and contains the internal degrees of freedom of the system, e.g. the line widths [38]. We have already discussed in section 3.2.1 the group theory statement on the value of the matrix element considered above: an integral will necessarily be zero unless the integrand is a basis for the totally symmetric irreducible representation (irrep) of the group [9, 25]. In the case of adsorbates, these symmetry considerations are very helpful provided the adsorbed molecules do not dissociate and do not interact strongly with the substrate. Then the photoelectron spectrum is determined solely by the adsorbate molecule itself, independent of the substrate [30]. As already discussed in section 3.2.1, H' is proportional to Z and so has the symmetry of Z (belongs to the same irrep) [28]. We assume that the surface has a mirror plane and that both the direction of incidence of the exciting light and the detection direction for emitted electrons are within the mirror plane. The final state must always be even with respect to reflection in the mirror plane otherwise a detector located in the mirror plane would see a node of the emitted electron. The initial states can be both even or odd with respect to the mirror plane and the electrical field $\overrightarrow{E}$ can be in the mirror plane or perpendicular to it, leading to even and odd elements in

H', respectively [26]. A photoemission signal will therefore be detected only when the initial state and the electric field are both even or both odd with respect to reflection in the mirror plane.

Intermolecular interactions are always present in real adsorbate systems and determine, among other things, the ordering of the adsorbed overlayers, leading to a two dimensionally periodic arrangement of adsorbed molecules [38]. We can assign a certain space group to this arrangement and then classify the electronic band states of the system according to the space group [38].

It may be useful to compare UPS difference spectra obtained on chemisorption of a particular molecule with the gas phase spectrum of the same molecule. This procedure can help to identify the nature of the adsorbate in the case of dissociation and/or reaction and allows one to get more information on the way the molecule adsorbs. As already mentioned in section 3.2.2, one measures with photoelectron spectroscopy not directly the orbital energies but the ionization energies. The ionization energy is defined by the energy difference between the initial neutral state and the final state where an electron from the ith level has been emitted and thus $I_P = E(N-1) - E(N)$. One will then find the gas phase energy levels in general shifted on an absolute energy scale relative to those of the chemisorbed molecule. This shift originates in both the initial and the final state [39] and is given by [27]:

$$\Delta E = E_{ad} - E_{gas} = E_{relax} + E_{bond\ shift} - (\varphi + \Delta\varphi) \qquad (3.27)$$

The term E_{relax} corresponds to the so-called extra-molecular relaxation-polarization (EMRP) shift. This is a final state effect and accounts for the fact that the hole in the adsorbed particle left after photoionization interacts with its image in the solid, resulting in some energy gain. The term $E_{bond\ shift}$ is connected with the initial state of the system and concerns the orbitals of the adsorbate involved in the bonding to the surface. This quantity will permit one to know which orbitals interact with the substrate.
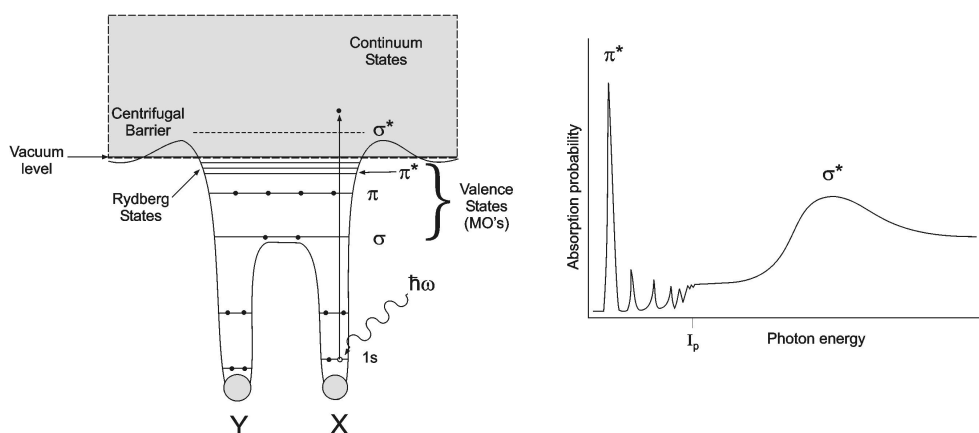
Figure 3.8: Schematic potentials (left) and K-edge spectra (right) of diatomic molecules

XPS

In contrast to UPS, the study of angular effects in XPS has found much less attention. It is in principle possible to extract information about the adsorption site geometries from XPS angular resolved data, even for systems without long-range order, but this technique is very elaborate [27].

NEXAFS

By contrast, the study of adsorbate orientation with NEXAFS is very easy and powerful. Figure 3.8 shows the NEXAF spectrum obtained for a diatomic molecule. π resonances arise from electronic transitions from a 1s initial state to Rydberg or unfilled molecular orbital final states. For photon energies larger than the ionization potential, transitions to levels of the continuum states occur, yielding no sharp features like for the π resonance but a broader feature as shown in figure 3.8. The dipole selection rules governing K-shell NEXAFS resonance intensities are quite simple: the resonance intensity associated with a specific molecular orbital final state is largest if the $\overrightarrow{E}$ vector points in the direction of that molecular orbital, and the intensity vanishes if $\overrightarrow{E}$ is perpendicular to the direction of the orbital [34].
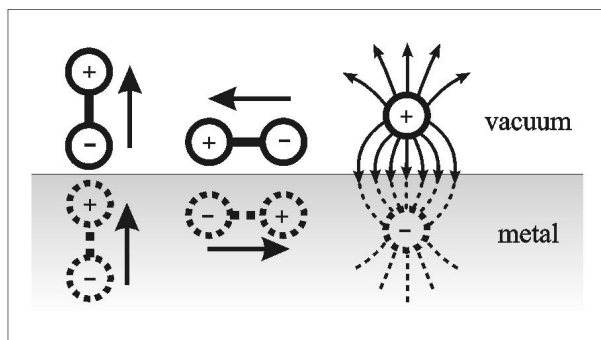
Figure 3.9: Schematic illustration of dipole screening on metal surfaces

3.3   Vibrational Spectroscopy

3.3.1   IRAS

Analogous to the interaction between electromagnetic radiation and an electron discussed in section 3.2.1, Fermi's Golden Rules describe the interaction between a radiation and a molecule in the gas phase in terms of the excitation probability of a vibration [9]:

$$I \propto |\langle\varphi_f|\overrightarrow{\mu}.\overrightarrow{E}|\varphi_i\rangle|^2 \tag{3.28}$$

where $|\varphi_i\rangle$ and $|\varphi_f\rangle$ are the initial and excited state, respectively, $\overrightarrow{E}$ the electrical field and $\overrightarrow{\mu}$ the dipole moment of the molecule. Only vibrations where the dipole moment changes in magnitude and/or direction are infrared active [40]. One can define the dynamic dipole moment as $(\partial\overrightarrow{\mu}/\partial Q_k)_o$ and show that in the case of surface species on metal surfaces, only vibrational modes with a non-zero component of the dynamic dipole moment perpendicular to the surface can be observed [41]. This originates from the screening effect of the electrons of the metal which produces an image dipole within the metal. The resulting dipole will vanish if the molecular dipole is parallel to the surface, as is schematically shown in figure 3.9.

3.3.2 HREELS

In an electron energy loss experiment, a monoenergetic beam of electrons is incident onto the sample surface and the energy spectrum of the scattered electrons is recorded. One can distinguish three limiting cases for the interaction between the incoming electron and the vibrating atoms in the solid.

Dipole scattering occurs when a vibrational normal mode of an adsorbed molecule is excited. The static electric dipole moment μ is now modulated to become $\mu + p \exp(-i\omega_o t)$ where ω_o is the vibration frequency. The oscillating component of the electric dipole moment sets up electric fields in the vacuum above the crystal and these oscillating electric fields scatter the incoming electron inelastically [42]. As the electron is reflected from the crystal surface before it strikes the detector, the scattering cross section is peaked strongly around the forward direction, i.e the specular direction. The dipole produces an image dipole in the substrate parallel to itself. Therefore, the total oscillating dipole moment of the molecule-substrate combination has a strength 2p for dipole moments perpendicular to the surface and vanishes for dipole moments parallel to the surface. The consequence is that for a molecule which stands vertically on the surface only the modes involving motions normal to the surface are detectable. Additional modes in the spectrum indicate that the molecule axis is tilted away from the surface normal [42].

Impact scattering is based on the short-range portion of the electron-molecule interaction. The incoming electron with wave vector k^I and energy E_I is scattered by the potential of the molecule to a final state of energy $E_S = E_I \pm \hbar\omega_o$ and wave vector k^S with $Q_\parallel = k_\parallel^S - k_\parallel^I$. The subscript $\parallel$ denotes the component parallel to the surface, Q is the transmitted wave vector. For the simple case of an atom adsorbed in a site of sufficiently high symmetry, the cross sections for the vibrations parallel to the surface vanishes [42]. The angular distribution of the electrons scattered inelastically from a molecular vibration is relatively broad. Because of the very small accepted solid angle of the spectrometer typical count rates of inelastically scattered electrons from impact scattering are small.

The last scattering process is the inelastic scattering via an intermediate negative ion resonance. It involves the temporary negative ion formation due to electron capture. This results in a change of the potential energy surface (PES). The nuclei find themselves in a non-equilibrium position with respect to that new PES and thus respond by moving. After a short ion lifetime, the original PES is restored but now with the vibrational coordinates displaced from the ground state equilibrium point [41].

Chapter 4

Experimental Setup

Three different ultra-high vacuum (UHV) systems were used for this work. Angle resolved UV photoelectron spectra (ARUPS) were taken in the first one. X-ray photoemission spectroscopy (XPS) and near edge X-ray absorption spectroscopy (NEXAFS) measurements were performed in the second system at the BESSY II synchrotron radiation source in Berlin. And in the third system, high resolution electron energy loss spectra (HREELS) and ínfrared absorption spectra (IRAS) were taken.

4.1   The UHV Systems

4.1.1   UPS System

The system for UPS is composed of a preparation chamber and a main chamber. The preparation chamber is equipped with an evaporator, a quartz crystal, an ion gun for sputtering, LEED and AES optics and a mass spectrometer. The UPS measurements were performed in the main chamber using a rotatable VSW HA 100 hemispherical analyser and a Specs UVS 300 helium discharge lamp as source for UV radiation.

Figure 4.1 shows the operating principle of a hemispherical analyser. The lens at the entry focuses the electrons emitted from the sample. A deflection potential V_o is applied in order to select those electrons with kinetic energy $E_o = eV_o \cdot (R_1 \cdot R_2 / (R_2^2 - R_1^2))$. The resolution of the analyzer was about
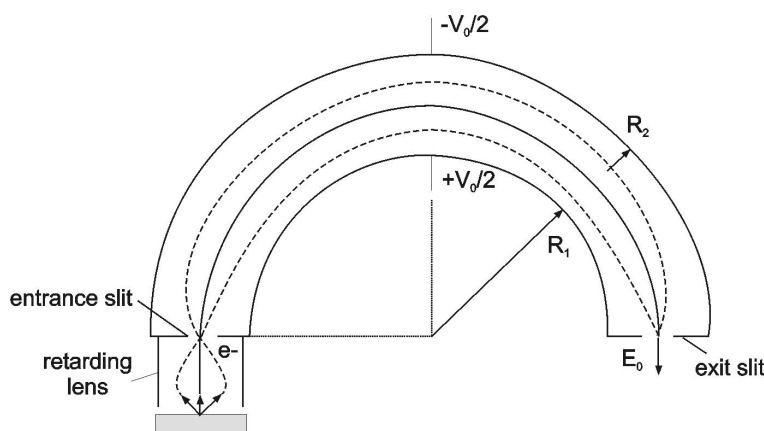
Figure 4.1: Schematic picture of a hemispherical deflection analyser

100 meV (pass energy E_o of the analyzer set to 10 eV). A spectrum of a gold sample was taken for the energy calibration with both He(I) and He(II) lines since the Fermi edge is quite well visible for this material.

The UV discharge lamp generates a high density plasma by guiding the electrons extracted from a hot cathode filament along the lines of a strongly inhomogeneous magnetic field towards the small discharge region. The strong ultraviolet radiation emitted from this dense plasma is extracted from the cathode side by the combination of a metal and a quartz capillary.

4.1.2   System at Bessy II

The system at Bessy II is equipped with a 150 VG hemispherical analyser with three channeltrons. The XPS spectra were taken with a photon energy of 630 eV. We therefore obtained good surface sensitivity since the kinetic energy of electrons coming from the V 2p and O 1s levels was around 100 eV corresponding to a short electron escape depth. The energy scale was calibrated relative to the Au $4f_{7/2}$ energy by taking a spectrum of the gold sample. The photon beam was incident at 55° to the sample surface normal and electrons were recorded in normal emission. NEXAFS spectra were collected using the Auger yield mode. The spectra were normalized to the beam current. The analyser was positioned at an angle of 55° relative to the photon beam.
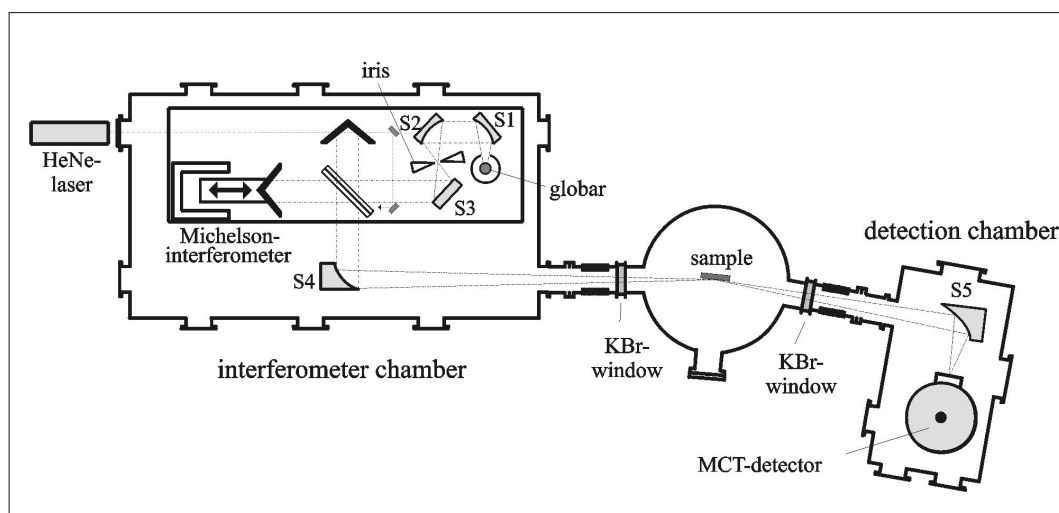
Figure 4.2: Setup of the infrared interferometer chamber

4.1.3 Vibrational Spectroscopy System

Like the other two systems, the vibrational spectroscopy system consists of
a preparation chamber and a measurement chamber. It has in addition an
infrared interferometer chamber (operated at ca. $7 \cdot 10^{-3}$ mbar) and a de-
tection chamber (under constant nitrogen pressure). These two chambers
are connected to the UHV chamber via KBr-windows. A globar - a silicon
carbide pin- is the source for the infrared light, heated up to 1400K. Fig-
ure 4.2 shows the setup of the infrared interferometer chamber. The angle
of incidence of the light is roughly 85° relative to the normal of the sam-
ple. The infrared light detector is a Mercury-Cadmium-Telluride-detector
(MCT-detector). The measured interferogram is then Fourier transformed
into a spectrum. The whole characteristics of the light source and the op-
tical elements are detected by the measurement. Thus, for the detection of
(less intense) vibrations of molecules in the surface, two measurements are
required: the first one of the clean sample ("background spectrum") and
the second one after adsorption. The two spectra are divided by each other.
Thus one obtains the change of reflectivity of the surface. Adsorbates give
rise to characteristic absorption bands.

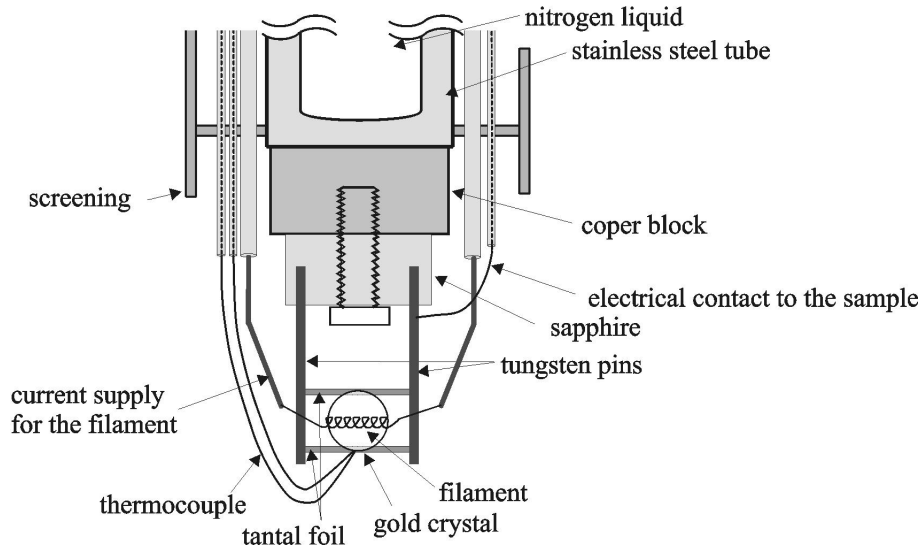For the HREELS measurements, a Specs delta 0.5 electron energy loss

Figure 4.3: Setup of the sample holder at the end of the manipulator

spectrometer in the measurement chamber was used. Its construction has been developed by Ibach and his group [43]. The electrons are emitted from the LaB_6 cathode and then go through two monochromators. A special construction of these two monochromators permits a very good energy resolution with a high energy flux. The electron beam is focussed on the sample where it is reflected. The reflected beam is then focussed on the entrance slit of the analyzer.

4.2   Sample Setup

Figure 4.3 shows the sample holder and its setup at the end of the manipulator. The sample is a gold (tungsten) crystal of diameter 10 (6) mm and thickness 2 mm. Two slits were made at the side of the crystal which allow the holding of the crystal by two thin tantalum foils. The tantalum foils are spot welded to the tungsten pins. These pins and so the sample are electrically isolated from the manipulator by the sapphire block. To heat the sample, a tungsten filament is placed on the back side of the sample.

Through the electrical contact to the sample, one can apply a voltage to the sample and thus heat the sample more quickly by bombardment of electrons emitted from the filament towards the sample.

Chapter 5

Growth of Vanadium Oxides

5.1 $V_xO_y/Au(100)$

Figure 5.1 shows the crystal structure and lattice parameter of gold and VO. Gold is a face centered cubic metal. Its face (110) has therefore C_{4v} symmetry and the primitive unit cell is a square of parameter a_{nn}. VO has a NaCl type oxide structure, that is a face centered cubic lattice structure with a two atoms motif. Thus the primitive unit cell is also a square. As one can see from figure 5.1, the lattice parameter of gold and VO are very close. Therefore we tried to grow VO(100) on Au(100). Della Negra et al. [44, 45] showed that VO(110) can be grown on $TiO_2(110)$ and Kishi et al. made thin films of VO(111) on Ni(110) [46] and on Cu(100) [47]. To
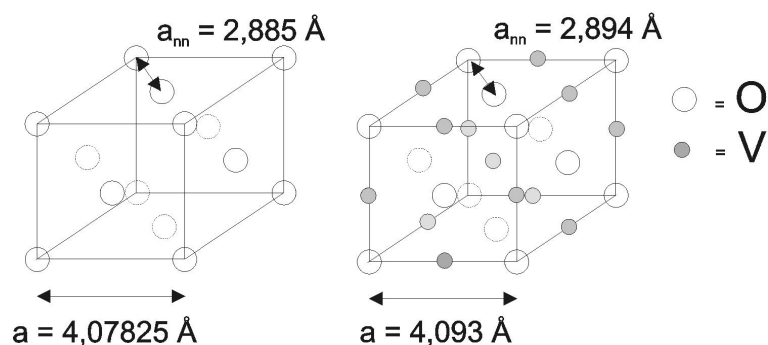
Figure 5.1: Crystal structure of Au (left) and VO (right)

$a_b = 4,07825$ Å

$a_{nn} = a_b/\sqrt{2} = 2,885$ Å

$a_1 = 0,9\ a_{nn} = a_6$

$a_2 = 1,008\ a_{nn} = a_4 = a_5$

$a_3 = 0,965\ a_{nn}$

$\overline{a} = 0,9615\ a_{nn} = 2,774$ Å

unit cell   ● bulk atom   ● surface atom
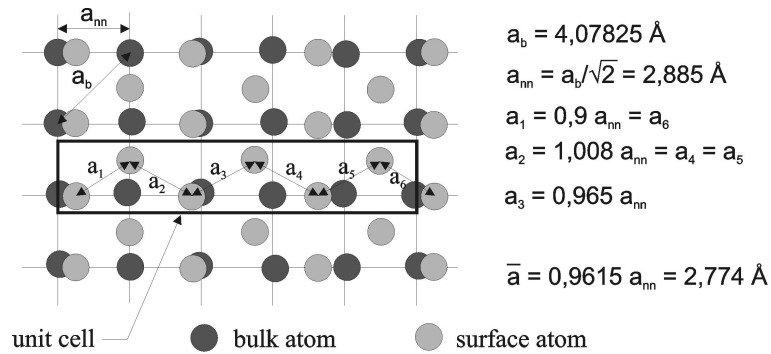
Figure 5.2: Model based on a (1x5) reconstruction for the Au(100) surface after [49]

our knowledge, no thin film VO(100) has been grown yet. It is therefore an interesting attempt to try to grow VO(100). But as other clean metal surfaces, the (100) surface of gold reconstructs [48] and may therefore cause some problems. The complicated reconstruction pattern c(26x68) observed by LEED [48] may be approximated by a rectangular (1x5) cell [49]. The model is shown in figure 5.2.

Au(100) substrate was cleaned in UHV by alternating cycles of 30 minutes up to one hour Argon sputtering and annealing at 1150 K. The LEED pattern obtained is shown in figure 5.3. The spot corresponding to the (0,0,0) (Γ) point of the reciprocal lattice is not in the center of the screen because the gold crystal surface was not exactly perpendicular to the electron beam of the LEED. One recognizes the principal spots forming a square unit cell corresponding to the bulk structure. Between them one can see other groups of two or three spots. These groups are located at regular intervals equal to one fifth of the length of the square side. These intervals are therefore in agreement with the simple (1x5) reconstruction model presented in figure 5.2. As mentioned above, the reconstruction is more complicated, so that there are several spots instead of only one at each of the four sites between the principal spots.

The vanadium oxide thin films were prepared by evaporating metallic vanadium in an oxygen atmosphere followed by annealing in oxygen to different temperatures from 800 up to 950 K. The LEED patterns obtained are
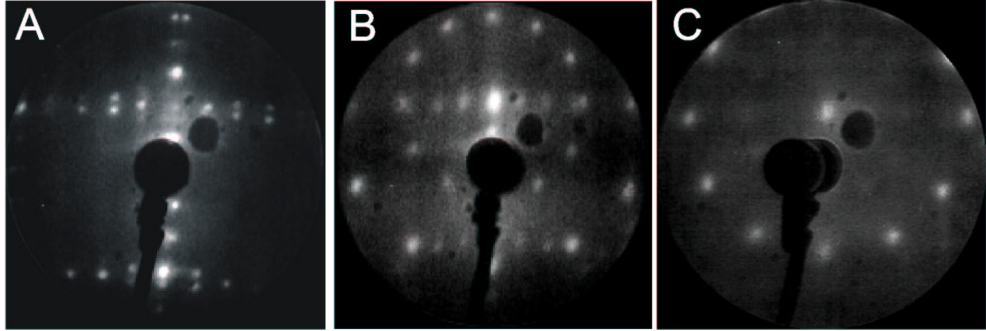
Figure 5.3: LEED patterns obtained for the Au(100) substrate (A) and 2 monolayers (B) and 12 monolayers (C) of vanadium oxide on it at 40 eV

shown in figure 5.3 B and C. In figure 5.3 B, one can see the LEED pattern obtained after little vanadium oxide has been grown. The spots of the Au(100) substrate are still visible. After longer deposition, they disappear and one sees only the spots coming from the vanadium oxide. These consist of successive rings of twelve spots each. As already mentioned, VO is a cubic face centered material and so its face (100) is of C_{4v} symmetry. The corresponding LEED pattern should therefore be of square type. By contrast, its (111) face is of C_{3v} symmetry and thus shows a hexagonal type LEED pattern. As the substrate is of C_{4v} symmetry, the VO(111) thin film would show several domains rotated relative to each other by 90°. The resulted LEED patterns are then rings such as those we observe in figure 5.3.

One can calculate the primitive vectors of VO(111) in reciprocal space. Taking for the primitive vectors in real space:

$$\vec{a_1} = (a, 0)$$
$$\vec{a_2} = (-\frac{a}{2}, \frac{\sqrt{3}a}{2})$$

(5.1)

and applying the method presented in section 3.1.2, one finds:

$$\vec{a_1^*} = 2\pi(1/a, \frac{1}{\sqrt{3}a})$$
$$\vec{a_2^*} = 2\pi(0, \frac{2}{\sqrt{3}a})$$

(5.2)

where a = 2.894 Å as shows figure 5.1. By the same procedure, one obtains

for gold:

$$\overrightarrow{a_1^*} = 2\pi(1/b, 0)$$
$$\overrightarrow{a_2^*} = 2\pi(0, 1/b) \tag{5.3}$$

with b = 2.885 Å. By looking at figure 5.3 B with attention, one can see actually two rings corresponding to the vanadium oxide. According to equations 5.2 and 5.3, the spots corresponding to the first-order diffraction of VO(111) should be in the vicinity of the spots coming from gold (at a distance $d_{VO} = \frac{2}{\sqrt{3}} \cdot d_{Au} \simeq 1.15 d_{Au}$ from the center). This would correspond to the second ring observed on figure 5.3. But one should not forget that vanadium can take different valence states when it bonds with oxygen (see the complex phase diagram in appendix A). We shall therefore consider different vanadium oxides and look for their symmetry and corresponding LEED pattern. One will then obtain the possibility of having $V_2O_3(111)$ on the Au(100) surface. The primitive vectors in the reciprocal space given in equation 5.2 are valid for $V_2O_3(111)$ also, but here a = 4.9515 Å. The first-order diffraction spots for $V_2O_3(111)$ will therefore appear at a distance $d_{V_2O_3} = \frac{2b}{a\sqrt{3}} \cdot d_{Au} \simeq 0.66 \ d_{Au}$. The second-order diffraction spots are at a distance $d'_{V_2O_3} = \frac{2b}{a} \cdot d_{Au} \simeq 1.16 d_{Au}$. Hence one sees this is in good agreement with the observed LEED pattern. Nevertheless, as VO(111) is a polar surface, a reconstruction could occur to eliminate the electrostatic potential in the film (see section 2.2.2) in order to stabilize the surface. A $(\sqrt{3} \times \sqrt{3})$ reconstruction type would fit to the LEED pattern we observed. Such a reconstruction has not been reported in the literature but a (2×2) reconstruction [47, 46]. Therefore, we can conclude that the thin film grown on Au(100) is V_2O_3.

As reported in [44, 45, 46, 47], the VO thin films were obtained only for very small coverage or for the substrate TiO_2 under very particular experimental conditions. This allows one to think that it may be possible to grow VO on Au(100) but that the most stable phase is V_2O_3.

5.2 V$_2$O$_3$(0001)/Au(111) and /W(110)

The preparation process for the growth of V$_2$O$_3$ thin films on the gold and tungsten substrates consists of three steps. The first one is the cleaning of the substrate surface. Au(111) substrate was cleaned in UHV by alternating cycles of 30 minutes up to one hour Argon sputtering and annealing at 1150 K. To remove carbon from W(110) we repeated the usual cleaning cycle consisting of heating the sample first to 1800 K in 10^{-6} mbar of oxygen during a few minutes and then to 2300 K without oxygen. In the second step the metallic vanadium is evaporated in an oxygen atmosphere (10^{-7} mbar) at room temperature. The evaporator has been calibrated using a quartz crystal to the evaporation rate of 1 Å per minute. Annealing at 700 K in 5.10^{-8} mbar of oxygen constitutes the last step of the preparation process. In the beginning phase of this work, preparation cycles of each about 10 minutes evaporation and 10 minutes annealing were performed in order to find the best growth process. Later, as the preparation method was optimized, vanadium was evaporated for 30 minutes and the film annealed for about 15 minutes. The vanadium oxide so obtained is stable under UHV conditions (10^{-10} mbar) up to high temperatures (at least 1050 K). However, heating to higher temperatures than 800 K leads to diffusion of gold atoms towards the surface, as we shall see in section 5.2.3. This diffusion phenomenon does not occur with the tungsten substrate.

5.2.1 Characterization of the Growth by LEED and AES

Figure 5.4 shows the geometrical structures of the W(110) and Au(111) faces and how they fit for the epitaxial growth of V$_2$O$_3$(0001). Gold is a face centered cubic metal and therefore the (111) face is hexagonal as can be observed in the LEED pattern, on the left side of figure 5.5.

V$_2$O$_3$ has corundum structure like Al$_2$O$_3$, i.e. the oxygen atoms form a hexagonal lattice and two third of its octahedral sites are occupied by vanadium atoms. The parameter of the gold lattice (2.885 Å) and of the
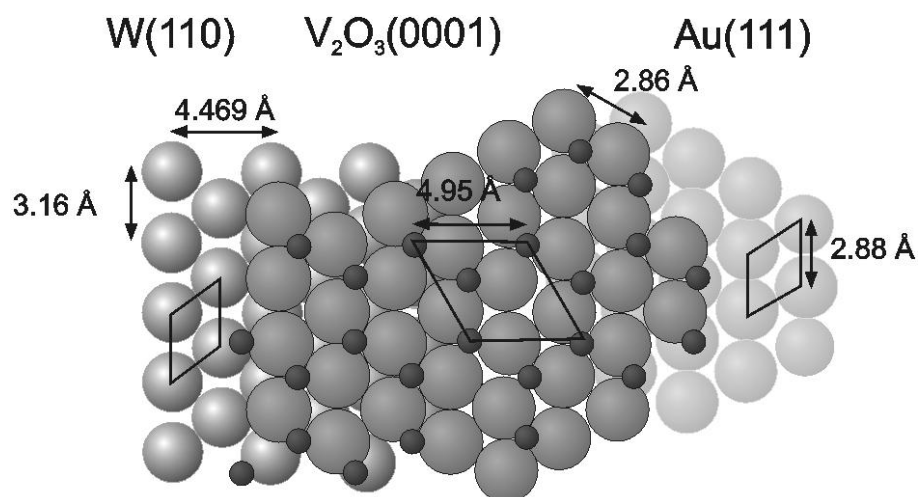
Figure 5.4: Lattice parameter for the epitaxial growth of $V_2O_3(0001)$ on W(110) (left) and Au(111) (right)
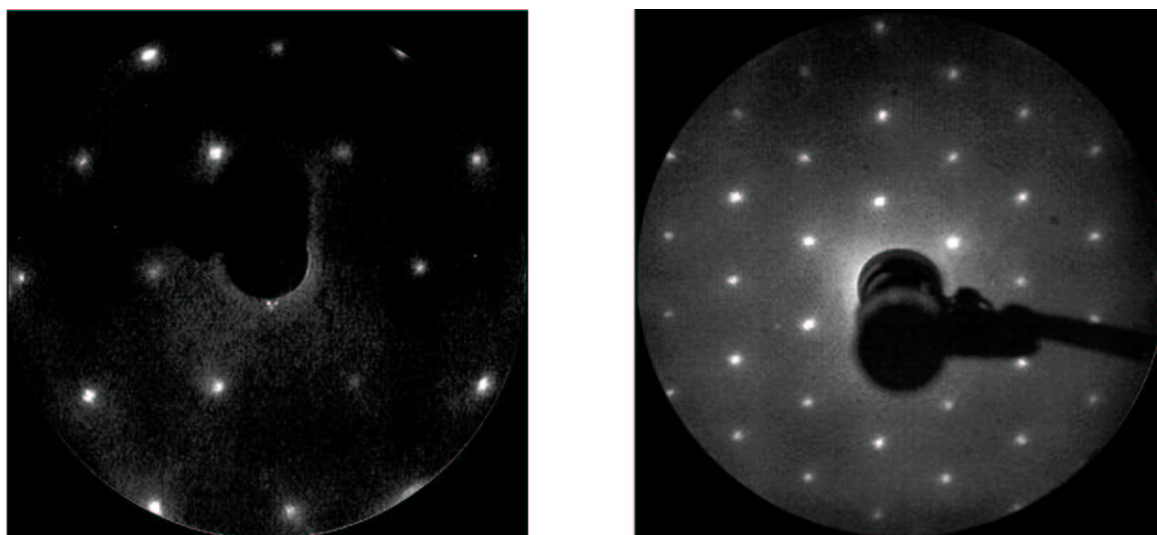

Figure 5.5: LEED pattern of the Au(111) substrate at 175 eV (left) and $V_2O_3(0001)$/Au(111) at 150 eV (right)
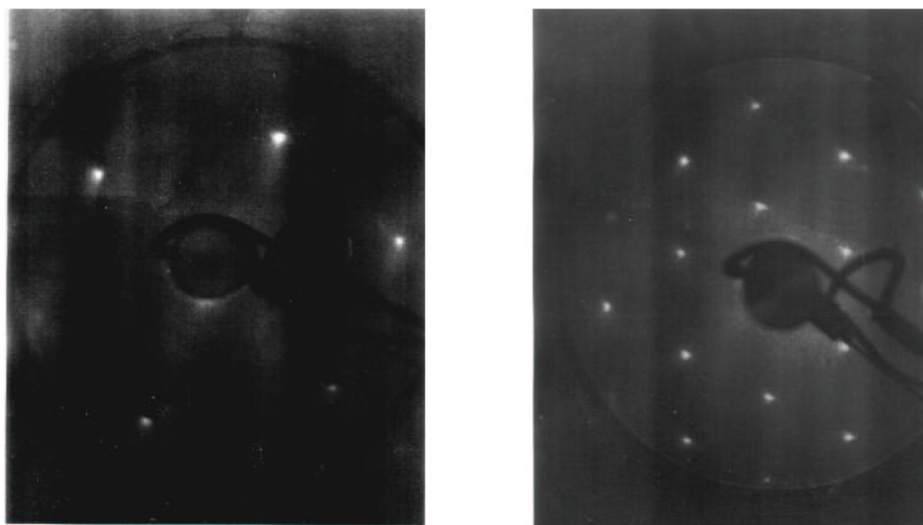
Figure 5.6:   LEED pattern of the W(110) substrate (left) and V₂O₃(0001)/W(110)(right) both at 100 eV

oxygen lattice in V_2O_3 (2.86 Å) are very close, which is a good basis for epitaxial growth. The LEED pattern of the $V_2O_3(0001)/Au(111)$ film on the right side of figure 5.5 indeed exhibits sharp reflexes, corresponding to a well-ordered structure.

Tungsten is a body centered cubic metal. The (110) face is quasi-hexagonal, as figure 5.4 shows. The mismatch between the V_2O_3 oxygen lattice and W(110) in the [001] direction of W is about 10%. In spite of the mismatch, the good quality of the LEED pattern for a 30 Å thick film provides evidence for satisfactory epitaxial growth on W(110) as well, see figure 5.6.

To control the deposition of the vanadium and oxygen atoms, AES measurements were performed. The result for the growth on Au(111) and on W(110) is displayed in figure 5.7 and shows that a 30 Å thick film completely covers the substrate surface. The Auger electron spectrum for the Au clean substrate shows two features at 240 and 256 eV, which correspond to gold. The low cross section for the concerned Auger transition of gold is the cause for the observed low signal/noise ratio. After deposition of vanadium in an oxygen atmosphere, we mainly observe three new features at 437, 473 and 509 eV, corresponding to vanadium (437, 473 eV) and oxygen (509
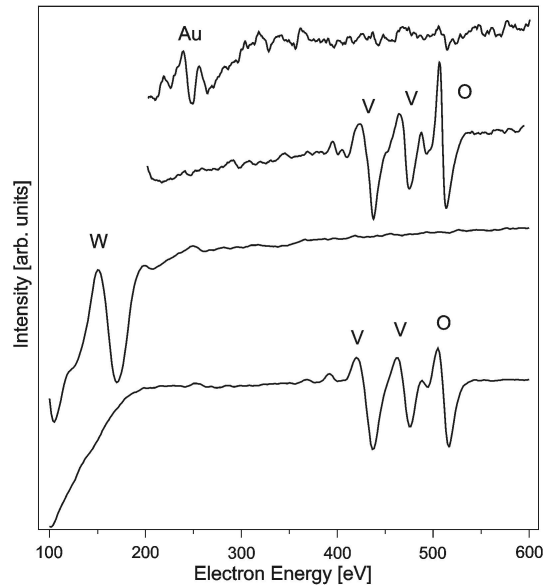
Figure 5.7: AES spectra for the Au(111) substrate and 30 Å $V_2O_3(0001)$/Au(111) (top) and W(110) substrate and 30 Å $V_2O_3(0001)$/W(110) with primary electron energy of 2.5 keV

eV). The spectrum for tungsten displays one broad feature at 170 eV. The spectrum for $V_2O_3(0001)$/W(110) displays similar features as the spectrum for $V_2O_3(0001)$/Au(111).

5.2.2 Characterization of the Stoichiometry with XPS and NEXAFS

In order to characterize the stoichiometry of the V_2O_3 film thus obtained XPS and NEXAFS measurements were performed. The result for XPS is shown in figure 5.8. One can recognize three features, the first two at lower binding energies correspond to V $2p_{1/2}$ and $2p_{3/2}$, the feature at higher binding energies originates from O 1s. As already discussed in the literature [2, 50, 51, 52] the position of the O 1s peak for vanadium oxides depends only weakly on the vanadium oxidation state. More relevant parameters for the determination of the stoichiometry of the oxide are the distance between the O 1s and V 2p signals, the FWHM and the shape of the spectra [1]. Our
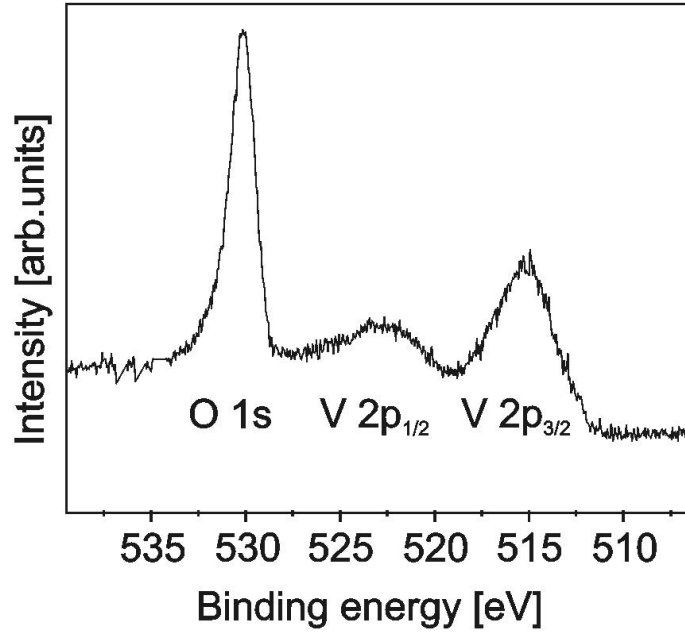
Figure 5.8: XPS spectrum of the V 2p and O 1s core levels for $V_2O_3(0001)/Au(111)$

spectra show good agreement with those found in the literature for V_2O_3 single crystals [53, 54, 55, 56].

As we previously discussed in section 3.2 X-ray absorption spectra correspond to electronic transitions from an occupied level to an unoccupied level just above the Fermi level. This has consequences on the dipole selection rules which in turn gives this spectroscopic method its site and symmetry properties [12]. To a first approximation, the peak positions of the metal L-edge features are related to the formal oxidation state of the parent metal [35]. NEXAFS measurements were therefore performed for the V L-edge of the $V_2O_3(0001)/Au(111)$ film in order to characterize its stoichiometry. The spectrum is shown in figure 5.9. The spectrum corresponds to transitions from the ground state ($2p^63d^2$) to a final state ($2p^53d^3$) and exhibits two broad structures (L_{III} and L_{II}), corresponding to the splitting of the initial state into $2p_{3/2}$ and $2p_{1/2}$ respectively. However, other interactions like the 3d-3d and the 2p-3d interactions play an important part in the X-ray absorption process [36] and have to be taken into account to explain such spectra
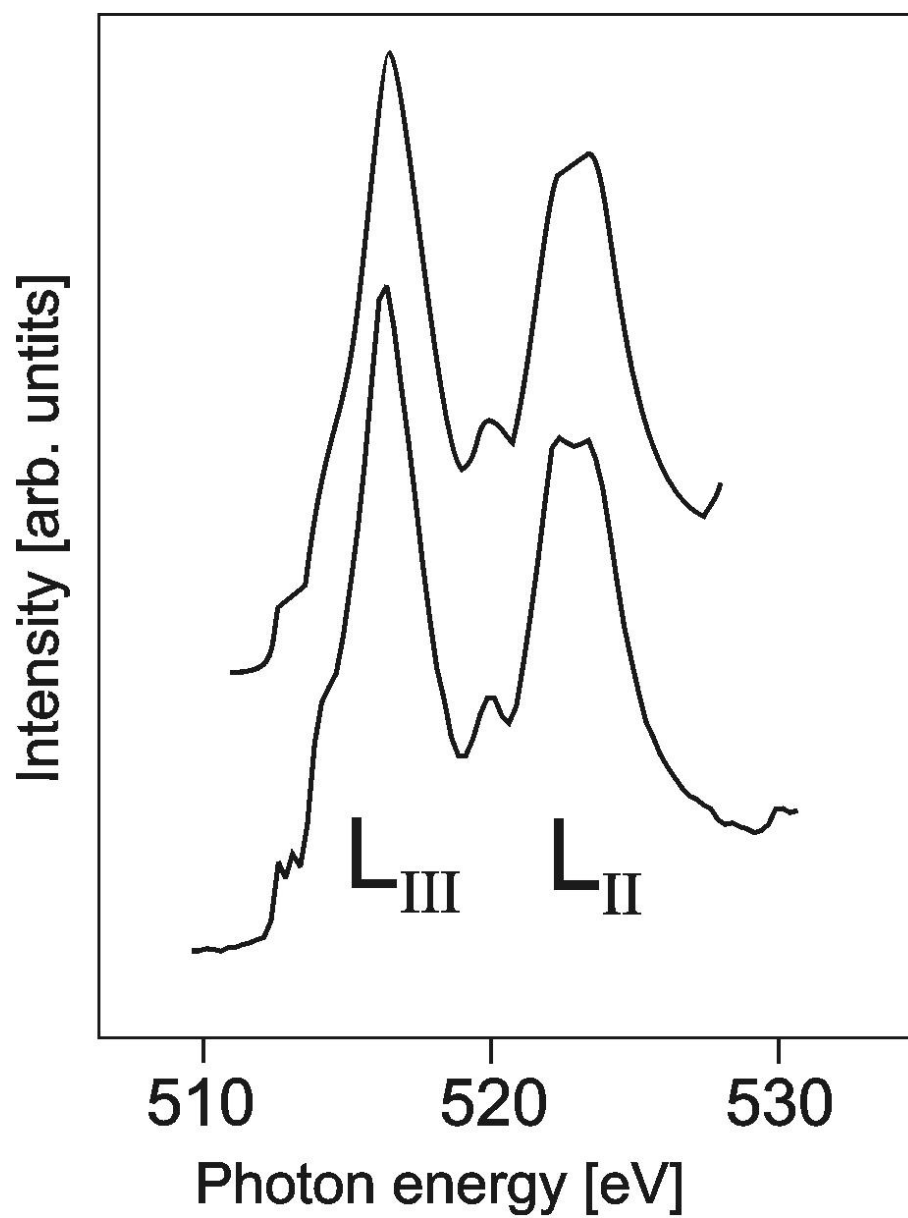
Figure 5.9: V L-edge NEXAFS of $V_2O_3(0001)/Au(111)$ (bottom) and V_2O_3 single crystal from [37] (top)

correctly. In [37] Abbate et al. showed V L-edge spectra of V_2O_3, VO_2 and V_2O_5. Their spectra exhibit noticeable chemical shifts characteristic of the different vanadium valencies and the shape of the spectra depends implicitly on the point-group symmetry of the compound [37]. This property is supported by theoretical calculations of X-ray absorption spectra for different valencies of a same element [36, 57]. This means that one can determine the valency and structure of a vanadium oxide by comparing the X-ray absorption spectrum with reference spectra. Hence the spectrum obtained for a single crystal of V_2O_3 in [37] is also shown in figure 5.9 . The comparison with our spectrum leads to the conclusion that the film grown on Au(111) is effectively identical in terms of its electronic structure to a single crystal of V_2O_3.

5.2.3 Diffusion of Gold to the Surface

Two different preparation methods for growing V_2O_3 on Au(111) were studied by means of NEXAFS. The first one is the same as described above, the second one differs from the first one only in the annealing temperature. For the first preparation method it was 400ºC and 500ºC for the second. We shall therefore call the first one the "low-temperature preparation" and the second the "high-temperature preparation". For the high-temperature preparation, three cycles of ten minutes deposition and ten minutes annealing were made. The L-edge NEXAF spectra obtained for both preparation methods are shown in figure 5.10 with the corresponding XP spectra of the Au $4f_{7/2}$ shell. The V L-edge NEXAF spectrum for the V_2O_3 film after only one high-temperature preparation cycle has a different shape than the spectrum for the V_2O_3 film obtained by the low-temperature preparation. By continuing the high-temperature preparation cycles, the features change smoothly towards those of the spectrum of the film obtained by the low-temperature preparation. On the other hand, the O K-edge spectra for both preparation methods are very similar and for that reason not shown here (the O K-edge spectrum of $V_2O_3(0001)/Au(111)$ will be discussed in chapter 6). In figure 5.10, one can recognize for the films obtained by the high-temperature preparation
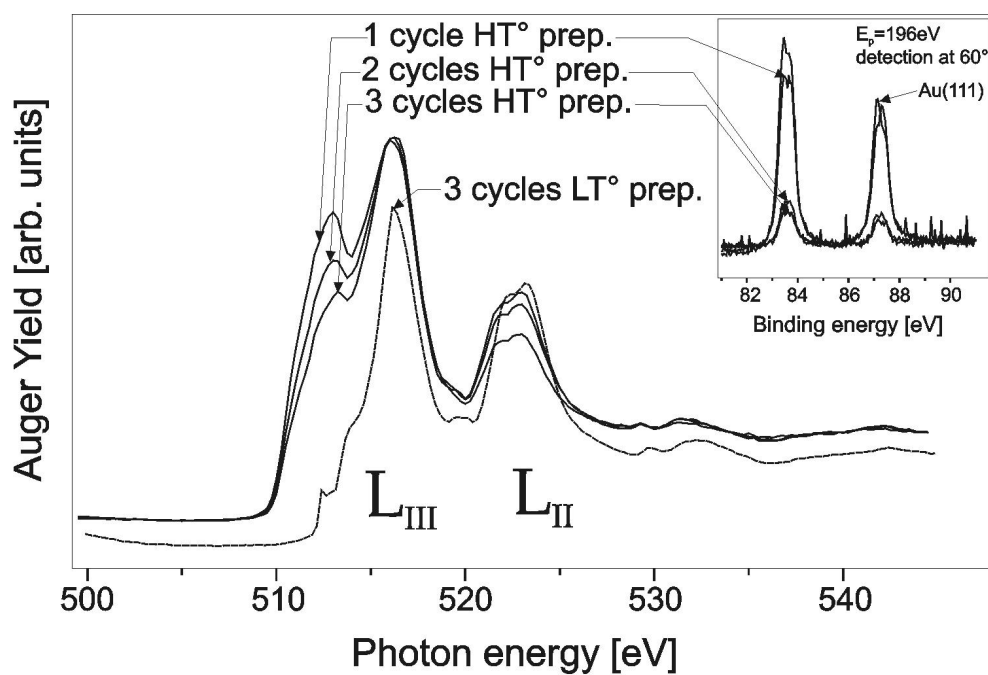
Figure 5.10: L-edge NEXAFS results for $V_2O_3(0001)/Au(111)$ obtained by the "low-temperature preparation" (annealing at 400ºC) and by the "high-temperature preparation" (annealing at 500ºC). Inset: Au $4f_{7/2}$ XP spectra for the thin film after each "high-temperature preparation" cycle

four features at around 513, 517, 522 and 523 eV. The latter three are to be found on the spectrum obtained after the low-temperature preparation but with differences in the intensity. In the energy range where the first, broad and intense feature occurs, the spectrum for the low-temperature preparation shows only two less intense features. Finally, the small feature at 520 eV in the spectrum for the low-temperature preparation does not appear for the high-temperature preparation. Looking at the XP spectra shown in figure 5.10 allows one to understand that the differences in the V L-edge spectra just described come from the presence of gold on the surface. The XP spectra evidence a diffusion phenomenon of the gold atoms toward the surface by the high-temperature preparation. Since this phenomenon does not occur for the low-temperature preparation, one can conclude that the temperature threshold for the gold diffusion through the vanadium oxide is between 400^oC and 500^oC. The shape of the V L-edge spectra for the high-temperature preparation is very similar to the one obtained for $3d^0$ compounds, for instance for a Ti^{4+} ion in an octahedral environment [12]. As we have already discussed in section 3.2.3 the L-edge spectra for $3d^0$ compounds can easily be interpreted within a single-electron scheme. The four observed features correspond to the 2p spin-orbit splitting and the 3d crystal-field splitting and are described as $L_{III} - t_{2g}, L_{III} - e_g, L_{II} - t_{2g}$ and $L_{II} - e_g$, respectively. In this single-particle approximation, the intensity ratio of the L_{III}/L_{II} features should be related to the ratio of the ground state populations in the $2p_{3/2}$ and $2p_{1/2}$ orbitals, which is 2:1. After one high-temperature preparation cycle the quantity of gold present at the surface seems to be very high. Supposing there is one gold atom for one vanadium atom leads to a formal $3d^0$ state for the vanadium, supposing gold has the valency +1, giving up its 6s electron. The most striking change in the spectrum by increasing the number of high-temperature preparation cycles is the decrease of the first feature corresponding to the $2p^{3/2} \rightarrow t_{2g}$ transition while the second feature corresponding to $2p^{3/2} \rightarrow e_g$ remains the same. In our simple model, this can be related to the slow population of the t_{2g} level as the vanadium quantity increases. This trend is also observed for the L_{II} feature but much less. The LEED patterns obtained for both preparation methods are exactly the same so that one can suppose that

we are concerned with an alloying of substitution type where gold atoms occupy regular vanadium sites. As Au^+ has a larger radius as V^{5+}, the lattice may be distorted, changing the symmetry of the ground state and consequently the transition probability through Fermi's Golden Rule. This could explain the abnormalities observed in the t_{2g}/e_g intensity ratios.

5.3   Termination of the $V_2O_3(0001)$ Surface

It has been shown so far that a thin film of stoichiometric V_2O_3 on Au(111) and W(110) can be produced that exhibits the same electronic structure as single crystals. But the termination of the surface has not been discussed yet. All the experimental data collected in the frame of this work infer that the $V_2O_3(0001)$ exhibit two different surface terminations. Which termination one obtains is determined by the preparation process. The first one is obtained immediately after the preparation process describes in section 5.2, which ends with an annealing in oxygen. The second surface is obtained from the first one by heating the sample up to 600 K by electron bombardment for a short time (few seconds). This process is reversible: annealing the second surface in oxygen leads to the first one again.

We are going to show here only IRAS measurements to illustrate our central result concerning the two different terminations. The results obtained with other experimental methods are shown and discussed in chapter 6 and 7. IRAS measurements were performed for both terminations and the spectrum obtained for the first termination was divided by the one corresponding to the second termination. The result, shown in figure 5.11, exhibits only one peak at 127 meV (=1023 cm^{-1}). A peak at the same energy has already been observed for $V_2O_5(001)$ by HREELS and assigned to the V-O stretching vibration of vanadyl groups (V=O) [2]. Netzer et al. showed also the existence of vanadyl groups in $V_2O_3(0001)/Pd(111)$ [58]. A similar phenomenon on the corundum $Cr_2O_3(0001)/Cr(110)$ has been already discussed in [59, 60]: formation of chromyl groups could be observed on this surface upon adsorption of oxygen followed by annealing at room temperature. In the following we will call the first surface termination with the vanadyl species the -V=O ter-
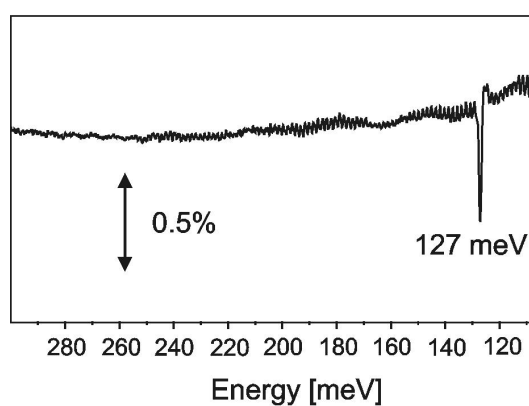
Figure 5.11: IRAS: spectrum for -V=O termination divided by spectrum for -V termination. The absorption peak corresponds to the V-O stretching vibration of the vanadyl groups

mination and the other one, where the V=O groups have been removed, the -V termination. AES could not detect any difference between these surfaces. It indicates that the removal process of the vanadyl oxygens by heating the sample concerns only the surface and has no effect on the bulk stoichiometry.

Chapter 6

Electronic Structure of V$_2$O$_3$(0001)

6.1 Electronic Structure of V$_2$O$_3$ in the Literature

V$_2$O$_3$ has been the object of many theoretical and experimental works because of its very rich phase diagram. Particulary, its transition at 150K from a paramagnetic metallic (PM) rhombohedral (corundum) phase to an antiferromagnetic insulating (AFI) monoclinic phase with unusual magnetic structure (ferromagnetic coupling in hexagonal (110) layers and moment reversal between adjacent layers [61]) has still not been completely understood. Here, we present a short (and due to the extremely large number of papers about V$_2$O$_3$ not exhaustive) review of the experimental works done on V$_2$O$_3$ and the different theories proposed to explain its metal-insulator transition. For a more detailed insight into the interplay between experiment and theory on the subject see [62, 63] and references therein.

The V ion in V$_2$O$_3$ is in the 3d^2 configuration. In the corundum phase (metallic) the V^{3+} cations occupy two thirds of the octahedral sites of the hexagonal packing formed by the anions O^{2-}. A trigonal distortion is associated with the corundum structure which causes the splitting of the t$_{2g}$ orbital into a nondegenerate a$_{1g}$ and a doubly degenerate e$_g^\Pi$ orbital. The a$_{1g}$ orbital

has lobes directed along the $\overrightarrow{c_H}$ vector of the hexagonal basis, while the e_g^Π lobes are more within the $(\overrightarrow{a_H}, \overrightarrow{b_H})$ basal plane. The oxygen octahedra share faces along the c_H axis and so the shortest V-V distance is along that axis [64]. Therefore the overlap integral between the a_{1g} electrons has a larger value along the c_H axis than in the basal plane. For this reason, Castellani et al. [65] assumed the formation of a molecular bond between the a_{1g} orbitals of V-V vertical pairs spread into a band. Since this molecular bond can accept two electrons for a V-V pair there is only one (magnetic) electron at each V site that occupies one of the 2-fold degenerate e_g^Π orbitals, leading to a ground state S=1/2. This model of orbital ordering has been successfully used to explain many experimental results [66, 67, 68, 69]. Hertel and Appel [70] adopted this picture also to perform their calculations but considered a unit cell containing two V_2 pairs so that the molecular bonding band can accomodate only 1/2 electron per V. Arguing that c/a is too large (V_2O_3 has the largest c/a ratio among Ti_2O_3, Cr_2O_3 and $\alpha - Fe_2O_3$) for a_{1g} to couple between two vertical V cations, Ivanov [71] and Ezhov et al. [72] contradicted the molecular orbital picture and Ivanov moreover claimed that the unit cell contains only two cations. However, an inspection of the literature shows that the electronic structure of V_2O_3 is very controversial. The first attempt to model the band structure of V_2O_3 was made by Goodenough [73]. In his simple model the a_{1g} orbital lies higher than the doubly degenerate e_g^Π and they overlap in the metallic phase. In the model of Castellani et al. [65] the a_{1g} orbitals lie much lower than the e_g^Π orbitals due to their molecular bonding and so their contribution to the total DOS at E_F in the metallic phase is negligible and the variation of its population in the two phases plays little role. This idea that the thermodynamic, transport and magnetic properties are governed by e_g^Π electrons is widely accepted by both theoreticians and experimentalists [70, 71, 72, 74, 75, 76, 77, 78] but most of them do not agree with the low spin S=1/2 and propose a predominantly e_g^2 high spin S=1 for the ground state. Nevertheless the band structure calculation performed by Mattheiss [79] indicate that the partially filled bands at the Fermi surface involve all 5 a_{1g}, e_g^Π and e_g^σ states.

Slater [80] was the first to propose an explanation for the PM to AFI tran-

sition. He argued that due to the antiferromagnetic order the period is twice the lattice spacing, so that the bands develop gaps in the middle. Castellani et al. [65] described the AFI phase of V_2O_3 as an insulating state of the Mott-Hubbard-Slater type in which the electrons localize in the way suggested by Mott due to the Hubbard short range repulsion U. Mott [81] showed that the conducting properties of an array of atoms with antiferromagnetic spin arrangement depend on the lattice parameter: it will be metallic for a smaller one and insulator for a larger one. With this argument one can easily understand the importance of the V-V distances, i.e of the c/a ratio in V_2O_3. The geometric argument used in the explanation of the PM to AFI transition is controversial also. We have already shortly mentioned the argument of a large c/a ratio used by many authors to reject the molecular orbital picture [71], arguing that the hopping integral between a V-V vertical pair is smaller than the Hubbard U [72]. Castellani et al. [65] argued that the lattice distortion only cooperates with the interelectronic correlation mechanism -that would occur anyway- by increasing the width of the gap due to the reduction of the hopping integral along the distortion direction. Thus the distortion is not the cause of the transition to an insulator state but in contrary its result. The trigonal symmetry is lost in the AFI phase because correlation between electrons in a doubly degenerate band favors the magnetic order observed. By contrast, other authors see the explanation for the magnetic and electronic transition in the crystallographic transformation during the transition. The volume expansion of 3.5% observed for the AFI phase is due to an increasing of the V-V distance along the distortion direction, the V-O distances remaining essentially unchanged. Goodenough first [73] assumed a splitting of the e_g^Π orbitals because of this V-V distance increasing and more recently Taylor et al. [64] claimed a presence of spatial correlation to explain the transition. Namely the increasing of this V-V distance explains the absence of V-V interactions, leading to local V moments.

Finally, one should cite the work of Mila et al. [82, 83] who have tried to find a new model consistent with all experimental results. They assumed a strong hybridization of the V pair along the trigonal axis and considered the in plane V-V interactions as a perturbation of these V-V pair molecules.

Thus they got a ground state S=2 for the V pair, because it is energetically favorable for the electron spin down on the a_{1g} bonding orbital to flip its spin and to move to an available e_g^{Π} level on one or the other of the V ions.

6.2   Valence Band

To our knowledge the results of UPS measurements reported in the literature only concern V_2O_3 single crystals [53, 54, 56, 84, 85, 86, 87, 88, 89, 90]. Since UPS is a surface sensitive spectroscopic method we used it to study the surface electronic structure of the V_2O_3 film with both -V and -V=O terminations.

We firstly show in figure 6.1 a He I spectrum for each termination at room temperature taken with an angle of incidence of 45º with respect to the surface normal and at normal electron emission. One can distinguish three bands of emission. The first and least intense one between E_F and about 3.5 eV originates from the V 3d bands. The second in the middle from about 3.5 to 9.5 eV corresponds to the O 2p band. The last one arises from secondary electrons. The assignment for the first two features corresponds to an interpretation in terms of a simple ionic picture but band structure calculations [79, 53, 91] and theoretical analysis of core level spectra [85] show evidence for a strong V 3d-O 2p hybridization. The emission of the V 3d and O 2p bands are not separated by the 2 eV gap predicted by theory. This effect has been attributed to a hole life time broadening [89]. As explained in section 3.2, the low energy cutoff gives us information about the work function of the material. We find a difference of about 0.8 eV between the two terminations. This is not surprising since the vanadyl species form a dipole with its negative end directed away from the surface, which increases the work function. Differences between the spectra for the two terminations are to be seen and they have been investigated more thoroughly using He II angle resolved photoelectron spectroscopy. The results are presented in the following paragraph.

We performed a measurement series for 6 light angles of incidence (0, 15º, 30º, 45º, 60º and 75º) and the same 6 emission angles, the detector
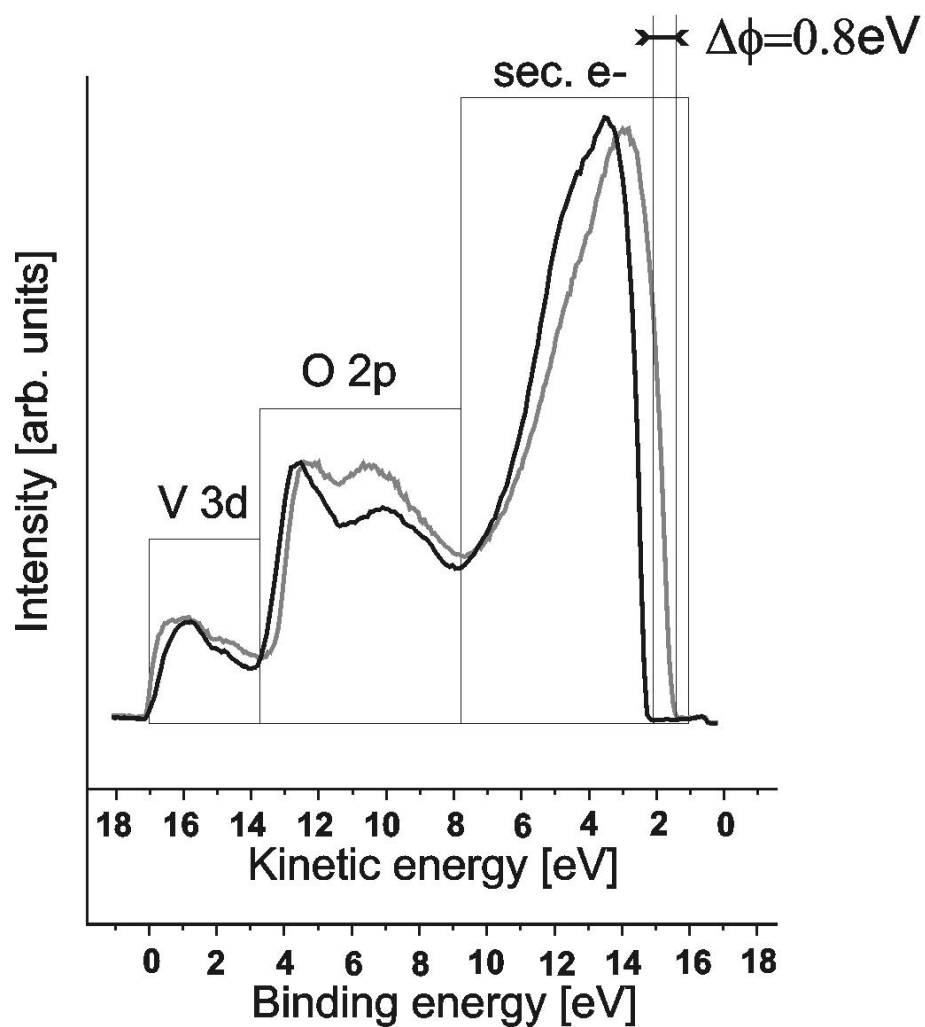
Figure 6.1: UPS (HeI) on $V_2O_3(0001)/Au(111)$ for the -V (grey) and -V=O (black) terminations at normal emission. The difference of the low energy cutoff corresponds to the difference of the work function between the two terminations

being positioned in the incidence plane. The results are shown in fig. 6.2. For geometrical reasons only 29 different combinations of incident light and emission angles were available for measurement. The spectra were normalized to the background signal above E_F. No background has been removed. We have plotted in figure 6.3 only the spectra obtained for $\alpha = 60^{\circ}$ for the -V termination. V_2O_3 contains ten atoms per unit cell : four vanadium atoms and six oxygen atoms. The O 2p band therefore consists of eighteen sub-bands, as shows the band structure calculated by Mattheiss [79]. Our spectra do not exhibit sharp structures and thus a correct assignment of sub-bands is difficult. However, one may recognize four large features within the O 2p band. The lines in figure 6.3 symbolize these four sub-bands. They are supposed to illustrate in a rather qualitative than quantitative way the sub-bands energy changes with the detection angle, i.e. with the momentum of the photoelectrons. As we showed in section 3.2, the momentum of the photoelectron is related to the wave-vector of the photoelectron in the solid through the component parallel to the surface. The change in energy as function of $\overrightarrow{k}_{\parallel}$ is called dispersion. As we discussed in section 2.2, this is the result of delocalization of the electrons by formation of bands.

All spectra of figure 6.2 exhibit a decreasing of the emission intensity from the V 3d band and a narrowing of this band for the -V=O termination. A more accurate look at this emission band leads one to the conclusion that there is no spectral weight at the Fermi energy for the -V=O termination, i.e that a gap has opened in the surface region for the -V=O termination. The formation of vanadyl groups on the vanadium terminated surface therefore induces a metal to insulator transition. The narrowing of the V 3d band and the opening of a similar gap could be observed on single V_2O_3 crystals through the PM to AFI transition for pure V_2O_3 [87, 90, 50] or for Cr-doped V_2O_3 [54]. In order to study in detail these differences in the V 3d band between both terminations, we performed UPS measurements only in this energy region. Figure 6.4 shows the difference in the V 3d band between the spectrum for the -V termination and the one for the V=O termination. The spectra have been subtracted after having been normalized to the background above E_F. All difference spectra are drawn at the same (arbitrary) scale.
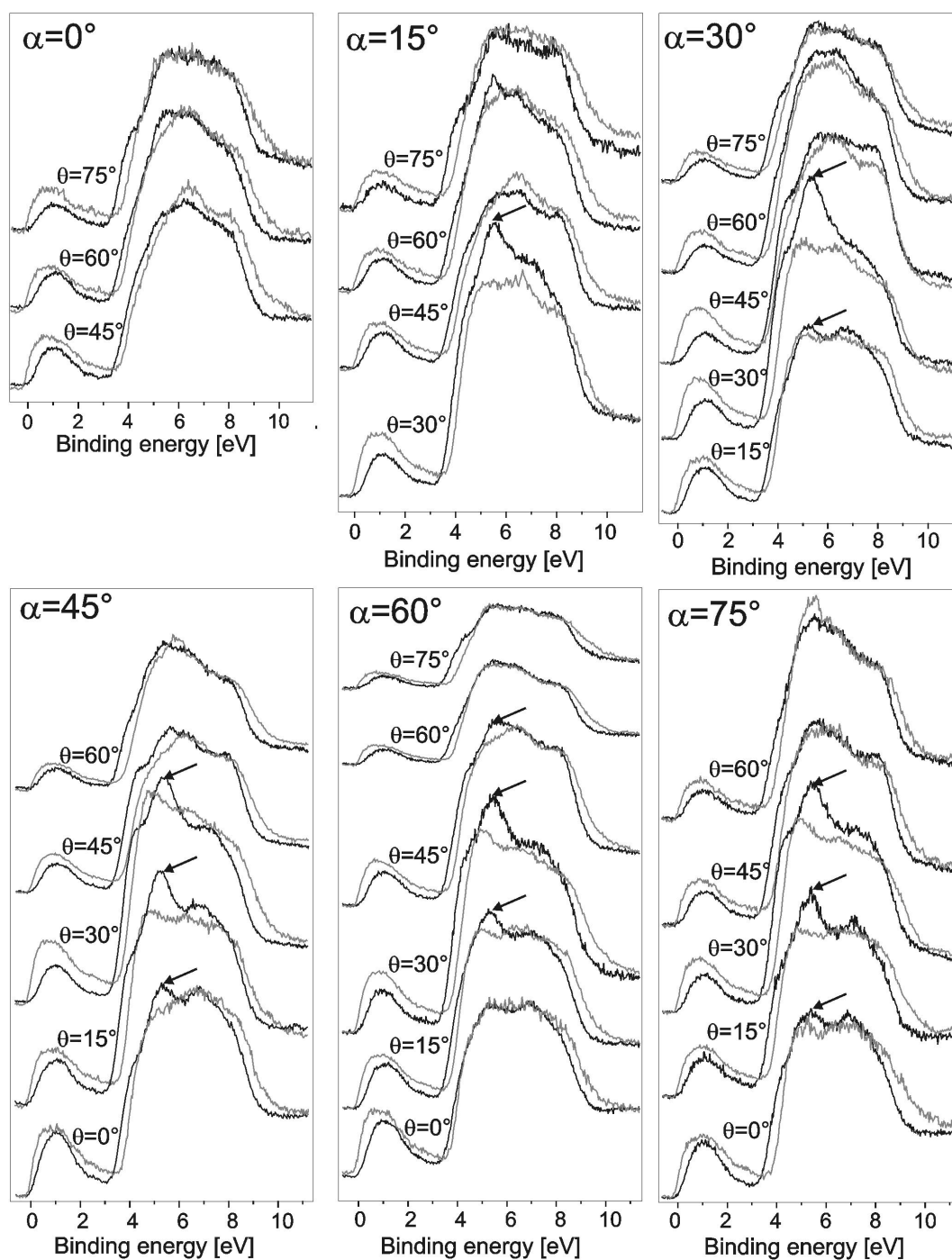
Figure 6.2: ARUPS on $V_2O_3(0001)/Au(111)$ for the -V (grey) and -V=O (black) terminations - α is the light angle of incidence and θ the angle of detection
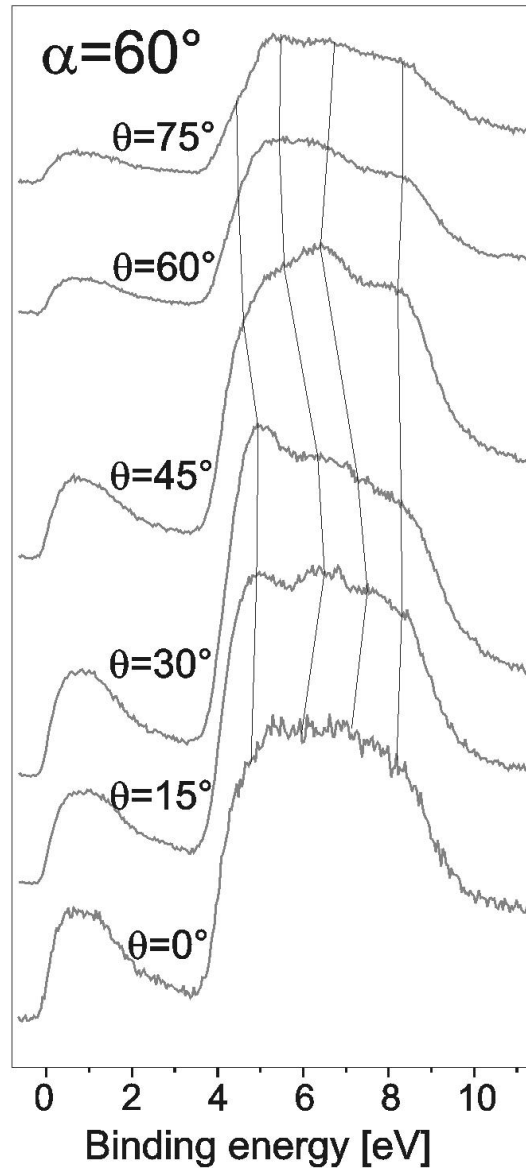
Figure 6.3: ARUPS on V-$V_2O_3(0001)$/Au(111) - α is the light angle of incidence and θ the angle of detection
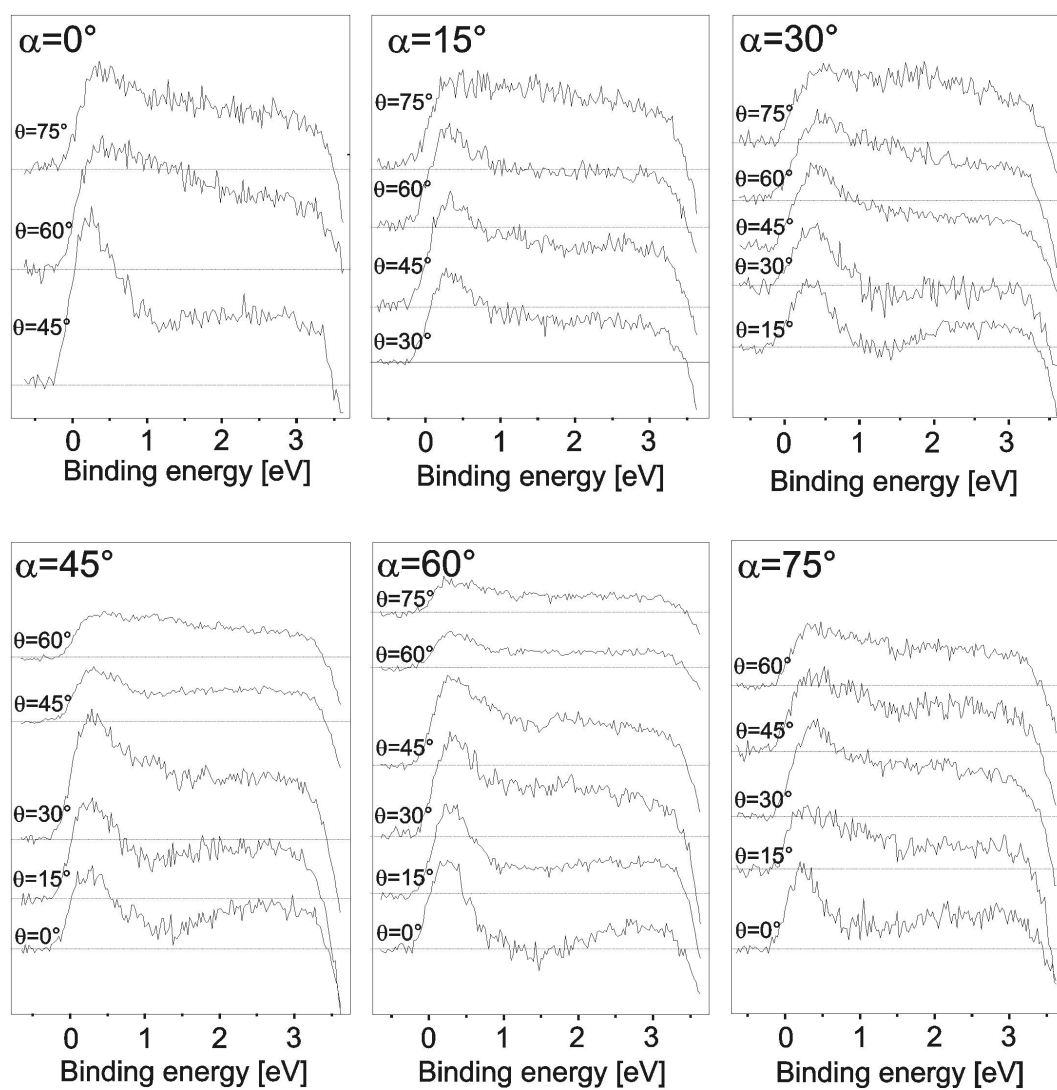
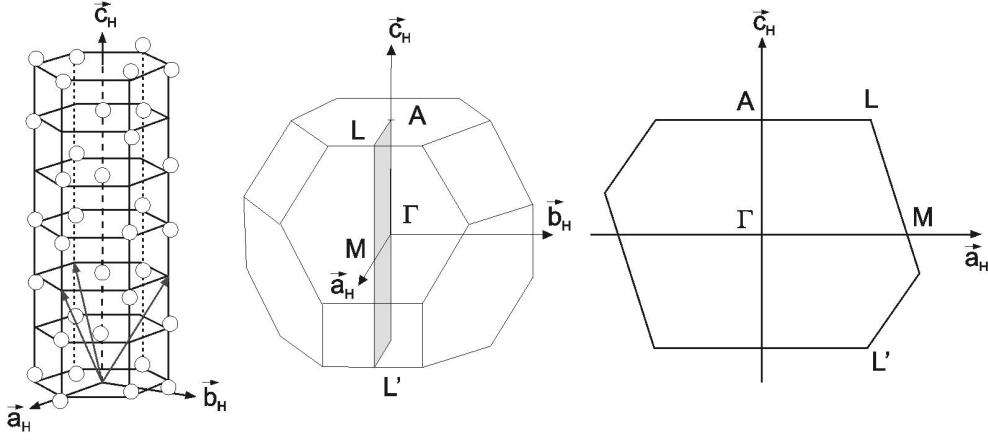Figure 6.4: Difference spectra in the V 3d region. (-V surface) minus (-V=O surface)

Figure 6.5: Vanadium atom positions (left) in V_2O_3 for the corundum phase. The primitive vectors of the primitive rhombohedral phase are shown. Corresponding Brillouin zone: three dimensional (middle) and in the plane (b_H, c_H) (right), corresponding to the incidence plane of the UPS measurement where c_H is the normal of the surface

They have all only positive values, showing that the loss of spectral weight in the V 3d band upon the formation of vanadyl groups is general. The most striking feature common to these spectra is a peak just below E_F. This peak shows a weak dispersion, as indicated on the figure. The other interesting feature is that for $\theta = 0$, the spectra are divided into two regions separated by a sort of gap. Actually, while the other spectra could be fitted with four Gaussians, they would be only by three. This becomes even more interesting when one looks at the band structure calculated by Mattheiss [79]. When $\theta = 0$, i.e. normal emission, the component of the momentum parallel to the surface is zero. We showed in section 3.2.1 that only the component parallel to the surface is conserved by the transmission of the photoelectron in the vacuum. In the case of normal emission, the photoelectron thus has the same direction as the wave-vector of the electron in the solid. This direction for $\theta = 0$ corresponds to the Γ-A direction in the first Brillouin zone, see figure 6.5. In the band-structure calculated by Mattheiss [79] there are only three occupied bands for the wave-vectors between Γ and A. This is consistent with our measurements, except for the broadness of the V 3d band which is

too small in the band-structure calculation (about 1 eV) compared to our results (about 2.5 eV). But the spectra we are talking about are difference spectra. Thus if they fit to the band-structure, the consequence is that one can interpret the difference between both terminations in terms of changes in the occupation of the bands but not in changes of the bands themselves. We will discuss this result in section 6.4 again.

For the -V=O termination, we also observe a shift of the O 2p band toward lower binding energy by 0.3 eV, as well as the appearance of additional spectral features in that region. In figure 6.6, we have plotted the O 2p band energy region of the spectra obtained for both terminations after having removed the shift between them and the difference spectra then obtained (-V=O termination minus -V termination ; the binding energy indicated is valid for the -V=O termination. For the -V termination, one should add 0.3 eV to the indicated values to obtain the correct binding energy). The difference spectra exhibit mostly one peak at about 5.5 eV which shows strong angular dependence. Interestingly, as figure 6.2 shows, this feature at 5.5 eV is most intense for $\theta = 30°$, independent of the angle of incidence of the light. There is another feature at about 7.5 eV which shows similar angular dependence but is less intense and broader. And finally, around 4.5 eV the difference spectra have negative values, corresponding to a loss of spectral weight at the top of the O 2p band for the -V=O termination. We will discuss these features and their angular dependence in section 6.4.

6.3   Core Level Spectra

The results for XPS measurements for the two surface terminations can be seen in figure 6.7. For the -V=O surface, two spectra are shown, the first was taken at normal emission, the other at an emission angle of 60°. The second one is therefore more surface sensitive. A fit of the spectra is shown in order to facilitate their interpretation. Here, we want to discuss the features observed besides the V $2p_{1/2}$, V $2p_{3/2}$ and O 1s lines (already discussed in chapter 5).

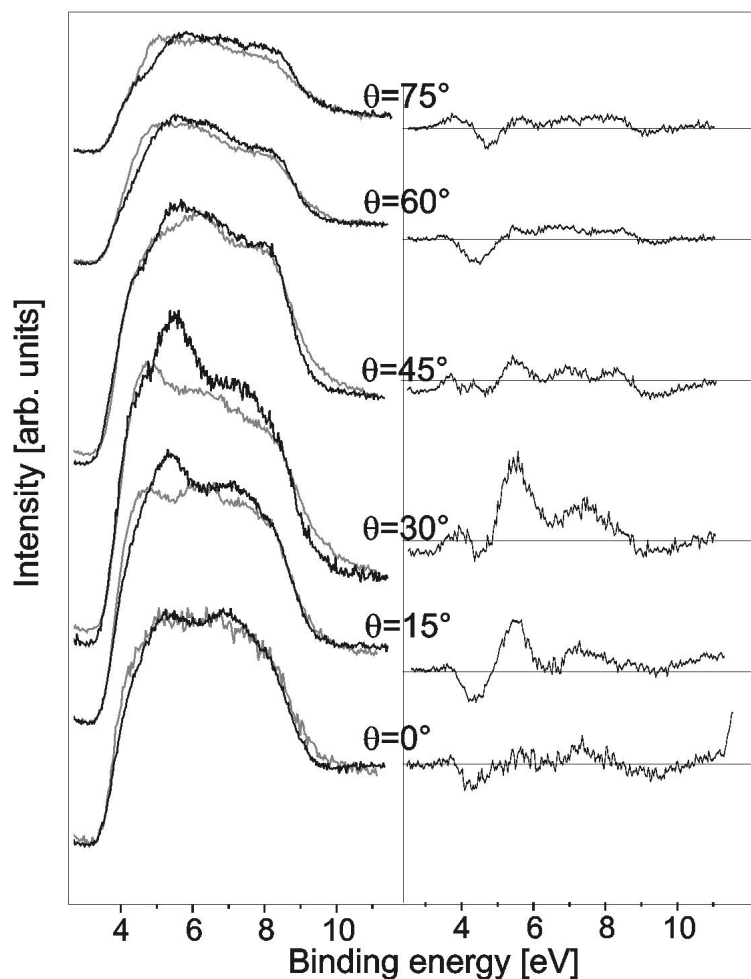The broader lines for V 2p in comparison to V_2O_5 [50, 92] correspond

Figure 6.6: Left: UPS (O 2p) of $V_2O_3(0001)$/Au(111) for the -V (grey) and -V=O (black) terminations for α (angle of light incidence) = 60°. The spectrum for the -V termination has been shifted by 0.3 eV towards lower binding energies. θ is the angle of detection. Right: corresponding difference spectra between both terminations
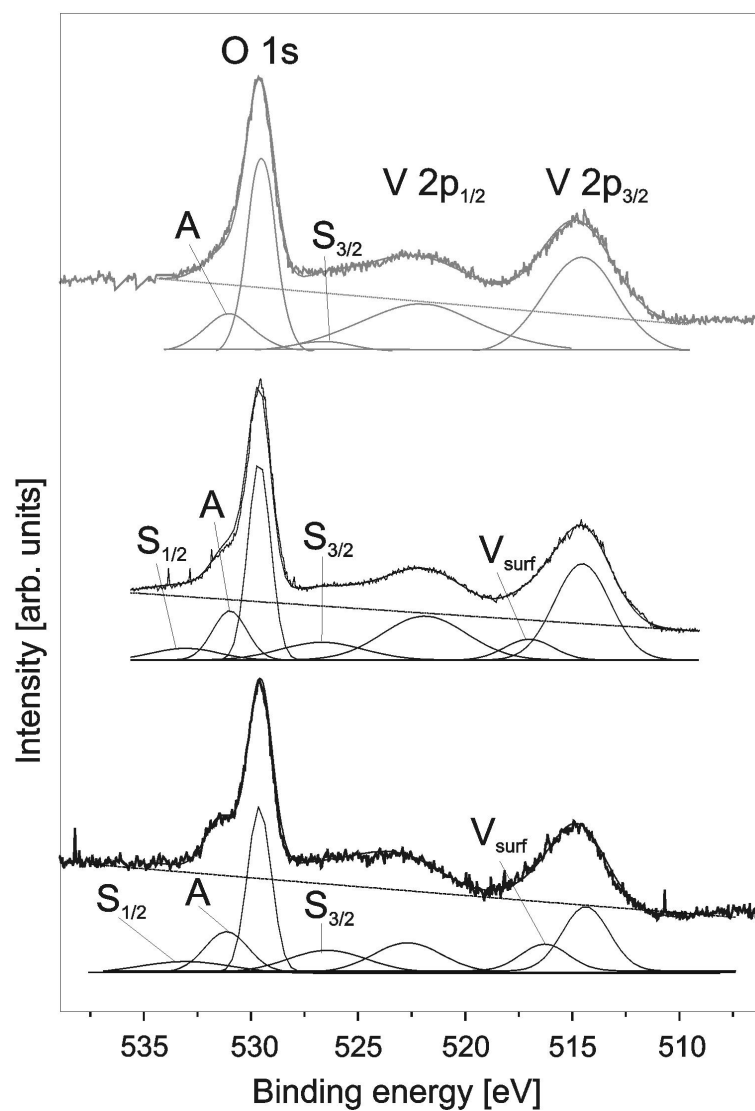
Figure 6.7: XPS of $V_2O_3(0001)/Au(111)$ for -V termination at normal emission (grey, top) and -V=O termination (black) at normal emission (middle) and at emission angle 60° (bottom)

to an intrinsic property of the material, interpreted as a characteristic of narrow-band metals [50]. The large asymmetry on the high binding energy side of the O 1s line is visualized on the fitted spectra by feature A. Henrich et al. [54] attributed this asymmetry to the creation of electron-hole pairs at E_F that reduces the energy of the emitted photoelectron (Doniach-Sunjic line shape). This interpretation was coherent with their experimental results since this asymmetry was not so strong for the insulating Cr-doped V_2O_3. Maurice et al. [93] found a second peak shifted by circa 2 eV with respect to the main O 1s peak for their oxide film formed on Cr(110). They assigned this peak to the presence of water in the film. We studied water adsorption on our V_2O_3 film with XPS also (see chapter 8) and found a peak for hydroxyl groups at a similar binding energy as feature A discussed here. Nevertheless, we do not think that feature A is due to water since it arises again from the -V surface after oxygen has been adsorbed and the sample annealed. We shall therefore assume that feature A corresponds to a Doniach-Sunjic line shape.

As the fits show, there are another features to be discussed : one in the vicinity of the V $2p_{1/2}$ line ($S_{3/2}$) and one at about 534 eV ($S_{1/2}$). These two features may be attributed to satellite structures of the V 2p main lines. Such features have been observed before and discussed for V_2O_3 [53, 55, 94] or for Fe_2O_3 [95]. They correspond to the charge-transfer satellites discussed in section 3.2.3. We have seen there that the satellite line corresponds to the $c^{-1}d^n$ configuration. Thus it can be attributed to poorly screened final states [96]. The increase of the intensity of the satellites in respect to the main line is therefore the result of a decrease of the screening. The intensity of the satellite features is larger for the -V=O surface than for the -V surface (feature $S_{1/2}$ is too weak for the -V surface to be resolved from feature A and thus does not appear in the fit for that surface). It is obvious that this difference is due to different surface properties as the intensity of the satellites is even larger in the spectrum taken at an emission angle of 60°. This is consistent with our UPS result which shows that the -V surface is metallic at room temperature and becomes an insulator when vanadyl groups form on it.
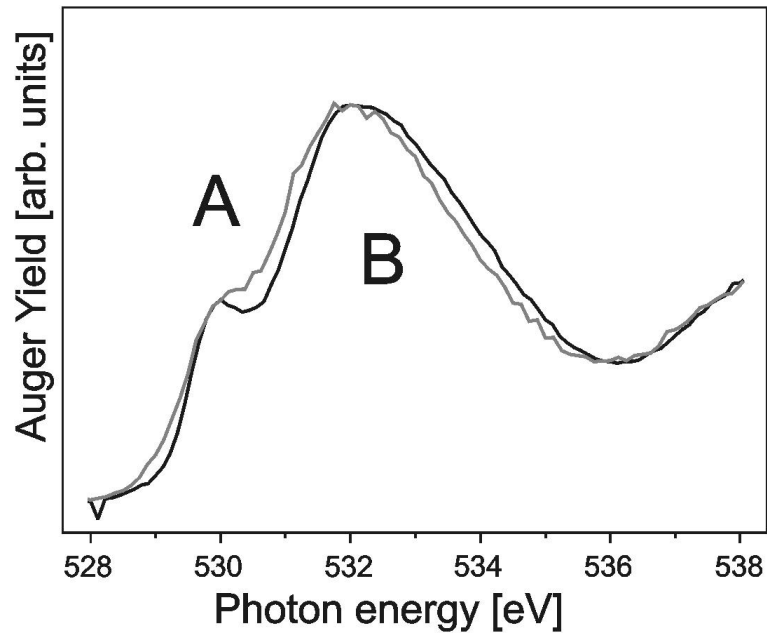
Figure 6.8: NEXAFS - O K-edge for $V_2O_3(0001)/Au(111)$ for -V (grey) and -V=O (black) surface terminations

Finally, while it is possible for the -V surface to fit the V $2p_{3/2}$ line with only one Gaussian this is not possible for the -V=O surface. The small second Gaussian for that surface (labelled as V_{red} in figure 6.7) can be interpreted as another oxidation state of V, namely V^{4+} or V^{5+}.

As we discussed in section 3.2.3 NEXAFS is a good tool to study the electronic structure and it allows one to get information about the unoccupied levels. We present here results for the V L-edge and O K-edge. In the V L-edge spectra, we consider the transition from the V $(2p^6 3d^2)$ initial state to a V $(2p^5 3d^3)$ final state. For the O K-edge spectra, the transition considered is from the O 1s level to an unoccupied level with oxygen p character, due to the selection rule stating that $\Delta L = \pm 1$. The signal obtained for this transition is a fingerprint of the hybridization of the O 2p with the metal states, leading to an oxygen 2p character for the unoccupied metal 3d, 4s and 4p states, see chapter 2. Figure 6.8 displays the result of a O K-edge NEXAFS measurement for the two surface terminations of $V_2O_3(0001)/Au(111)$. We observe two features labelled A and B. A is attributed to the transition to

the unoccupied V3d e_g^{Π} and a_{1g} states (t_{2g}) with O 2p character and B to the transition to the unoccupied V3d e_g^{σ} states (called e_g^{σ} because they are directed toward the oxygen 2p orbitals and so would form σ bond with them) hybridized with O 2p. The other half of the spectrum corresponding to the V 4s and 4p states hybridized with O 2p displays no change between the two terminations and is therefore not shown here. Taking the hybridization of the V t_{2g} and e_g^{σ} states with the O 2p into account, De Groot et al. [97] showed that the intensity ratio I_A/I_B should be equal to 1/4 for V_2O_3. This is in quite good agreement with our results.

The spectrum for the -V=O termination exhibits a shift towards higher energy for both A and B of about 0.25 eV relative to the spectrum for the -V termination. A similar shift has been observed by Müller et al. [98] when V_2O_3 becomes insulating but their spectra showed as well an increase of peak B that we did not observe. Abe et al. [99] observed by electron energy loss spectroscopy (EELS) a shift of 0.4 eV of the peak A through the transition from the PM to the AFI phase. They explained this increase of energy for that peak as a consequence of a splitting of the V 3d(t_{2g}) band. This band is partly filled in the PM phase and splits into a fully occupied band and an unoccupied band in the AFI phase. The unoccupied band would then lie on a higher energy level than in the PM phase. They also observed a decrease in intensity of peak A that they attributed to a decrease of the hybridization of O 2p with V 3d orbitals. We could not find any significative change in the intensity of feature A between both surfaces.

In figure 6.9, we show O K-edge spectra taken for the -V=O termination with different angles of incidence of light. The transition probability to a specific molecular orbital is maximum when the light vector $\overrightarrow{E}$ points in the direction of that molecular orbital and vanishes if $\overrightarrow{E}$ is perpendicular to the direction of the orbital [34]. Thus the angular dependence of the NEXAFS signal is a fingerprint of the anisotropy of the O 2p hybridization. We observe a linear dependence of the intensity for peak A with the angle of light incidence with respect to the surface normal. The intensity is maximum for grazing incidence i.e. for $\overrightarrow{E}$ nearly parallel to the c-axis. This result signifies that the hybridization of the O $2p_{c_H}$ orbitals with the V 3d e_g^{Π} and
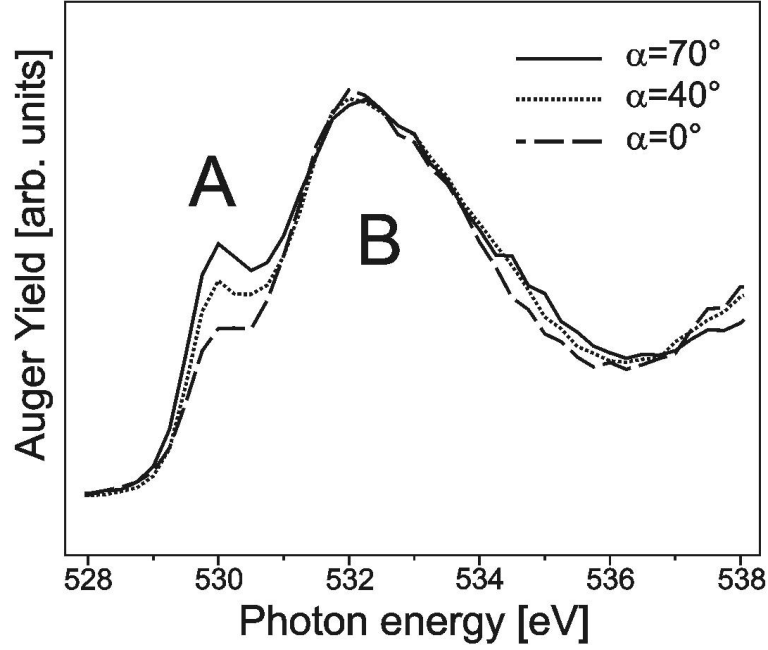
Figure 6.9: NEXAFS - O K-edge on O=V_2O_3(0001)/Au(111) as function of the angle α between incident light and surface normal

a_{1g} is stronger than the one of the O $2p_{a_H,b_H}$. Here $\{\overrightarrow{a_H}, \overrightarrow{b_H}, \overrightarrow{c_H}\}$ denote the primitive vectors in the hexagonal basis as shown in figure 6.5. Since the intensity of the peak B does not change with the angle of light incidence, the hybridization of the O 2p states with the V 3d e_g^σ is isotropic. Our results are in disagreement with those of Müller et al. [98]. For the insulating phase, they found a strong angular dependence of the X-ray absorption intensity showing that O $2p_{a_H,b_H}$ states have more contribution to the V 3d e_g^Π and a_{1g} bands than O $2p_{c_H}$. They interpreted this effect as a result of the increase of the c/a ratio in the insulating phase. Unfortunately, for technical reasons, we were not able to measure the angular dependence for the -V termination. Therefore, we cannot say whether this anisotropy for the hybridization we observed is only an effect of the -V=O termination or if the same anisotropy is present for the -V termination.

The angular dependence of the NEXAFS signal measured for the V 2p for O=V_2O_3(0001)/Au(111) can be seen on figure 6.10. The interpretation of the
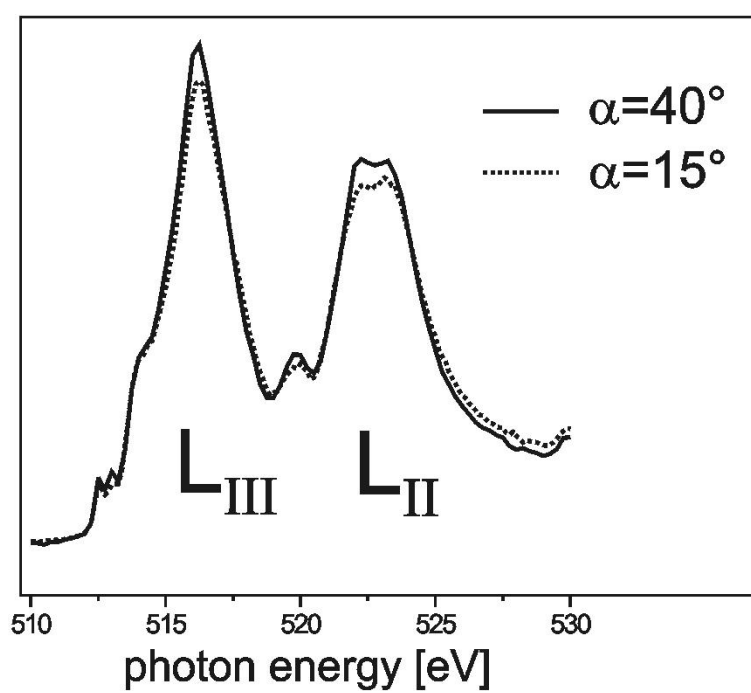
Figure 6.10: NEXAFS V 2p on O=V_2O_3(0001)/Au(111) as function of the angle α between incident light and surface normal

O K-edge spectra was relatively straightforward since the interaction effects between the hole left on oxygen and the unoccupied states on the metal sites could be neglected to a first approximation [97]. This is not the case for the V L-edge and the interpretation of the result obtained for the angular dependence cannot be so easily based simply on light polarization. Park et al. [78] reported polarization dependent X-ray absorption measurements on pure and Cr-doped V_2O_3 single crystals and compared the results with their theoretical calculations for pure $e_g^\Pi a_{1g}$ and pure $e_g^\Pi e_g^\Pi$ initial states. The authors concluded that the V $3d^2$ ions are in the high spin state (S=1) and that the ground state for all the phases considered cannot have neither pure $e_g^\Pi e_g^\Pi$ nor $e_g^\Pi a_{1g}$ symmetry but it has to be represented by a mixture of them. This theory is supported by an LDA+DMFT(QMC)(local density approximation with density mean-field theory using quantum Monte Carlo simulations) study carried out by Held et al. [100]. Our spectra show a similar trend as those of Park et al. but further calculations would have to be performed to further deduce information about the occupation of the V 3d orbitals.

6.4 Discussion on the Role of the Termination

In the previous sections of this chapter, we have seen that our photoemission results for the -V=O termination are very similar to those obtained on V_2O_3 below the transition temperature or on Cr-doped V_2O_3. The difference between both terminations is only the presence of supplementary oxygens in the case of the -V=O termination. In this section, we will firstly discuss the geometry and stability of this surface. Then, we will try to explain why the formation of these vanadyl groups leads to a such dramatic enhancement of the electron correlations that the surface becomes insulating.
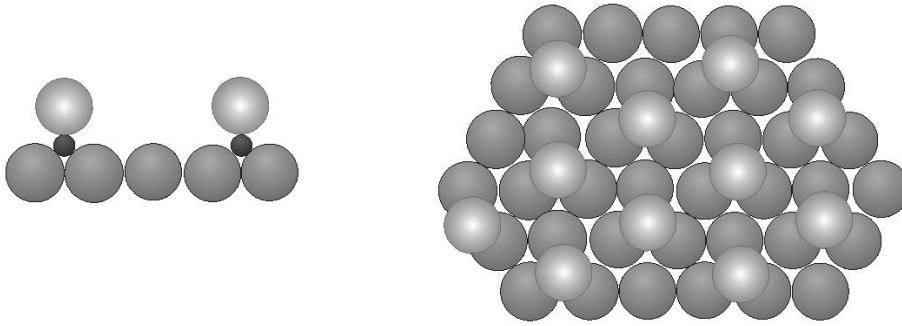
Figure 6.11: First model for the V_2O_3(0001) surface geometry. The oxygen atoms of the vanadyl groups sit on top of the vanadium atoms. Left: side view, right: top view

6.4.1   Surface Geometry

The first question that arises is how the -V=O terminated surface looks like in terms of geometric structure. The V_2O_3(0001) surface is a so-called polar surface. We mentioned in section 2.2.2 the problem posed by such surfaces because of the non-zero mean value of the electric field. A solution to cancel the electric field mean value is to reduce the surface charge density by a factor of two [10]. For the -V termination, this can easily be done by removing one of the two vanadium atoms for each unit cell, as it is the case for the Cr_2O_3(0001) face ([101] and references therein). The -V=O surface then can be imagined by solely adding a neutral oxygen atom to each surface vanadium atom. This has no influence on the electrostatic potential as long as the oxygen atoms remains neutral. This is the case for a pure covalent V=O bond. Note that the vanadyl molecule exhibits a highly covalent bond.

We start here from a picture with a neutral oxygen atom double bonded to the surface vanadium atoms. The most intuitive model because of the symmetry of the surface (C_{3v}) is to imagine the oxygen atoms on top of the vanadium atoms so that the V=O double bond is normal to the surface. This is schematically illustrated in figure 6.11. This scheme leaves the symmetry of the surface unchanged. The surface vanadium atoms would then sit in a distorted tetrahedron formed by the oxygen next neighbors while the bulk vanadium atoms are in a octahedron environment. It is not impossible to

have different oxygen environments for the vanadium sites. This occurs for instance in V_3O_7, see appendix A. We discussed shortly in chapter 2 the splitting of the V 3d orbitals due to the ligand field. In a tetrahedral environment, the 3d orbitals experience a similar splitting as in an octahedral ligand structure giving a set of 3 t_2 orbitals and 2 e orbitals. The strength of the splitting is then 4/9 of the value of the splitting for an octahedral environment [8]. The oxygen atom of the vanadyl forms a double bond with the vanadium atom. Thus one has to find two V 3d orbitals that have the right geometry to form a σ and a π bond with two O 2p orbitals, respectively. Due to the trigonal distortion of the corundum structure, the 3 t_{2g} orbitals split into one a_{1g} and two e_g^Π orbitals. The a_{1g} orbital is oriented along the c_H axis (normal to the surface) and so could form a σ bond with a O 2p orbital (say a $2p_{c_H}$ orbital -in order to avoid confusion we do not switch to a (x,y,z) basis but keep the vector basis (a_H, b_H, c_H) defined in the hexagonal system in figure 6.5). None of the remaining V 3d orbitals can form a π bond with an O 2p. Therefore, one has to imagine a hybridization scenario between several V orbitals to make the imagined geometrical arrangement possible. Such hybridizations are well known in molecular chemistry, mostly between s and p orbitals as in the methane molecule, but hybridizations between 3d, 4s and 4p orbitals are also possible in transition metals provided their energies are close to each other [102].

Imagine now that the vanadyl bonds have ionic contribution like the V-O bonds in the bulk. The surface charge density for the last oxygen layer is then equal to one third of its bulk value (one oxygen atom per surface unit cell instead of three), i.e. $-\sigma/3$ where σ is the absolute value of the charge density of the vanadium and oxygen layers in the bulk. In this model, however, we do not have a "standard" (partially) oxygen terminated surface. There is here a crucial difference because we start from a half-terminated -V surface and add neutral oxygen atoms which pull charge from the vanadium surface atoms. The charge density of the last vanadium layer then does not remain $\sigma/2$. It instead becomes $\sigma/2 + \sigma/3 = \frac{5}{3}\sigma/2$. Thus the charge of the vanadium ions has been multiplied by 5/3 and so it is now equal to 5 instead of 3. This is in agreement with the signal corresponding to the valence state
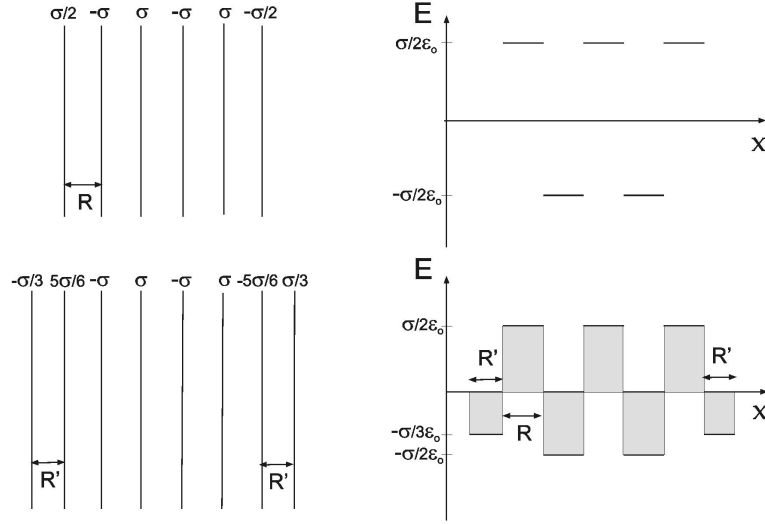
Figure 6.12: Electrostatic arguments for the models of the V-termination (top) and the -V=O termination (bottom). For the latter, the mean value of the electrostatic field E is cancelled for $R\sigma/2\epsilon_o = 2R'\sigma/3\epsilon_o$, i.e for R'=3/4 R

5+ found in the XP spectra of O=V_2O_3 (see figure 6.7 in 6.3). The V=O bonds therefore are here to be seen as an addition of dipole density as has been discussed in section 2.2.2. We have seen there that the macroscopic energy of the system will vanish if the added dipole density $\sigma'R'$ is equal to $\frac{\sigma R}{4}$. Figure 6.12 displays the electrostatic arguments used in the following. It should be emphasized here that we make in this model a great approximation by assuming that the V=O bonds have exactly the same character that the V-O bonds in the bulk in terms of hybridization. This yields $\sigma' = \sigma/3$ and thus R' has to be equal to $\frac{3}{4}R$ to satisfy the condition mentioned above for the macroscopic energy to vanish. The V=O bond length d is equal to 1.585 Å and so is much shorter than the V-O bond in the bulk ($\sim 1.97 - 2.05$ Å[79]). The inter-layer distance along the $\overrightarrow{c_H}$-axis is R = 1.165 Å when one neglects the V displacement along that direction [79]. In order to have $R' = \frac{3}{4}R$, the angle between the V=O bond and the surface normal must be $\gamma \sim 56^o$ ($\cos\gamma = R'/d$). This value found for γ corresponds to the angle between the surface normal (c_H) and the direction of the e_g^σ orbitals (x,y and z in a basis where the primitive axes correspond to the axes of the octahedron formed
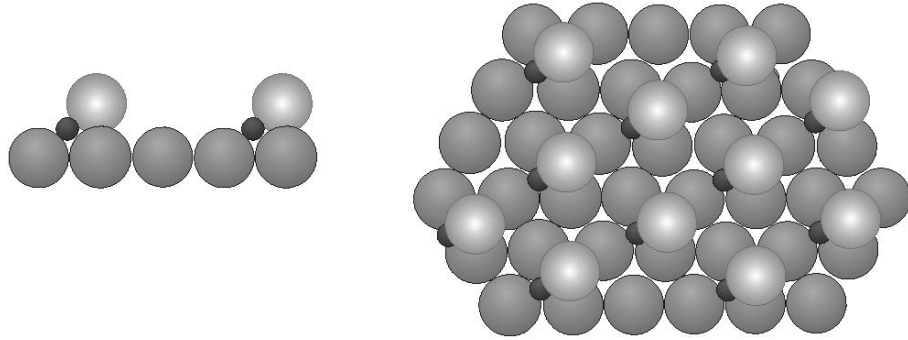
Figure 6.13: Second model for the $V_2O_3(0001)$ surface geometry. The oxygen atoms of the vanadyl groups occupy quasi regular bulk positions. Left: side view, right: top view

by the oxygens atoms around the vanadium central atom) - the exact value for the angle between the x,y or z axis and the surface normal for a regular octahedron is $\arccos(1/\sqrt{3}) \sim 55^o$. That is to say that in this model, the oxygen atoms of the vanadyl sit quasi on regular positions of bulk V_2O_3 (not exactly because the V=O bond length is shorter than the V-O bond in the bulk). This is schematically illustrated in figure 6.13. The orbitals involved in the double bond are then simply the V 3d e_g^{Π} and e_g^{σ} orbitals which form with O $2p_{x,y}$ and O $2p_z$ π and σ bonds, respectively. The symmetry of the surface is not C_{3v} anymore since only one oxygen bonds to each surface vanadium and not three. But if one supposes the existence of domains in which all the vanadyl groups are oriented along the same direction (as figure 6.13 shows), the surface unit cell is thus left unchanged and so is the LEED pattern.

In order to determine the geometry of the -V=O surface, one should take advantage of the ARUPS data shown in figure 6.2. There, we observed a new feature for the -V=O terminated surface that can be assigned to the vanadyl oxygens. This feature shows strong angular dependence. As discussed in chapter 3 (equation 3.26), the term determining the angular dependence of the signal intensity is $\langle \varphi_e(n)|H'|\varphi_k(n)\rangle$. Assuming a plane wave for the final state, it can be shown that this matrix element is proportional to: $(\overrightarrow{A}.\overrightarrow{p})e^{-\overrightarrow{p}.\overrightarrow{r}}\varphi_k(\overrightarrow{p})$ with $\varphi_k(p)$ the Fourier transform of the initial-state

wave function [103]. A theoretical treatment for each assumed geometrical structure of the surface allows one to determine the corresponding electronic structure and thus the initial-state wave functions for the vanadyl oxygen electrons. Using the proportionality property of the signal intensity discussed above, a comparison with the ARUPS data should be relatively straightforward and permit the determination of the right structure model.

6.4.2   Removal Process of the O of the Vanadyl Groups

As already mentioned in chapter 5, chromyl groups were observed on Cr_2O_3(0001)/Cr(110). To remove these chromyl groups and obtain the - Cr terminated surface, the sample was heated up to 1000 K [104]. In the case of V_2O_3 on both Au and W substrates, a desorption occurs for lower temperatures, e.g 600 K. We believe that the desorption of the oxygen of the vanadyl groups does not result solely from the thermal energy but is electron stimulated. As explained in chapter 4 we used electron bombardment for heating the sample. The major part of the electrons emitted by the tungsten filament reaches the sample on its back side but a few come onto the sample onto its front face. One can then imagine several scenarios for the electron stimulated desorption (ESD) process. The simplest and most general model is the so-called Menzel-Gomer-Redhead model (MGR). This model assumes an interaction of the system initially in a ground-state configuration with an incident electron which initiates a Frank-Condon (FC) transition to some excited state, possibly anti-bonding or ionic in nature [105]. The MGR model is schematically illustrated in figure 6.14. Quenching of the excitation will lead to recapture of the adsorbate, unless it has already acquired an amount of kinetic energy sufficient to result in desorption on the ground-state PE curve [106]. In this case, an incident electron merely stimulates an electronic excitation but in some cases there exists a possibility for the impinging electron to be captured for a finite time [105]. One could imagine in our case that an incoming electron stimulates a transition from the (bonding) π level of the V=O bond to the (anti-bonding) $\pi^\star$ level or to the (non-bonding) δ level and is then itself captured in one of these orbitals, resulting in desorption
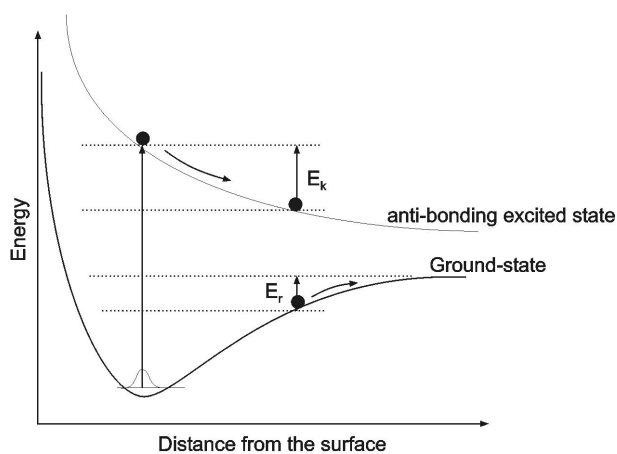
Figure 6.14: Schematic potential energy curves illustrating stimulated desorption by the Menzel-Gomer-Redhead model. For quenching occurring for kinetic energy E_k greater than the the barrier for recapture E_r the particle can escape, otherwise it results in recapture of the particle into the ground-state

of the oxygen atom from the surface. It is possible that the thermal energy supports the electron stimulated desorption giving the oxygen kinetic energy and thus facilitating the overcoming of the barrier (see figure 6.14).

6.4.3 Dramatic Change in the Electronic Structure of the Surface

Emission from the O 2p Band

The UPS difference spectra for the O 2p band between the -V termination and the -V=O termination show a loss of spectral weight at the top of O 2p band for the -V=O termination. This may be explained considering that the formation of the V=O bond at the surface pulls off electrons from the V 3d shells towards the O 2p of the vanadyl group. The oxygen of the underlying layer might try to compensate this loss of electrons on the surface vanadium atoms through an increased hybridization with them. This can be seen as sort of charge transfer from the oxygen atoms to the vanadium atoms, explaining this loss of spectral weight at the top of the O 2p band. This
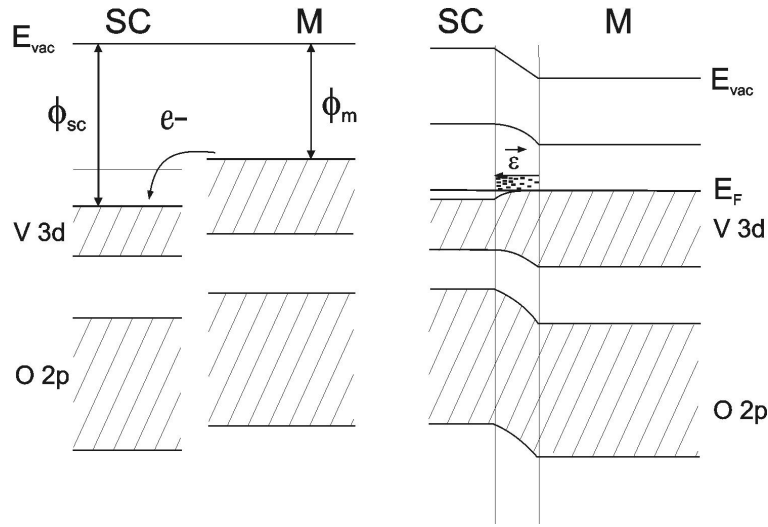
Figure 6.15: band-bending at a metal-semiconductor interface induced by the potential barrier due to the charge transfer between the metal and the semiconductor

would explain also the NEXAFS data which show for the -V=O termination a larger hybridization between O 2p and V t_{2g} (e_g^{Π} and a_{1g}) in the $\overrightarrow{c_H}$ direction (normal to the surface) than in the hexagonal basal plane.

The shift observed in the O 2p band between both terminations can be explained considering that only the surface is insulating and the bulk remains metallic. This can be modelled formally by a contact between a metal of work function ϕ_m and a semiconductor of work function ϕ_{sc}. As $\phi_{sc} > \phi_m$ (in our case), electrons will move from the metal to the semiconductor in order to align the chemical potentials. This induces an interfacial dipole potential which works against this charge transfer and an equilibrium is reached (the chemical potential is then the same in the whole material). This potential barrier bends the bands [10] and for our situation bends the band of the semiconductor toward higher energies (lower binding energies), see figure 6.15.

Metal to Insulator Transition

The most interesting and surprising effect is the metal to insulator transition induced by the formation of the V=O species. We have seen in section 6.1 that the PM to AFI transition in V_2O_3, though still controversial, is mainly explained within the Mott-Hubbard model. As already explained in section 2.2, this model describes the electron correlations through the Hubbard energy U and the bandwidth W. In a periodic system having an odd number of electrons per unit cell, electron-electron interaction causes the splitting of the d bands into occupied and unoccupied states, called lower and upper Hubbard bands. This system must be an insulator (Mott insulator) when these electron electron correlations, U, are greater than the band width W [107, 108]. This is the Mott insulator.

In the insulating phase, a gap has opened between a full 3d band (lower Hubbard band) and an empty 3d band (upper Hubbard band) as the shift observed in the O K-edge spectrum for the V=O termination shows. The UP difference spectra for the V 3d energy region presented in section 6.2 suggest that the loss of 3d electrons required for the V=O bonds did not induce any change in the band structure but only in the occupation of the bands. The O 2p band does not show any structural changes either but essentially only features assigned to the vanadyl species when one removes the shift observed. This is very surprising since the Fermi level should simply go deeper in the band for a metallic system if the occupation of the band decreases. But as a correlation gap opens while the 3d bands are partially depleted, the two effects on the position of the Fermi level could compensate, so that one finds the 3d levels for both terminations effectively on the same position relative to the Fermi level.

The Mott transition can be characterized in photoemission by a decrease of emission at the Fermi level. In the framework of the so-called dynamical mean-field theory (DMFT), this change in emission from the d band is believed to correspond to a transfer of spectral weight from the region near the Fermi level to the upper and lower Hubbard bands. The DMFT has been used to explain photoemission spectra of $3d^1$ compounds [109, 110, 111, 112].

These compounds show in the 3d emission region two features : the first one, just below E_F, is assigned to the coherent part of the single-particle spectral function, and the second one to its incoherent part (corresponding to the lower Hubbard band). The coherent part seems to correspond in this model to the density of states and is attributed to itinerant d-band states or quasi-particle excitations [110]. The changes in the emission from the V 3d band between both terminations reveal actually two effects : an opening of a correlation gap and a decrease of the electronic density in the V 3d band for the -V=O termination. Since the latter implies a decrease of the emission from the V 3d band, one may have some difficulty to interpret the former along the line of the DMFT, i.e. in terms of transfer of spectral weight.

The MIT that we observed when vanadyl groups form on the surface is a very surprising effect. In a first approximation, formation of vanadyl groups can be interpreted as a doping of holes. It has been observed on ternary compounds [110] and also theoretically shown [107] that doping a Mott insulator with carriers (holes or electrons) leads to a transfer of spectral weight to the Fermi level. Formation of vanadyl groups should therefore favor the metallic phase and not induce a MIT, as we experimentally observed.

One could invoke orbital ordering, i.e a pure $e_g^{\Pi}e_g^{\Pi}$ ground state, to have a half-filled e_g^{Π} band. This could be a good starting point for a Mott insulator. In several theories about the insulating phase of V_2O_3 at low temperatures, it is assumed that the a_{1g} orbitals form a molecular bond between a V-V vertical pair and thus only the remaining e_g^{Π} electron is considered in the Hubbard model [108]. Nevertheless, this hypothesis cannot be retained for the surface since the vanadium atoms of the surface and half of them of the under-lying layer miss the other vanadium atom of the vertical pair. However, the explanation exposed here is only a speculative attempt to understand the observed phenomenon. Theoretical calculations should be performed to understand it properly. Note that electron correlation remains substantial even in the metallic phase of V_2O_3 [13], which is consistent with our XPS data where charge transfer satellites are important even for the -V termination.

Chapter 7

Phonons of $V_2O_3(0001)$

HREELS measurements were performed on the clean $V_2O_3(0001)/W(110)$ surface. All the spectra presented here were recorded in specular geometry ($a_i=a_r=65°$) with a primary energy of 5 eV and a full width at half maximum (FWHM) varying between 3.2 and 3.6 meV.

An analogy can be drawn with other corundum oxides since the major parameter governing the phonon features is the lattice structure. Infrared lattice vibrations have already been studied for V_2O_3 [113] and for other corundum systems, e.g. mostly for $\alpha - Al_2O_3$ [114, 115, 116] but also for Cr_2O_3 [117, 118, 119], for Ti_2O_3 [120] and for $\alpha - Fe_2O_3$ [121]. As discussed there, a group theoretical analysis predicts six infrared-active long-wave-length modes in addition to the seven Raman-active modes, $2A_{1g}+5E_g$: two A_{2u} modes with polarization parallel to the crystalline c_H axis and four E_u modes with polarization perpendicular to the c_H axis. HREEL spectra are dominated by the surface optical (SO) phonons or "Fuchs-Kliewer" modes, which we discussed in section 2.3. These modes have frequencies slightly lower than those of the bulk longitudinal optical (LO) phonons. Therefore, one can take for comparison the values found for the bulk LO modes in the infrared experiments. Table 7.1 summarizes the results found in the literature.

Figure 7.1 displays a spectrum of $V_2O_3(0001)/W(110)$ for the -V termination. A HREEL spectrum of $Cr_2O_3(0001)/Cr(110)$ (-Cr termination) is also shown for direct comparison. We firstly compare the features of our
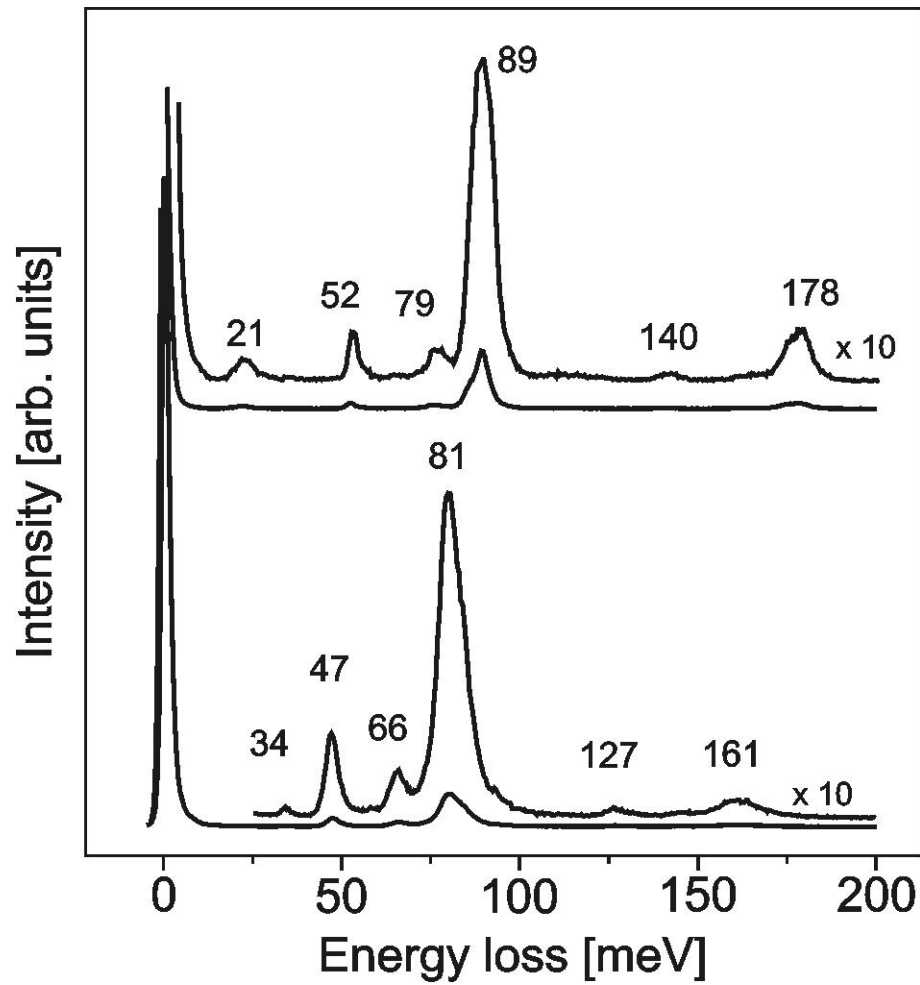
Figure 7.1: HREELS of Cr_2O_3(0001)/Cr(110) from [101] (top) and V-V_2O_3(0001)/W(110) (bottom)

$\overrightarrow{E} \perp \overrightarrow{c}$	Al_2O_3	Ti_2O_3	Cr_2O_3	Fe_2O_3
	48.2	34.9	38	28.6
	59.6	48.5	54.9	45.7
	77.6	62.3	73.6	61.3
	111.7	66.7	91.1	82.2
$\overrightarrow{E} \parallel \overrightarrow{c}$	63.6	43.6	51.8	51.4
	108.1	68.5	90.1	82.2

Table 7.1: Comparison of the frequencies in meV of the LO modes of different oxides with corundum structure [120, 121]

spectrum with other spectra performed on V_2O_3 reported in the literature. Botto et al. [113] performed IR measurements on V_2O_3 obtained from V_2O_5 by temperature reduction treatment. They found peaks for energies that correspond to the losses at 47, 66 and 81 meV we observed. They did not find any feature at 127 meV but at 121 meV. They assigned this shifting of the peak relative to the position found for the vanadyl in V_2O_5 (127 meV) to increased weakness of the surface V=O bonds and to decreased oxidation states at the surface. Guo et al. [122] performed HREELS measurements on $V_2O_3(0001)/Al_2O_3$ and found only four of the six features we observed. We suppose they could not see the two less intense features at 34 and 66 meV because of a too large FWHM of the elastic peak. We encountered the problem and then indeed saw only the four most intense features.

The comparison with an HREEL spectrum of $Cr_2O_3(0001)/Cr(110)$ shows a very similar spectrum structure whereas the phonon frequencies of Cr_2O_3 are larger than those of V_2O_3. It is tempting to interpret this frequency shift between both oxides in terms of oxygen-metal bond strength. The phonon frequencies can always be expressed in the form:

$$\omega^2 = k/\overline{m} \tag{7.1}$$

where k is an effective force constant and $\overline{m}$ is an oscillator mass. The most intense phonon at 81 meV (89 meV for Cr_2O_3) corresponds to a phonon mode in which the metal and the oxygen ions move in opposite directions along the c_H axis. For these modes $\overline{m}^{-1} = 2\overline{m}_{V/Cr}^{-1} + 3\overline{m}_O^{-1}$. This yields $\overline{m}_{V_2O_3}^{-1} > \overline{m}_{Cr_2O_3}^{-1}$

and therefore $k_{V_2O_3} < k_{Cr_2O_3}$ as $\omega_{V_2O_3} < \omega_{Cr_2O_3}$. One can therefore conclude that the metal-oxygen bond in V$_2$O$_3$ is not as strong as in Cr$_2$O$_3$ along the c_H axis. One shall remember here that V$_2$O$_3$ has a larger c/a ratio than Cr$_2$O$_3$ which could explain a difference in bond strength. Moreover, the number of 3d electrons may play an important role. It is difficult, however, to relate the relative values of k to any microscopic parameters because they contain contributions from both short-range bonding forces and longer-range Coulomb and dipole-dipole interactions [120].

As explained in section 3.3.2, the dipole scattering selection rules predict a stronger interaction of the incoming electrons with vibrational modes normal to the surface, i.e. in our case parallel to the c_H axis. We can therefore assign the two most intense features at 47 and 81 meV to the two A$_{2u}$ modes. Successive loss events can occur during an HREELS experiments, resulting in multiple loss peaks. Their intensities are given by the Poisson distribution:

$$P_n = \frac{e^{-x}x^n}{n!} \tag{7.2}$$

where x is the predicted single-phonon loss probability and P_n gives the probability of an n-phonon excitation in the full spectrum [6]. The two features at 127 and 161 meV can be assigned to multiple loss ($127 \simeq 47 + 81$ and $161 \simeq 2 \times 81$). The last two features at 34 and 66 meV correspond to the E$_u$ mode as maybe another feature at 85 meV which appears as shoulder on the right side of the feature at 81 meV. The feature at 21 meV for Cr$_2$O$_3$ is attributed to a microscopic surface mode as it disappears when molecules are adsorbed on the surface [101]. Upon adsorption of gas molecules on the surface, we observed no decrease of the feature at 34 meV. The very small intensity suggests that it corresponds to a E$_u$ mode. Because of the aforementioned frequency shift between V$_2$O$_3$ and Cr$_2$O$_3$ phonons features, we shall assign our feature at 34 meV to the feature at 38 meV found for Cr$_2$O$_3$ in [119].

In figure 7.2, we present HREELS spectra of V$_2$O$_3$(0001)/W(110) for both -V=O and -V terminations. The spectra differ only in the intensity of their phonons and in a loss at 127 meV corresponding to the vanadyl groups (V=O) as already discussed. The -V termination does show a loss at this energy
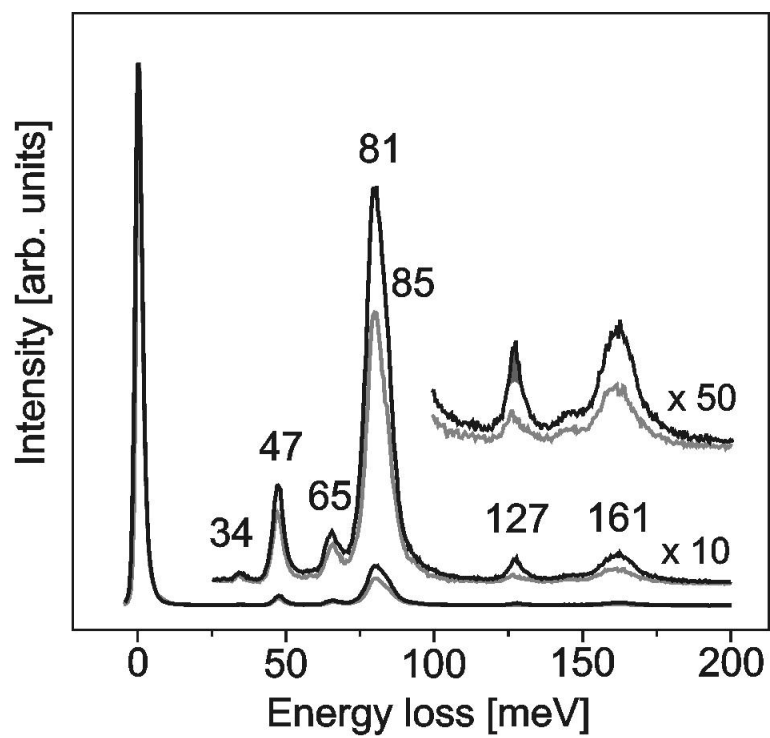
Figure 7.2: HREELS of $V_2O_3(0001)/W(110)$ for the -V=O (black) and -V (grey) terminations

because it corresponds accidentally to a multiple loss as discussed above. But only the -V=O termination exhibits at 127 meV this sharp feature colored in dark grey on figure 7.2. The overall difference of intensity of the phonons between both terminations can be explained in terms of electron mobility. The screening effect of electronic carriers reduces the amplitude of optical phonon excitations compared to insulators [6], and thus the phonons are more intense for the (insulator) -V=O termination than for the (metallic) -V termination. Nevertheless, we are not aware of morphology changes of the film surface by the removal process of the vanadyl groups. Morphology differences could explain the observed phonon intensity differences between both terminations.

Chapter 8

Water Adsorption

8.1 Introduction

Figure 8.1 displays the molecular orbital diagram for the H_2O molecule. The three highest occupied molecular orbitals detectable by UPS are the $1b_1$, $3a_1$ and $1b_2$ orbitals. Figure 8.2 shows the photoelectron spectrum obtained for H_2O in the gas phase. One obtains for ionization energies in the gas phase: 12.6 ($1b_1$), 14.7 ($3a_1$) and 18.5 ($1b_2$) eV [123].

The purpose of this chapter is to understand how water adsorbs on the $V_2O_3(0001)$ surface. As we have seen it is possible to prepare two terminations of $V_2O_3(0001)$ and therefore the adsorption experiments were performed on both -V=O and -V terminations. Figure 8.3 shows an HREEL spectrum of clean $O=V_2O_3(0001)/W(110)$ and with a multilayer ice on it, taken at 90 K for an energy loss region 100-300 meV (left) and 350-500 meV (right). A small features arises on the left side of a multiple phonon (at 204 meV - 1643 cm^{-1}) upon water adsorption. This feature can be associated with the $\delta(HOH)$ mode of ice and has already been observed on other corundum oxides [101, 124, 125]. For the second energy region in the curve on the right two small features are to be seen: a very broad one around 424 meV (3415 cm^{-1}) and one at 455 meV (3665 cm^{-1}). The first corresponds to a $\nu(OHO)$ mode of ice and the latter is due to dangling HO-H bonds at the ice-vacuum interface [124].
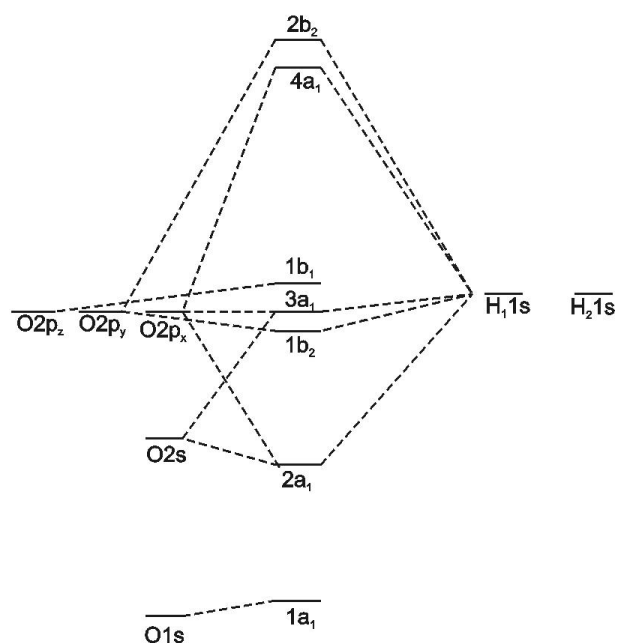
Figure 8.1: Molecular orbital diagram for the H_2O molecule
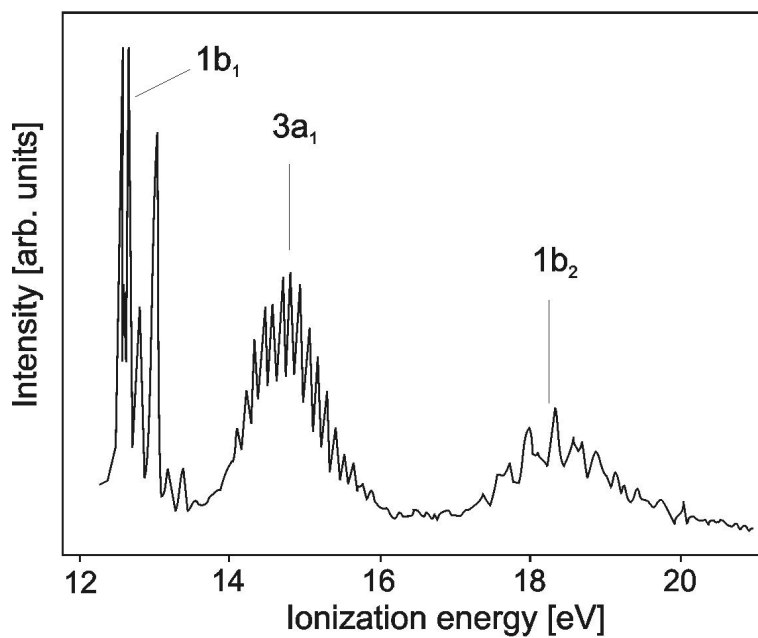
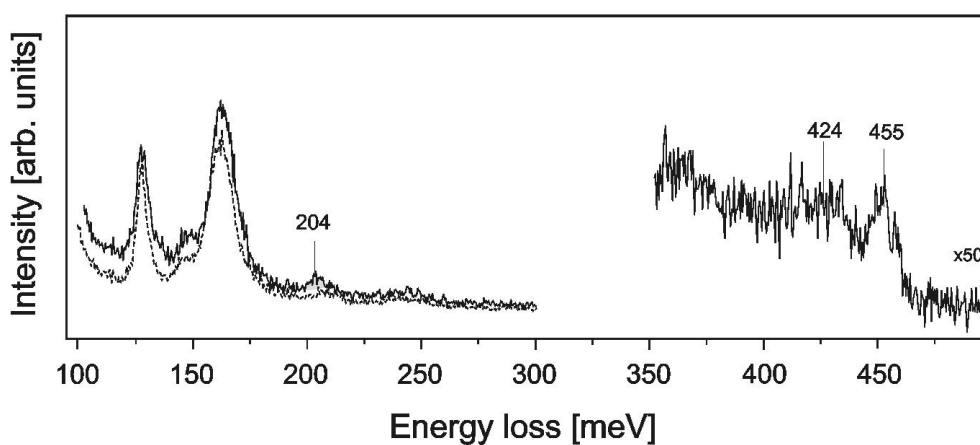Figure 8.2: Photoelectron spectrum of H_2O in the gas phase (from [123])

Figure 8.3: Clean O=V$_2$O$_3$(0001)/W(110) (dashed) and H$_2$O/O=V$_2$O$_3$(0001)/W(110) (solid) at 90 K. A feature appears upon water adsorption at 204 meV

The next step of the water adsorption experiment is to heat the sample in order to desorb any multilayer water leaving a nearly saturated monolayer. The way water bonds to the surface was then studied with UPS, XPS and HREELS. The different parameters governing the way water adsorbs on a surface are quite complex. We could observe both H$_2$O chemisorption and dissociative adsorption -with formation of OH groups- for both terminations. We shall first present the results obtained for each case and in the last section discuss how to model the adsorption properties we observed.

8.2 H$_2$O Chemisorption

Figure 8.4 shows the UPS results for 0.1 L water adsorption on the **-V termi-nated** V$_2$O$_3$(0001)/Au(111) taken at normal emission. The sample surface was exposed to water at 90 K and the spectrum was taken at 165 K. The spectrum for the clean surface is shown for comparison. On the bottom of the figure the difference spectrum obtained by subtracting the clean sur-face spectrum from the spectrum taken after water adsorption is displayed. The subtracting procedure was made without energy correction since the observed shift in energy of the O 2p band is negligible. Three features at
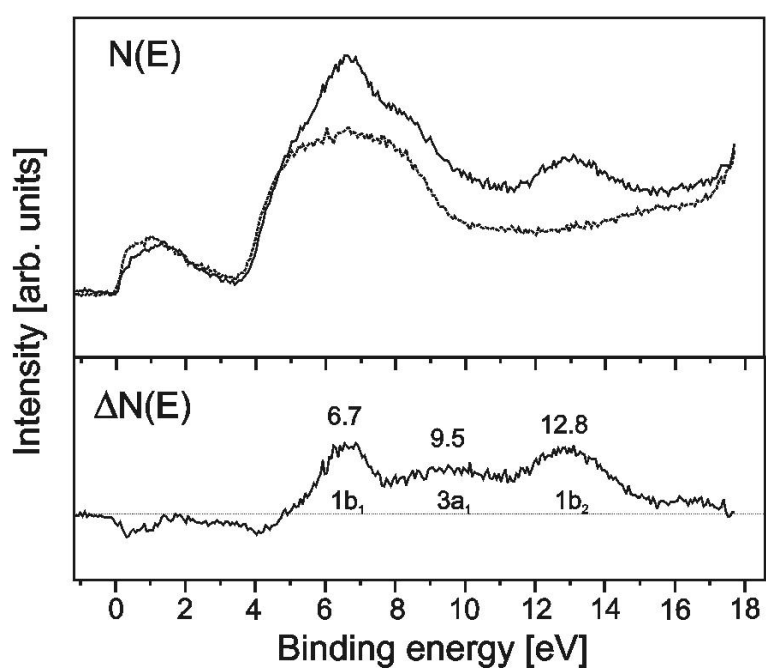
Figure 8.4: Top: clean -V terminated $V_2O_3(0001)/Au(111)$ surface (dashed curve) and with 0.1 L H_2O (solid curve) at 165 K. Bottom: difference spectrum
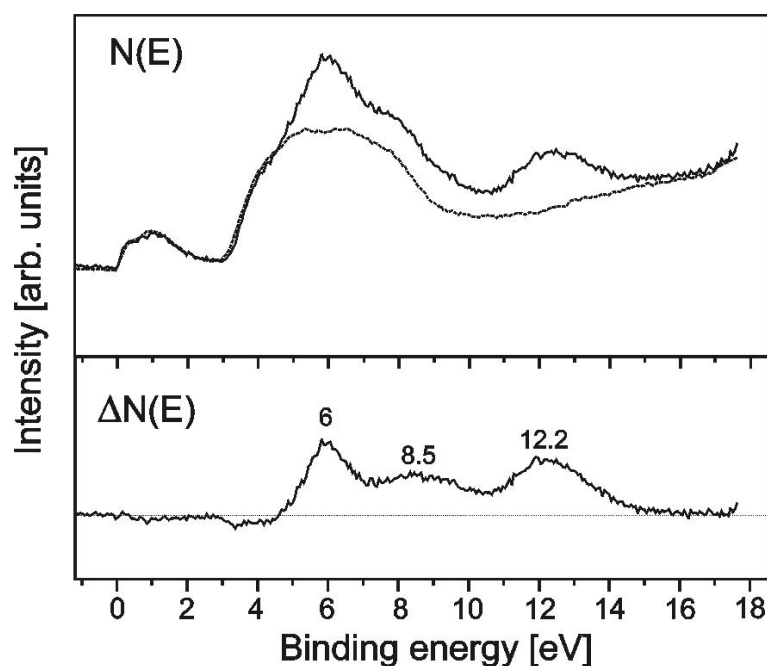
Figure 8.5: Top: clean O=V_2O_3(0001)/Au(111) surface (dashed curve) and with 0.1 L H_2O (solid curve) at 165 K. Bottom: difference spectrum

6.7, 9.5 and 12.9 eV are to be seen and constitute the typical signature of molecular water. A comparison with the photoelectron spectrum of H_2O_{gas} shown in figure 8.2 yield a shift of the water orbitals (the extra-molecular relaxation-polarization -EMRP- shift) of 5.9 ($1b_1$), 5.3 ($3a_1$) and 5.7 ($1b_2$) eV. These three values are very close together, indicating that adsorbed H_2O does not interact strongly with the substrate. Two small negative features are observed in the difference spectrum of figure 8.4. One between the Fermi level and 1 eV, and a second at about 4 eV.

Figure 8.5 shows the UPS results for 0.1 L water adsorption on the **-V=O terminated** V_2O_3(0001)/Au(111) taken at normal emission. As for the -V termination, the sample surface was exposed to water at 90 K and the spectrum was taken at 165 K. Three features at 6, 8.5 and 12.2 eV, analogous to those found for the -V surface, are observed in the difference spectrum in the bottom of the figure. They can be assigned to the H_2O $1b_1$, $3a_1$ and $1b_2$ orbitals, respectively. The values of the EMRP shift for the three orbitals

are very close together and no real bonding shift is observed, again indicating that the water molecule interacts only weakly with the surface. For the -V=O terminated surface, only a small negative feature around 4 eV in the difference spectrum is observed but no one just below the Fermi level.

Toledano et al. [126] performed water adsorption experiments on a $V_2O_3(0001)$ single crystal. Their difference spectra exhibit three positive features at 6.3, 9.6 and 12.3 eV binding energy, a negative feature at about 4.1 eV and smaller negative features at 0.2 and 1.0 eV. Their results are therefore very similar to those we found for the -V surface. A slight charge transfer for their surface and for our -V surface occurs from the substrate to the adsorbate. This explains the small negative feature just below the Fermi level. Toledano et al. assigned the negative feature at about 4 eV to additional charge transfer to the adsorbate or to a slight increase in the binding energy of substrate orbitals due to the presence of the adsorbate [126].

It is very interesting to notice that the spectra obtained for both terminations are actually very similar. The most striking difference is a shift of 0.7 eV between the features corresponding to the water orbitals. This shift corresponds to a difference in the EMRP shifts for the two surfaces. We have seen in section 3.2.4 that this EMRP shift may be expressed as $E_{relax} + E_{bond\ shift} - (\varphi + \Delta\varphi)$ [27]. The difference in the shift we observe then simply corresponds to the difference of work function φ between the two surfaces as discussed in section 3.2.2.

To summarize, the results presented in this section show that for low exposures, water adsorbs molecularly on both surfaces. The -V=O surface does not seem to interact strongly with the water molecule and no charge transfer is observed. A small charge transfer from the substrate to the adsorbate might occur in the case of the -V surface. The vanadium cation then acts for the -V surface as a Lewis base (electron donor). This is in disagreement with the most common situation where the bonding of water to a surface is accompanied by a net charge transfer to the surface [127].

8.3   Dissociative Adsorption

Figure 8.6 shows UP spectra obtained after 10 L water adsorption on the
-V=O terminated $V_2O_3(0001)$ and taken at normal emission. The sample
was exposed to water at 90 K and then heated to 190 K, 350 K and 550 K as
indicated on the figure. The spectrum of the clean surface is shown for com-
parison. The most striking result upon water adsorption is the appearance
of two large features at roughly 7.6 and 11.2 eV. The spectrum also exhibits
a dramatic shift (of about 2.5 eV) of the O 2p band towards larger binding
energies and an increase of the V 3d emission. The spectrum after heating
at 550 K shows no presence of adsorbates anymore but is not identical to the
clean surface: it corresponds to the spectrum of a -V terminated surface.

A glance at the spectrum of solid sodium hydroxide allows one to assign
the features at about 7.6 and 11.2 eV in the UP spectra to the 1π and 3σ
orbitals of OH^-, respectively. Kurtz et al. [56] found similar features at 7.4
and 10.7 eV for water on $V_2O_3(10\bar{1}2)$.

Figure 8.7 shows the UPS results of the same experiment but for the
-V terminated surface. Three large features arise upon water adsorption
at 7.7, 11.1 and 13.7 eV. At variance with the -V=O terminated surface,
the emission of the V 3d decreases here upon water adsorption. The O 2p
band shows a similar shift (~ 2 eV) as in the case of the -V=O terminated
surface. The features at 7.7 and 11.1 eV can be assigned to OH-groups while
the feature at 13.7 eV indicates that molecular water is still present on the
surface.

A HREEL spectrum taken after water has been adsorbed on the **-V=O
terminated** $V_2O_3(0001)/W(110)$ and the sample heated to 190 K is dis-
played in figure 8.8. Unlike the spectrum shown in figure 8.3 the spectrum
here shows only one feature at 453 meV besides the phonons of the substrate.
This feature is reflective of an OH stretching mode of an isolated OH group
- the term "isolated" shall denote an OH group whose proton is not involved
in hydrogen-bonding [125].

Figure 8.9 shows the O 1s XPS results obtained at 90 K after 3L water ad-
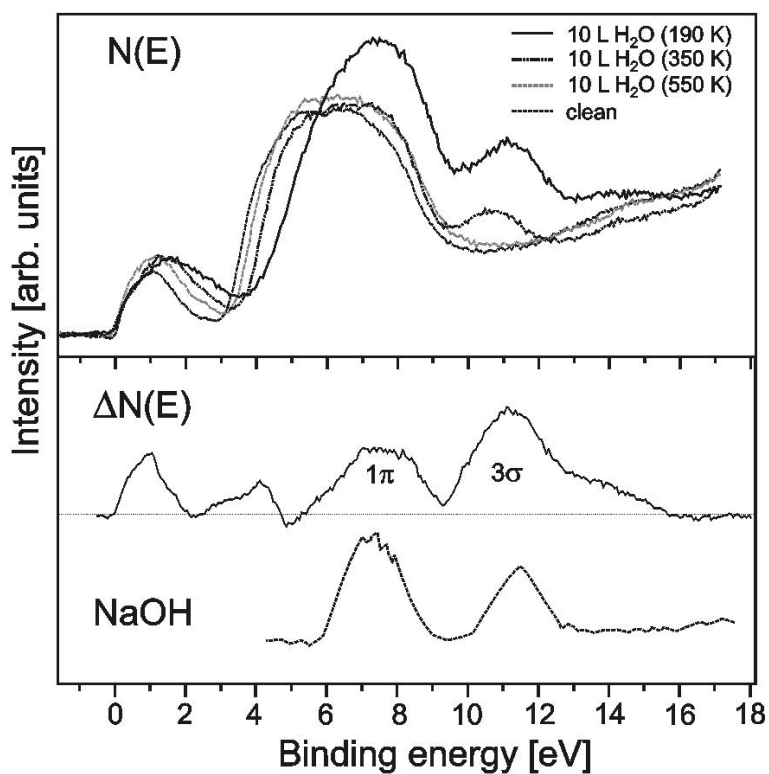sorption on the **-V=O terminated** $V_2O_3(0001)/Au(111)$ and after heating

Figure 8.6: Top: clean O=V$_2$O$_3$(0001)/Au(111) surface and with 10 L H$_2$O at 190 K, 350 K and 550 K. Bottom: difference spectrum between the H$_2$O adsorbed surface at 190 K and the clean surface (prior to the subtraction the upper edge of the O 2p band of the clean surface spectrum has been aligned with that of the H$_2$O dosed surface and spectrum of solid sodium hydroxide (dashed curve) shifted by approximately 1 eV towards smaller binding energies
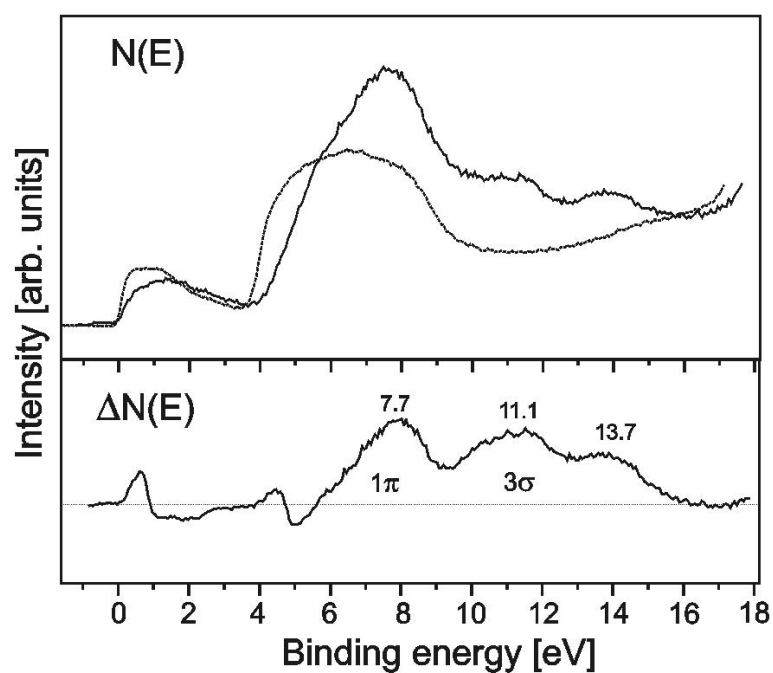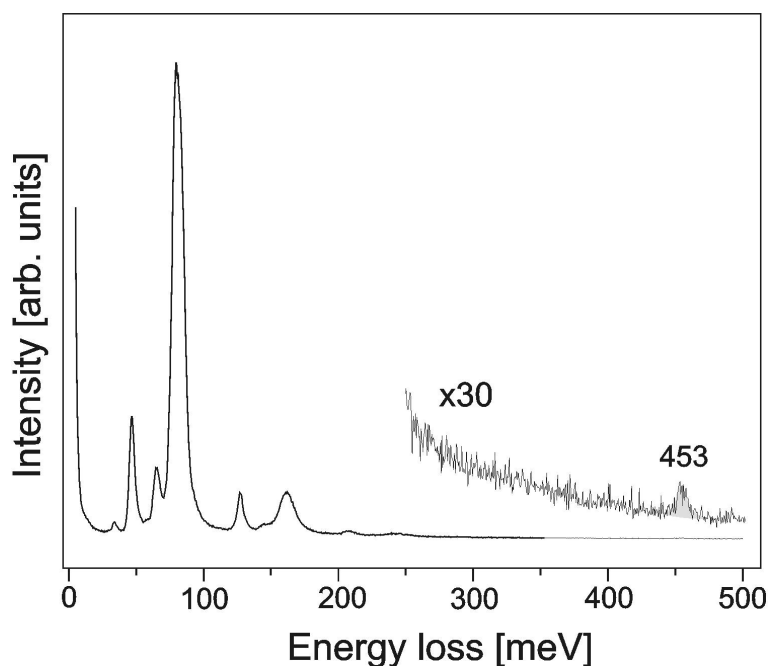
Figure 8.7: Top: clean -V terminated $V_2O_3(0001)/Au(111)$ surface (dashed curve) and with 10 L H_2O (solid curve) at 190 K. Bottom: difference spectrum. Prior to the subtraction the upper edge of the O 2p band of the clean surface spectrum has been aligned with that of the H_2O dosed surface

Figure 8.8: HREEL spectrum of 3L $H_2O/O{=}V_2O_3(0001)/W(110)$ at 190 K

the sample up to 220K and 300K as indicated on the figure. The spectrum of the clean surface is shown also. The spectrum taken at 90K after adsorption shows an additional feature at 533.5 eV besides the peak at 531 eV corresponding to the oxygen of V_2O_3. This feature can be assigned to ice. Upon heating the sample, this feature decreases and another feature at 532.5 eV arises, corresponding to OH groups.

All the results presented in this section therefore show a dissociative adsorption path leading to the formation of OH-groups. On the -V terminated surface, molecular water is still present on the surface. This may be compared with the $\alpha - Fe_2O_3(0001)$ (1×1) surface where theoretical calculations show that the most stable configuration of adsorbed water consists of roughly 70% dissociated and 30% molecular water [124]. This corresponds to a case where dissociated and molecular water have similar energies. There may still be molecular water on the -V=O surface (the feature at 11.2 eV has a shoulder on the high binding energy side) but in any case much less than for the -V surface.
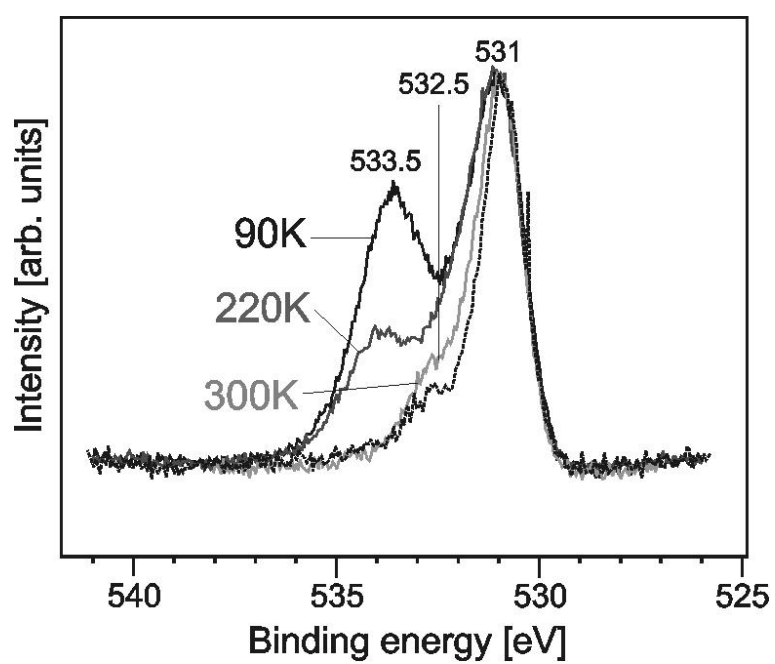
Figure 8.9: O 1s XP spectrum of 3L H$_2$O/O=V$_2$O$_3$(0001)/Au(111) at 90K and after heating the sample as indicated. The spectrum of the clean surface is shown (dashed curve)

8.4   Discussion

The results we have presented above are supposed to illustrate the trend we observed by making many experiments varying the experimental conditions. It seems to us that mainly two parameters govern the adsorption path - molecular or dissociative-, namely the surface termination and the quantity of water which has been adsorbed (or simply the fact that an ice multilayer has been formed or not).

The results presented in section 8.2 show that for low exposures, water adsorbs molecularly for both surfaces. In section 8.3, we showed that for larger exposures, only the -V=O terminated surface exhibits pure dissociative adsorption. On the -V surface, we found a mixture of OH groups and molecular water. Our experiments show that large water exposure on the -V=O surface always leads to dissociative water adsorption. For this reason, we want to concentrate first on this adsorption case.

If the activation barrier to dissociative adsorption is not too high, thermodynamic and not kinetic arguments shall predict whether or not dissociation of adsorbed water is favored, for any given surface. This can be done by means of an enthalpy diagram as displayed in figure 8.10. ΔH_f denotes the enthalpy of formation, ΔH_D the heat of desorption and ΔH_m and ΔH_d are the enthalpy of molecular adsorption and of dissociation, respectively. Dissociative adsorption occurs when ΔH_d is smaller than ΔH_m (as in the figure). In a three dimensional ice structure the water molecules are hydrogen bonded. The main components of the hydrogen bond are electrostatic forces, charge transfer, covalent forces, dispersion forces and exchange repulsion [127]. In the case of two hydrogen-bonded water molecules, the OH fragment of one molecule acts as acidic group and engages in a bond with an oxygen lone pair of the other molecule, which acts as basic group. One can therefore imagine that this hydrogen bonding weakens the internal O-H bond in the H_2O molecule and consequently decreases the enthalpy of dissociation ΔH_d. This shall explain why dissociative adsorption is favored by large water exposures. This phenomenon has been already observed and treated theoretically for water on MgO(100) [128].
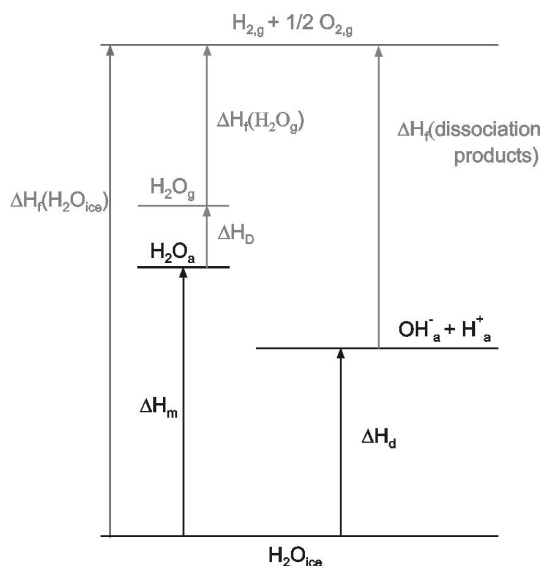
Figure 8.10: Enthalpy changes which accompany adsorption and dissociation of water, referenced to gas-phase hydrogen and oxygen (grey) and to ice (black)

When dissociative adsorption takes place on the **-V=O terminated** surface, charge transfer to the substrate V 3d is observed. The large shift of the O 2p we observe is due to the presence at the surface of the negative OH radicals. This origin of the shift is confirmed by the fact that it decreases when the OH-groups are partly desorbed at 350 K. When no more OH^- is present on the surface (at 550 K), the spectrum shows a very important change relative to the clean spectrum prior to water adsorption: the oxygen atoms of the vanadyl groups have desorbed with the OH-groups together. This signifies that these oxygen atoms were involved in the dissociation reaction of the water: $H_2O + O_{V=O}^{2-} \rightarrow 2OH^-$. One can therefore imagine a dissociative adsorption model on the -V=O terminated $V_2O_3(0001)$ surface as represented schematically on figure 8.11. It is there supposed that H_2O initially adsorbs on the surface vanadium through its oxygen atom. One hydrogen can then interact with the oxygen double bonded to the vanadium cation to form a OH radical when its bond to the water molecule is broken. It results in two OH^- groups, both bonded to the surface vanadium cation. This dissocia-
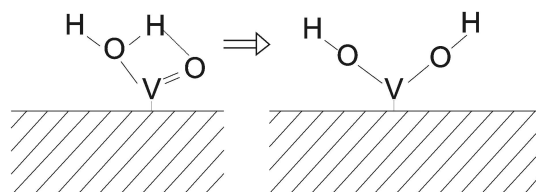
Figure 8.11: Model for the dissociative water adsorption on O=V$_2$O$_3$(0001). Only the surface vanadium and the oxygen of the vanadyl are shown

tion mechanism may imply charge redistribution, explaining why the V 3d emission increases upon water adsorption. If the formed OH radicals contain only a partial negative charge, there is a net charge-transfer back to the vanadium cation. This phenomenon has been already observed by Kurtz et al. on TiO$_2$(110) [129].

As mentioned above, the water does not completely dissociate on the **-V terminated** surface. For this surface, a charge transfer from the V 3d of the substrate to the adsorbate is observed, producing OH$^-$ radicals. The adsorption mechanism may be here quite different as for the V=O surface. Here the vanadium cation seems to act as a Lewis base (electron donor). After complete desorption of OH radicals and molecular water, the spectrum obtained shows no difference to the spectrum of the clean surface prior to the water adsorption (and for that reason it is not shown here). We can therefore suppose that if lattice oxygen is involved in the dissociative reaction path, then the OH$^-_{lattice}$ radicals dissociate before desorption. It is maybe more probable that water dissociates into OH$^-$ and H$^+$ groups. One can suppose that the substrate cation a$_{1g}$ or e$_g^{\Pi}$ orbital forms a σ bond with O lone-pair orbitals of OH$^-$. The observed charge transfer thus occurs along this bond.

Chapter 9

CO_2 Adsorption

9.1 Introduction

In this chapter, we present the results obtained upon CO_2 adsorption on both the -V=O and -V terminated $V_2O_3(0001)$ surfaces. CO_2 is a linear molecule with the carbon atom in the middle. Figure 9.1 shows the energy levels of the CO_2 molecular orbitals and their shape. Detectable by UPS are the four highest occupied molecular orbitals (HOMO): $4\sigma_g^+$, $3\sigma_u^+$, $1\pi_u$ and $1\pi_g$, as the photoelectron spectrum of CO_2 in the gas phase shown in figure 9.2 illustrates. Only the $1\pi_u$ of these four orbitals is binding. The other three are due to "lone pairs" which are located on the oxygen atoms.

9.2 Photoemission Spectroscopy

Figure 9.3 shows the UP spectrum of 20 L CO_2 on the **-V=O terminated** $V_2O_3(0001)/Au(111)$ and the difference spectrum obtained when the spectrum of the clean surface is subtracted from it. Three positive features are observed at 6.5, 10.4 and 11.9 eV and two small negative features just below the Fermi level (V 3d) and at the top of the O 2p band. As mentioned in section 9.1, four CO_2 orbitals are expected to be observed. A comparison with spectra of condensed CO_2 [130] leads one to make the assignment indicated on the figure. The intensity of the features corresponding to the adsorbed
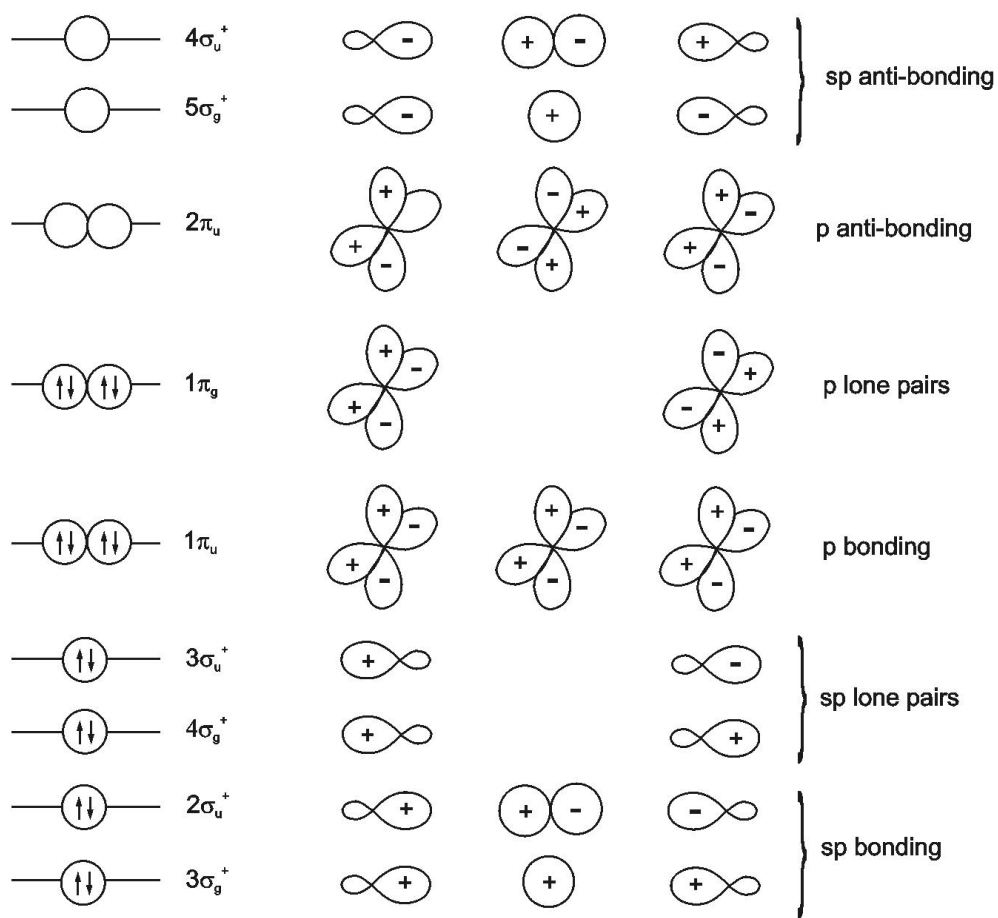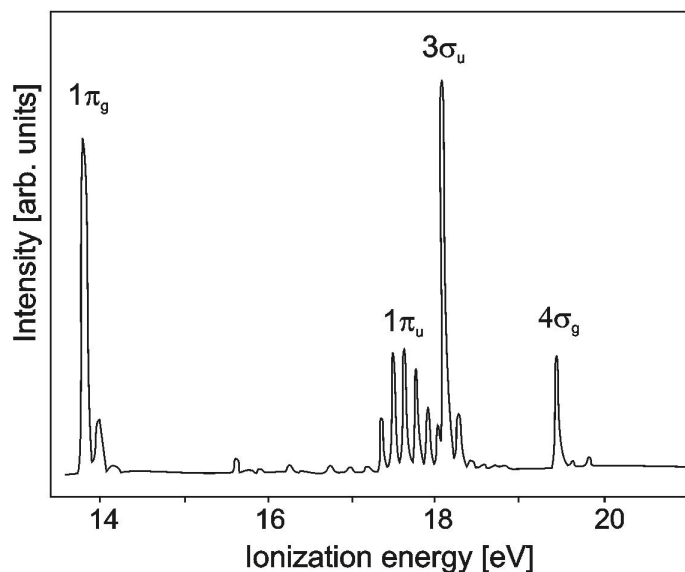
Figure 9.1: Molecular orbital diagram of CO$_2$

Figure 9.2: He I photoelectron spectrum of CO_2 in the gas phase (from [123])

species is very low, indicating that only a small quantity of CO_2 adsorbs on the surface. This weak physisorption on this surface is confirmed by the fact that heating the sample up to 115 K already leads to desorption of CO_2.

The **-V terminated** V_2O_3(0001)/Au(111) has been exposed to CO_2 at 90 K and then heated up to room temperature. Figure 9.4 shows the UP spectra obtained at different temperatures and the corresponding difference spectra. The first observation, in contrast to the spectrum obtained for the -V=O surface at 90 K, is that the features are much more intense, indicating adsorption of a larger quantity of CO_2. As for water adsorption discussed in chapter 8, the higher extra-molecular relaxation-polarization (EMRP) shift relative to the ionization energies of $CO_{2,gas}$ corresponds to the difference of work function between the two terminations. Note that the indicated ionizations energies are to be taken only in a qualitative manner since the features are quite broad and thus a deconvolution procedure can be only approximative. The spectrum at 115 K shows less intense features, indicating that the physisorbed CO_2 has already partly desorbed. New features seem to arise, which can be better visualized in the spectrum taken at 200 K when all the CO_2 has disappeared. Only these new features at 6.2, 10.6 and 13.2

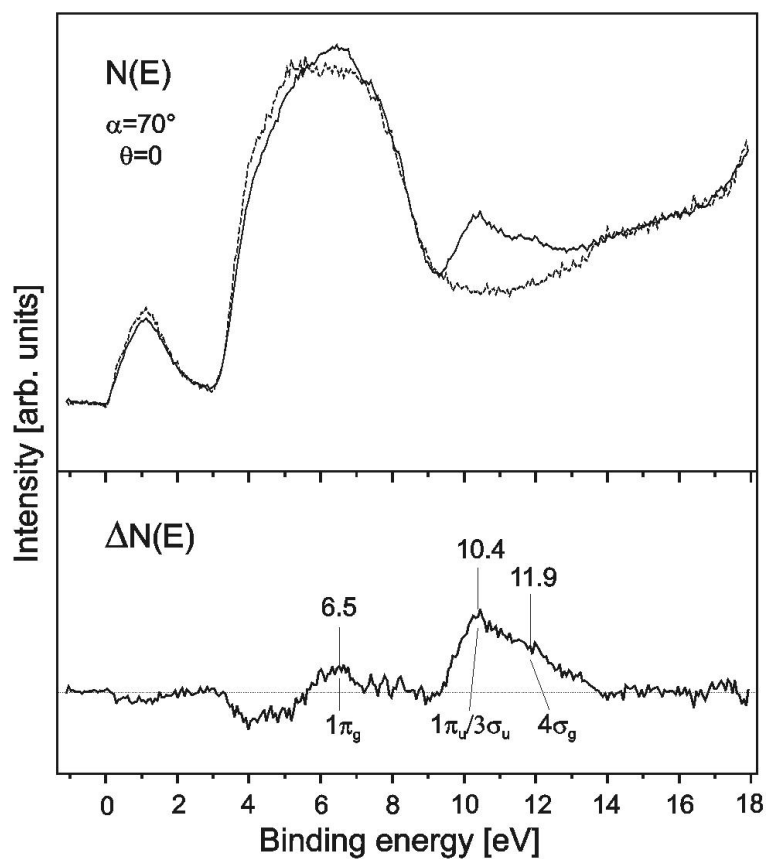Figure 9.3: He II UP spectra - Top: clean (dashed line) and 20 L CO$_2$/-V=O terminated V$_2$O$_3$(0001)/Au(111) (solid line) at 90 K. Bottom: corresponding difference spectra. α is the angle of incidence of light and θ is the detection angle
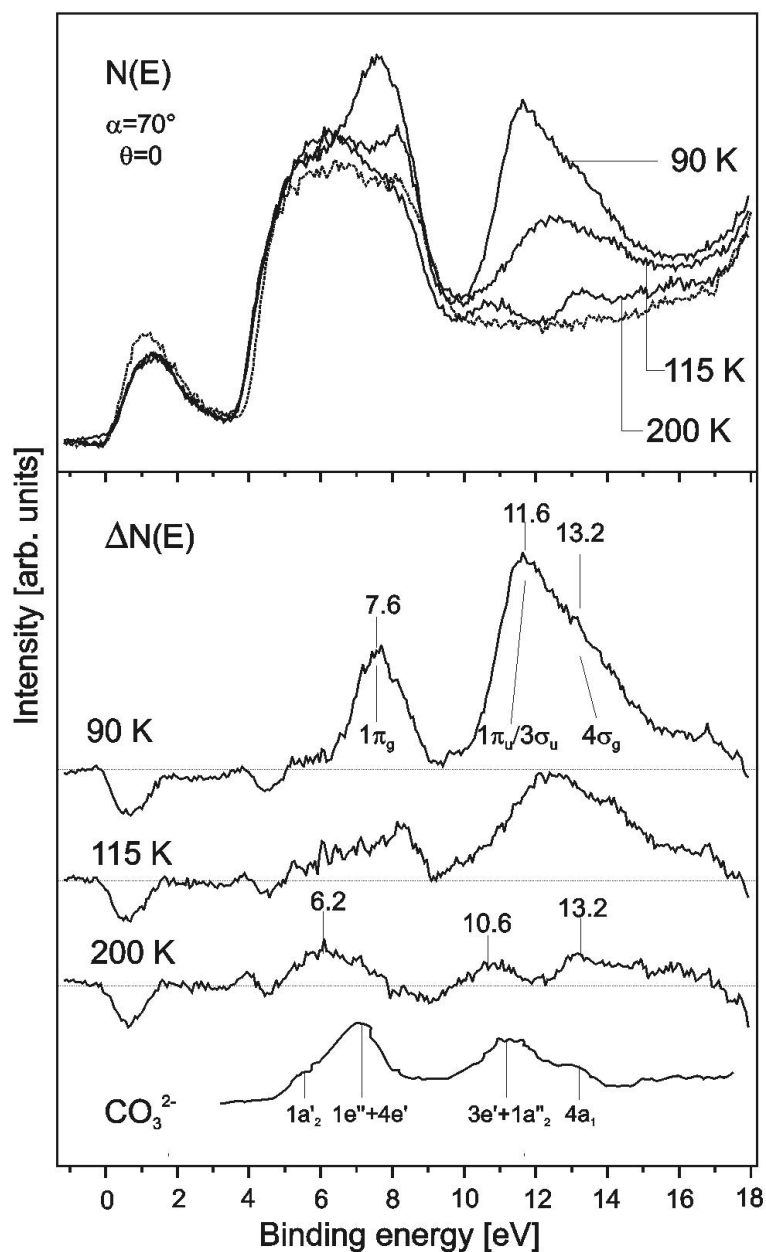
Figure 9.4: He II UP spectra - Top: clean (dashed line) and 20 L CO_2/-V terminated $V_2O_3(0001)$/Au(111) (solid line) at the temperatures indicated. Bottom: corresponding difference spectra. α is the angle of incidence of light and θ is the detection angle

eV remain. By comparing this spectrum with a HeII spectrum of K$_2$CO$_3$ from [131] shown in the bottom of figure 9.4 (the spectrum has been shifted of about 2 eV towards lower binding energies in order to align the features), we can assign the species present on the surface to carbonate ions CO$_3^{2-}$. Formation of carbonate from adsorbed CO$_2$ upon heating has already been observed for example on Pd(111) [132] and on Cr$_2$O$_3$(0001)/Cr(110) [104].

The XPS results for the same experiment as above on the **-V terminated** surface are presented in figure 9.5. O 1s spectra are to be seen on the top and C 1s on the bottom. Each O 1s spectrum exhibits a feature at 531 eV corresponding to the O 1s signal of V$_2$O$_3$ as discussed in chapter 5. Upon CO$_2$ adsorption at 90K, one feature at 535.5 eV shows up, which we can assign to physisorbed CO$_2$. Upon heating the sample, this feature decreases and another one arises at 532.5 eV, corresponding to carbonate. A similar feature has been found for carbonate on Cr$_2$O$_3$(0001)/Cr(110) [104]. The C 1s signal at 90 K consists of a relatively broad feature centered at 291.2 eV. Upon heating, two features are then to be seen at 290 and 291.7 eV. The first one increases and the latter decreases upon further heating. They can therefore be assigned to carbonate and physisorbed CO$_2$, respectively. This is in agreement with the results found in [104].

Figure 9.6 displays the results obtained upon CO$_2$ adsorption on an **O$_2$ precovered -V terminated** V$_2$O$_3$(0001) surface. The difference spectra correspond to the subtraction of the spectrum of the O$_2$ covered surface from the spectra of this surface exposed to CO$_2$. The spectrum of 20 L CO$_2$/O$_2$/-V V$_2$O$_3$(0001)/Au(111) at 90 K exhibits a slight band bending relative to the spectrum of the O$_2$ covered surface. This has been taken into account for the corresponding difference spectrum. The band bending is negligible for the spectrum at 140 K and has not been taken into account for the difference spectrum. The difference spectrum at 90 K shows similar features corresponding to physisorbed CO$_2$ as discussed above and the assignment to the CO$_2$ orbitals is also indicated. The spectrum at 140 K shows mainly the same features but less intense and shifted towards higher binding energies. This can be explained by the desorption of part of the physisorbed CO$_2$ and of the O$_2$, leading to a change of the work function. The small negative
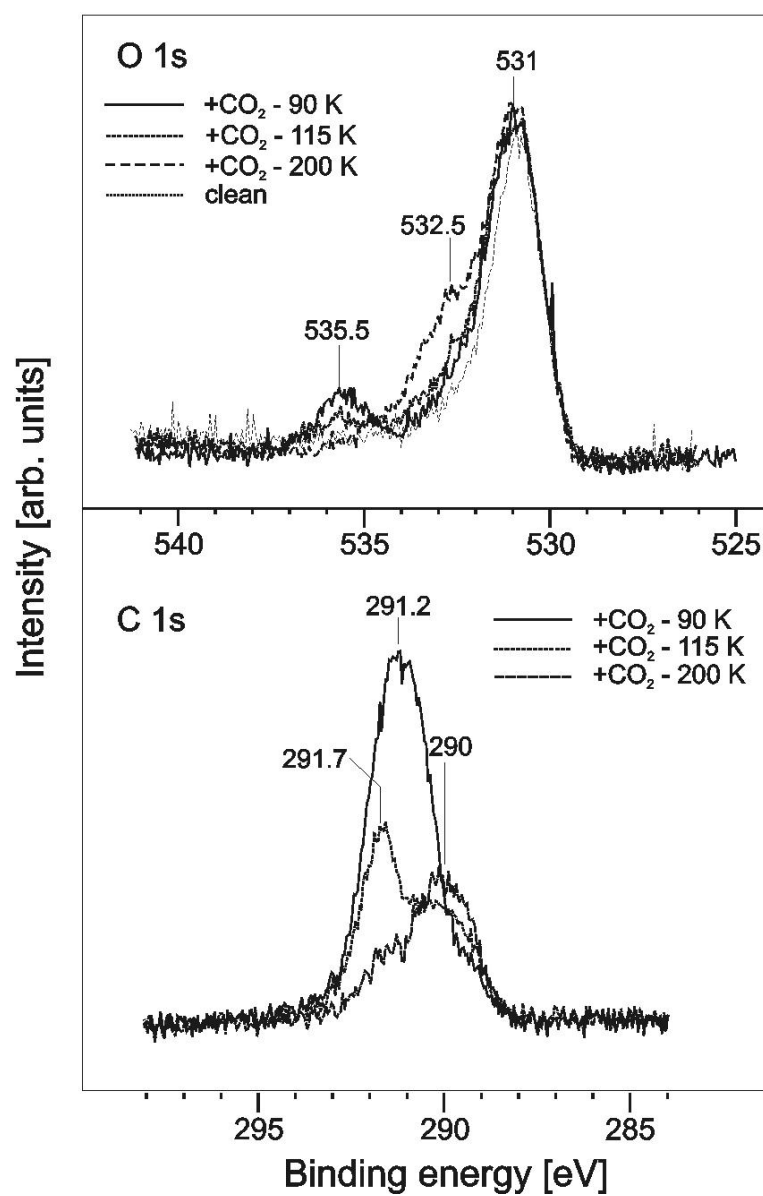
Figure 9.5: XP spectra of clean and 20 L CO_2/-V terminated $V_2O_3(0001)$/Au(111) at the temperatures indicated
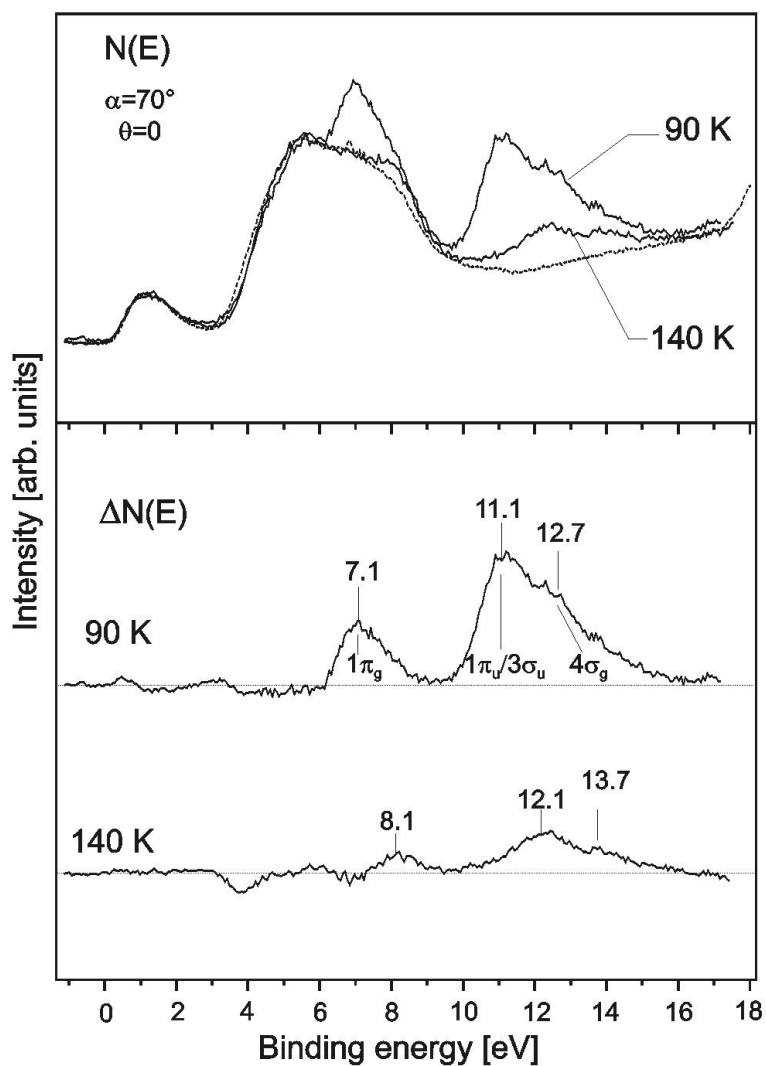
Figure 9.6: UPS HeII - Top: 20 L O$_2$/-V terminated V$_2$O$_3$(0001)/Au(111) (dashed line) and 20 L CO$_2$ on this O$_2$ precovered surface at the temperatures indicated. Bottom: corresponding difference spectra. α is the angle of incidence of light and θ is the detection angle
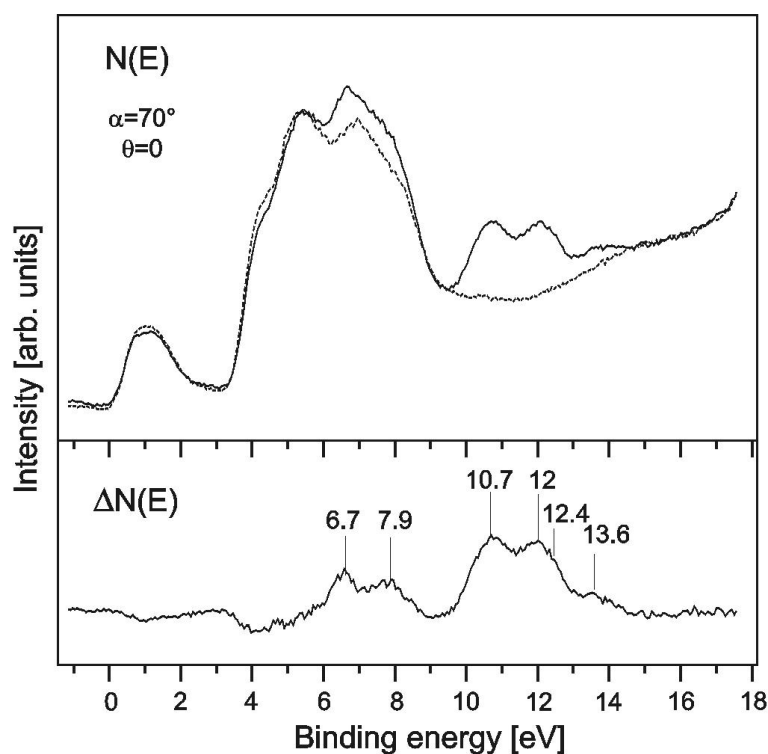
Figure 9.7: UPS HeII - Top: clean -V=O terminated $V_2O_3(0001)/Au(111)$ after 30 min. heating to 650 K without electron bombardment (dashed line) and 20 L CO_2 on this surface (solid line) at 90 K. Bottom: corresponding difference spectra. α is the angle of incidence of light and θ is the detection angle

feature at roughly 4 eV is probably due to a light persistent band bending. At 200 K, all the CO_2 and O_2 has desorbed and the spectrum corresponds to the spectrum of the clean -V terminated surface (not shown). The presence of O_2 therefore inhibits the formation of carbonate, as is the case for $Cr_2O_3(0001)/Cr(110)$ [104].

The role of the vanadyl groups on the adsorption of CO_2 can be also illustrated by the following experiment. We heated the sample to 650 K without electron bombardment (the temperature could not be higher because of the diffusion of gold from the substrate to the surface as discussed in section 5.2.3) and then performed CO_2 adsorption at 90 K. The obtained spectrum is
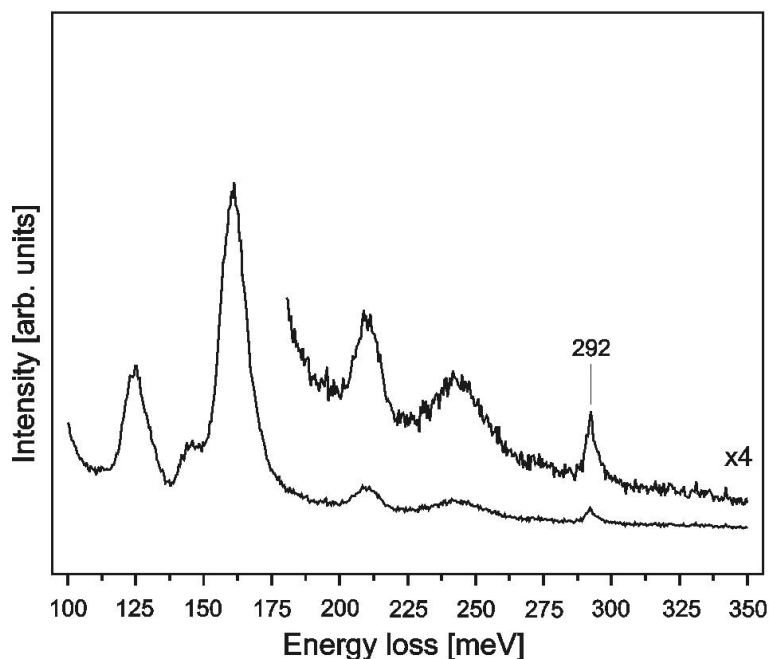
Figure 9.8:   HREEL   spectrum   of   50   L   CO$_2$/-V   terminated V$_2$O$_3$(0001)/W(110) at 90 K

shown in figure 9.7. The positive features in the difference spectrum actually are the same as in the previous figures but here they are twice and shifted relative to each other by approximately 1.2 eV. As discussed in section 6.4, we think that the removal process of the oxygen of the vanadyl groups, when the sample is heated by electron bombardment, is due mainly to desorption induced by electron transitions. By heating the surface without electron bombardment, the removal of the oxygen atoms can only occur through thermic desorption and this process might be very slow. Therefore, only a part of the vanadyl groups has been removed, yielding a heterogeneous surface. One then obtains two adsorbed species corresponding to the two terminations still available.
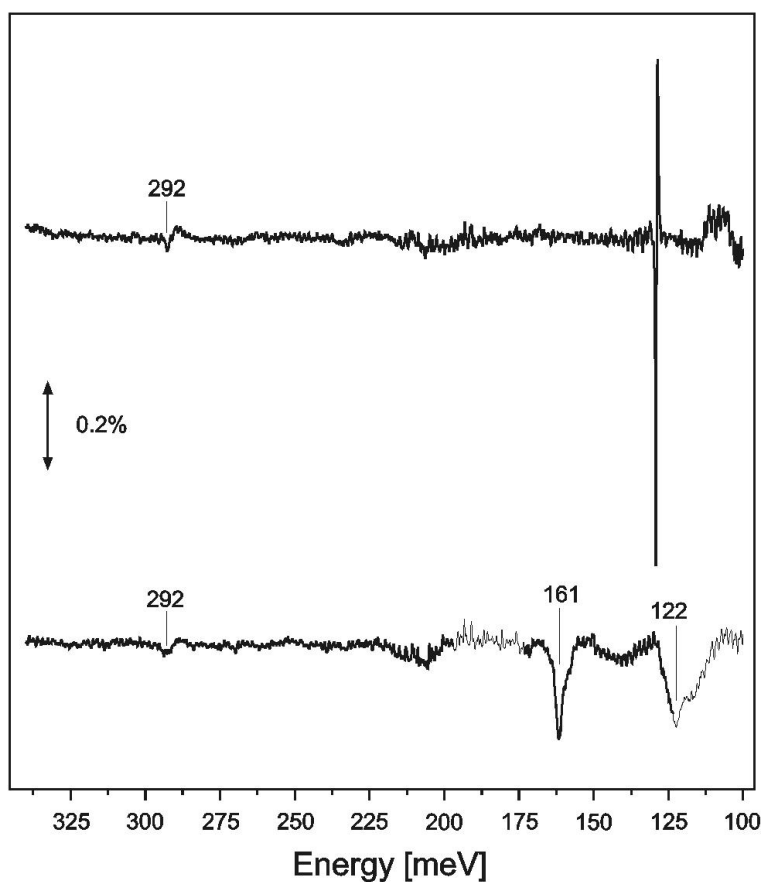
Figure 9.9: IRA spectrum of 50 L CO_2/-V=O terminated (top) and -V terminated (bottom) $V_2O_3(0001)$/W(110) at 90 K, referenced to the clean surface

9.3 Vibrational Spectroscopy

Figure 9.8 shows the HREEL spectrum obtained for the **-V terminated** $V_2O_3(0001)$/W(110) surface. As only a slight quantity of CO_2 adsorbs on the -V=O surface, no real feature could be detected by HREELS and thus the spectrum is not shown here. One feature at 292 meV (2352 cm^{-1}) assigned to physisorbed CO_2 can be seen on the figure. The other features are phonons as discussed in chapter 7. This feature at 292 meV corresponds to the asymmetrical stretch of the CO_2 molecule. Figure 9.9 displays the IR spectra obtained for both surfaces. One observes on both spectra a small

feature at 292 meV (2352 cm^{-1}) similar to that one observed with HREELS. The V=O stretching frequency exhibits a small shift toward higher binding energies, explaining the large and very narrow feature observed around 127 meV. This shift may be due to a change in the V=O bonding strength. More interesting are the two other features observed for the -V surface at 122 meV (983 cm^{-1}) and 161 meV (1297 cm^{-1}). The latter can be assigned to the symmetrical stretch of a bent $CO_2^{\delta-}$ species. As discussed in section 3.3.1, the symmetrical stretch frequency of a linear CO$_2$ molecule is not infrared active since this vibration has no changing dipole moment [40]. But this is not the case anymore for a bent molecule. A similar feature has been observed for CO$_2$/Cr$_2$O$_3$(0001)/Cr(110) [133, 101]. For such a bent CO$_2$ molecule, the asymmetrical C-O stretch frequency is expected around 199 meV (1600 cm^{-1}) [134]. No corresponding feature could be observed in our case. This suggests that the bent CO$_2$ molecule is oriented with its C$_{2v}$ axis perpendicular to the surface: the dynamical dipole moment for the asymmetrical stretch is along the O-O axis and so if this axis is parallel to the surface, the stretch frequency will not be detected by infrared. The symmetrical bend frequency is expected around 100 meV ($\simeq$ 800 cm^{-1}) and thus could not be seen with IRAS. The feature at 122 meV (983 cm^{-1}) may be assigned to a V-O stretching mode as observed for V-CO$_2$ complexes [135].

9.4   Discussion

The IRAS results show the formation of a bent CO$_2$ species upon CO$_2$ adsorption at low temperature on -V terminated V$_2$O$_3$(0001). This phenomenon has been frequently observed on single-crystal metal surfaces [136]. Note that the frequencies observed in the IRA spectra are consistent with carbonate. However, as carbonate is detected by UPS and XPS upon heating the sample and not already at 90 K, we instead assigned the features observed at 90 K to this bent CO$_2$ species. This species may be therefore a precursor of the formation of carbonate. This bent CO$_2$ species is formed by transferring electronic charge from the metal to the closed shell CO$_2$ molecule. The system then tends, according to the Walsh rules [137], to avoid a linear
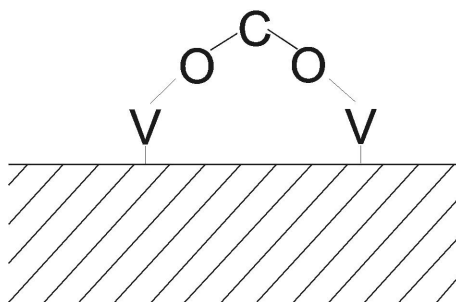
Figure 9.10: Schematical model of the adsorption of a bent CO_2 species on -V terminated $V_2O_3(0001)$

geometry. The additional charge is accommodated by the CO_2 molecule by breaking one of the two C-O double bonds and formation of an additional oxygen lone pair. The molecular orbital diagram then is slightly different than for a linear CO_2 molecule. One should therefore be able to observe changes in the UP spectra between the two adsorption configurations [138]. However, the UP spectrum we measured shows such large features that it is possible that the observed features correspond to linear CO_2 and CO_2 $^{\delta-}$. The negative feature just below the Fermi level observed in the difference spectra suggests that the charge transferred to the adsorbate comes from V 3d orbitals. This is not surprising since this $CO_2^{\delta-}$ species does not form on the -V=O surface, indicating that this is a result of an interaction with the V cation. The assignment of the feature at 122 meV (983 cm^{-1}) to a V-O stretching mode suggests that the molecule stands with the carbon atom on the top while the oxygen atoms interact with two vanadium cations. This model is schematically shown in figure 9.10.

The low intensity of the feature at 292 meV (2352 cm^{-1}) corresponding to physisorbed CO_2 compared to the IRAS measurements done on CO_2/$Cr_2O_3(0001)$/$Cr(110)$ [133, 101] can be explained either considering that only a small quantity of CO_2 remains in the linear form or that the molecule adsorbs nearly parallel to the surface. The changing dipole moment of the asymmetric stretch is then parallel to the surface also and therefore not infrared active.

Chapter 10

CO Adsorption

10.1 Introduction

Figure 10.1 shows a schematic molecular orbital diagram of the CO molecule. The three highest occupied molecular orbitals (HOMO) are the 4σ, 1π and 5σ. One observes features originating from these three orbitals in photoemission. Figure 10.2 displays the spectrum obtained for a CO molecule in the gas phase. Molecular adsorption of CO on transition metals involves electron transfer from the adsorbate to the surface along a CO 5σ-Me 3d bond. At the same time, the (anti-bonding) CO 2π orbital forms a π bond with Me 3d orbitals, allowing an electron transfer from the (occupied) Me 3d orbitals to the (unoccupied) CO 2π orbitals (reverse transfer or back-donation). Unlike the spectrum obtained for CO in the gas phase shown in figure 10.2, the photoemission spectrum obtained for CO adsorbed on transition metal generally shows only two features [24]. This arises from a shift of the CO 5σ orbital toward lower binding energies due to its σ bonding with a Me 3d orbital. Consequently, the 5σ and 1π orbitals are closely spaced and cannot be resolved in the photoemission spectrum. The stretching vibration frequency of adsorbed CO will depend on the relative contribution of σ- and π-bonding, which, in turn, depends on the state of the adsorption site (chemical nature, charge state, the character of bonding with ligands)[134].

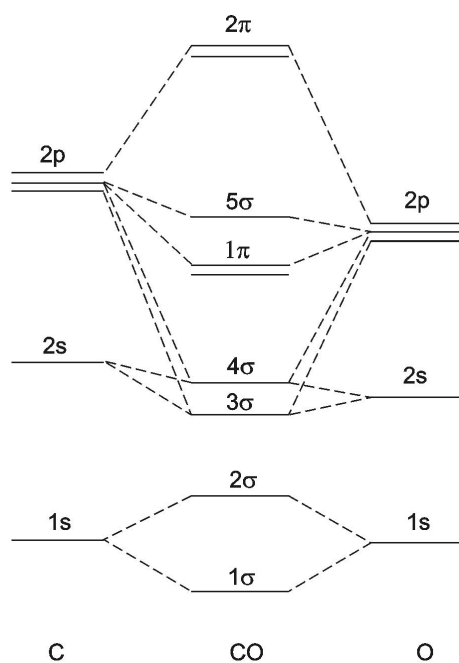Photoemission and vibrational spectroscopies are therefore good tools to

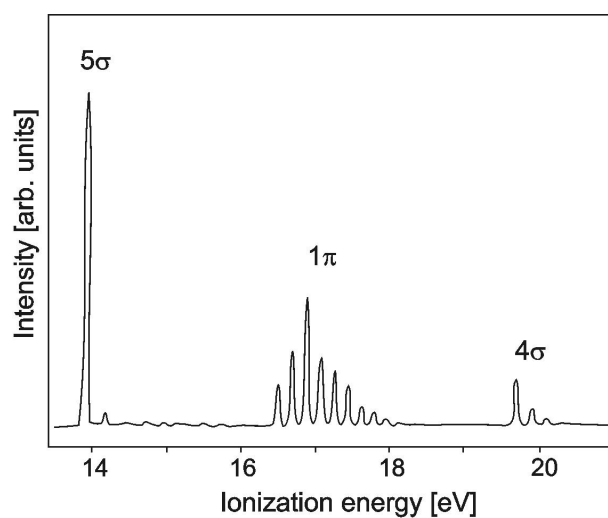Figure 10.1: Molecular orbital diagram of the CO molecule

Figure 10.2: He I photoelectron spectrum of CO in the gas phase from [123]

study the interaction of the adsorbed CO molecule with the metal oxide surface. We present in this chapter UPS, NEXAFS, HREELS and IRAS measurements performed on both the -V=O and -V terminated $V_2O_3(0001)$ surfaces.

10.2   CO Adsorption on the -V=O surface

Figure 10.3 shows the UP spectra obtained upon CO adsorption on the **-V=O terminated** $V_2O_3(0001)$/Au(111) surface at 90 K. The difference spectra created by subtracting the spectrum of the clean surface prior to the adsorption are shown in the bottom of the figure. One observes only two small features at 11 and 13.9 eV. No band bending occurs and only negligible negative features in the O 2p are observed. As stated in section 10.1, it is not unusual to observe only two features corresponding to the three HOMO of CO, since two of them can actually appear unresolved in one feature. The values found in the literature for CO on different substrates exhibit great variance. It is therefore difficult to make a valid comparison. Fukuda et al. [139] found three features for CO on Mg at 11, 13.2 and 15.7 eV that they assigned to the CO 5σ, 1π and 4σ orbitals, respectively. Didziulis et al. [140] found two features for CO on VC and TiC at 8.5 and 12.4 eV which they assigned to the $1\pi/5\sigma$ and 4σ levels, respectively. They found for TiC a supplementary feature at 15.9 eV that they attributed to a satellite peak typical of weakly adsorbed systems. Toledano et al. [141] found a broad feature at 10.9 eV for CO on Cr-doped $V_2O_3(0001)$. Referring to a previous work done on the isomorphic $Ti_2O_3(10\bar{1}2)$ which shows up two features at 10.8 and 7.8 eV, they assigned their feature at 10.9 eV to the CO 4σ. However, for $Cr_2O_3(0001)$/Cr(110) (also isomorphic to V_2O_3) two features at 11.8 and 14.3 eV were found[104, 142]. The authors assigned these features to the CO 5σ and $4\sigma/1\pi$ orbitals, respectively, pointing out the unusual state of adsorbed CO on $Cr_2O_3(0001)$ where the CO 1π level is closer to the 4σ than to the 5σ as generally observed.

The intensity of the observed features shows strong angular dependence. It can be shown that an oriented CO molecule exhibits a distinctive angular
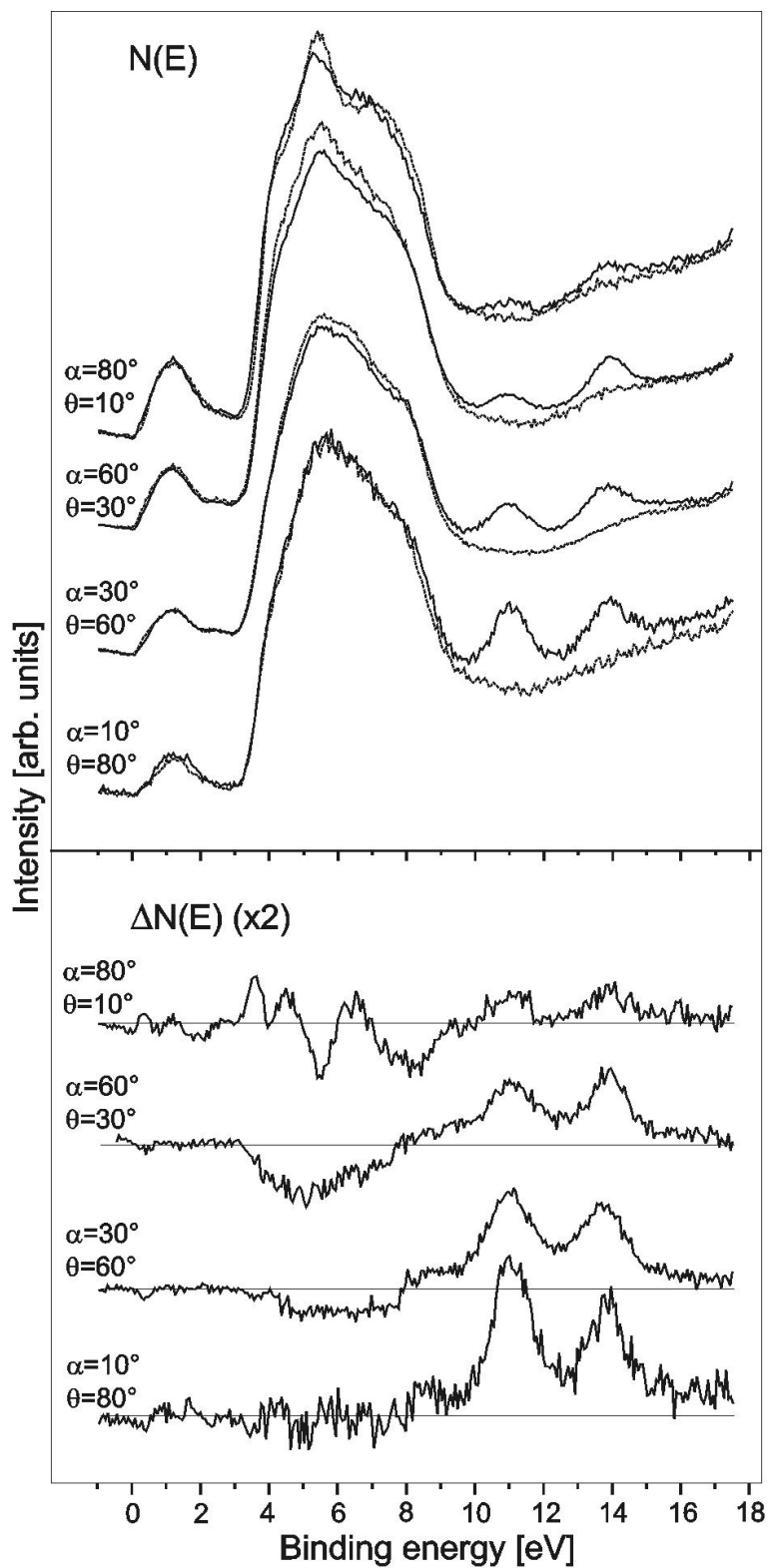
Figure 10.3: He II UP spectra. Top: 20 L CO/O=V$_2$O$_3$(0001)/Au(111) (solid line) and clean surface (dashed line) at 90 K. Bottom: difference spectra. α is the angle of light incidence and θ the angle of detection

distribution of the photoelectrons [143]: the photoemission from the 4σ and 5σ is maximum along the molecule axis when the light vector is parallel to this axis. For the emission from the 1π orbital, the maximum is found in a direction perpendicular to the molecule axis when the light vector is also perpendicular to the molecule axis. In each case, the maximum of emission is in the direction of the light vector, that is the reason why we had always $\alpha + \theta = 90^o$, α and θ being the angle of light incidence and detection, respectively. Nevertheless, the measurements here were performed with unpolarized light and thus one has to be careful when interpreting the data in terms of direction of the light vector. However, it is striking that both features at 11 and 13.9 eV have their maximum for $\alpha = 10^o$ and their minimum for $\alpha = 80^o$. This observation can be explained considering a CO molecule nearly parallel to the surface. The maximum of emission from both σ orbitals is then found for light coming nearly perpendicular to the surface. It should be emphasized that we suppose here that the CO molecule is in the incidence plane (i.e. oriented along one of the three axis of the oxygen hexagonal sublattice) and neglect the contribution in the photoemission signal of the two other possible orientations (along the two other axis). A question arises concerning the 1π orbitals and their corresponding features. As discussed in [104] for $CO/Cr_2O_3(0001)/Cr(110)$ where a strongly tilted adsorption geometry was proposed, the CO 1π orbital may split by interacting with the substrate in this geometry. These orbitals are two-fold degenerate in the gas phase but the interaction of one of these two orbitals with the surface will break the degeneracy. One may therefore expect one 1π orbital parallel to the surface and the other perpendicular to it. Neither of the observed features completely disappears by varying the light angle of incidence. This may suggest the presence of emission signal from 1π orbitals in these features. The maximum of their emission signal is expected when the light vector is perpendicular to the molecule axis, i.e. in our case for larger angle α. However, as one of the 1π orbitals is supposed to interact with the surface, this may alter the orbital in a way that these considerations are not longer valid.

Figure 10.4 shows a HREEL spectrum obtained for the **-V=O termi-nated** $V_2O_3(0001)$ surface exposed to CO at 90 K. One feature at 269 meV
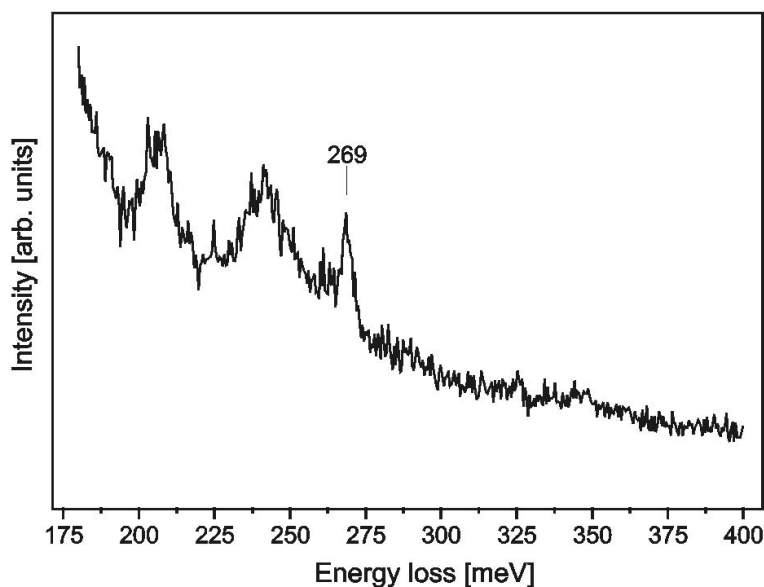
Figure 10.4: HREEL spectrum of 20 L CO/O=V_2O_3(0001)/W(110) at 90 K

(2166 cm^{-1}) arises upon CO adsorption. The two other features correspond to multiple loss phonons, as discussed in chapter 7. The CO stretching frequency is typical for adsorbed CO species on a transition-metal oxide surface. CO on reduced V^{3+} in V_2O_5 shows absorption around 270.5 meV (2180 cm^{-1}) [134].

10.3   CO Adsorption on the -V surface

Figure 10.5 displays the UP spectra obtained for the **-V terminated** surface for three different geometries. The corresponding difference spectra show three broad (not completely resolved) features at roughly 10.4, 12.9 and 15.2 eV. The emission of the whole O 2p band decreases upon adsorption while the V 3d band emission decreases just below the Fermi level (appearing as a small negative feature in the difference spectra). At variance with the -V=O surface, a large quantity of CO seems to adsorb on this surface. The intensity of the observed features is maximum for the smallest light angle of incidence (α), i.e. when the light vector is almost parallel to the surface. The observed angular distribution would consequently suggest that the CO
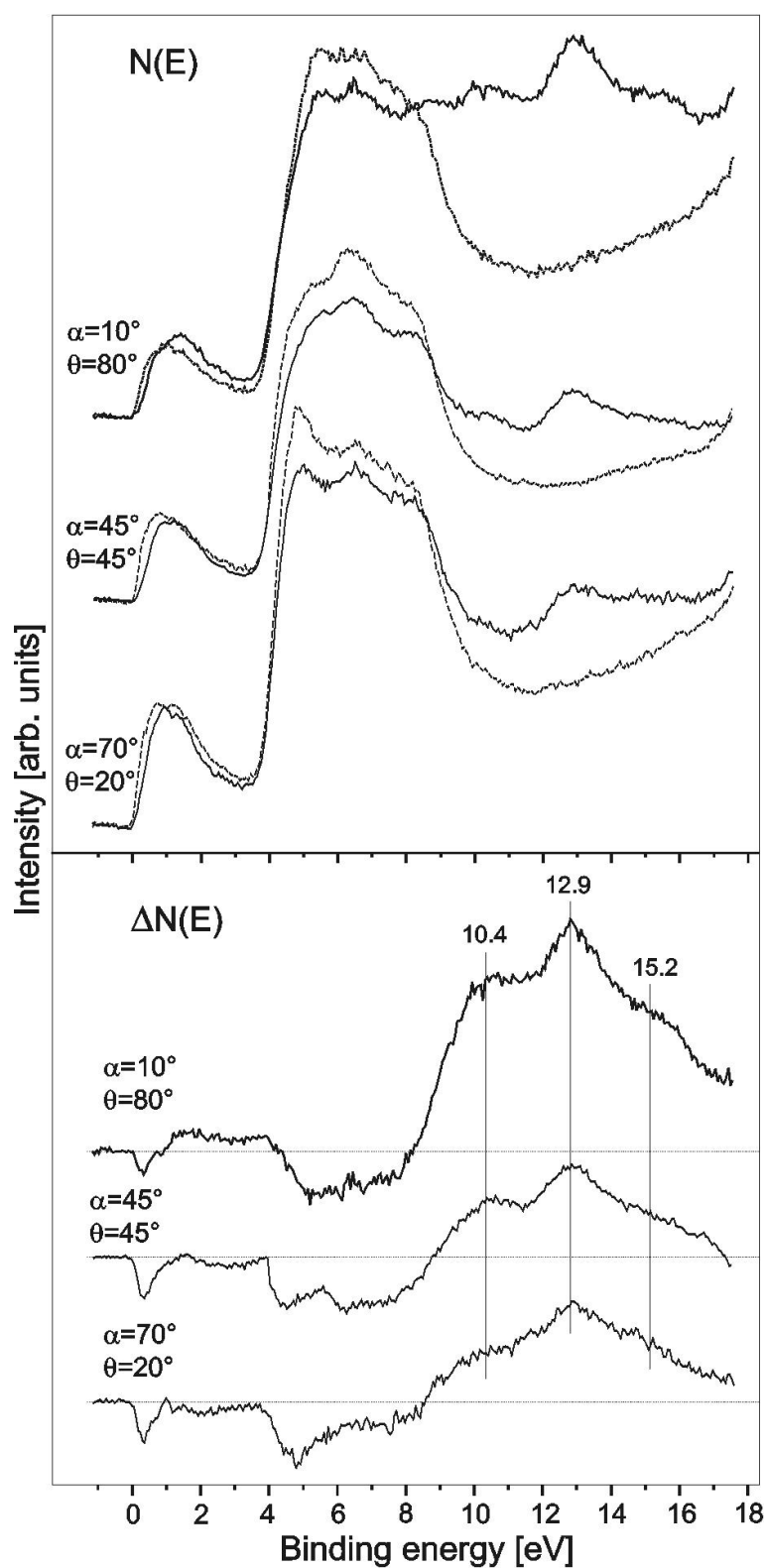
Figure 10.5: He II UP spectra. Top: clean (dashed line) and 20 L CO/-V terminated $V_2O_3(0001)/Au(111)$ (solid line) at 90 K. Bottom: corresponding difference spectra. α is the angle of incidence of light and θ the angle of detection
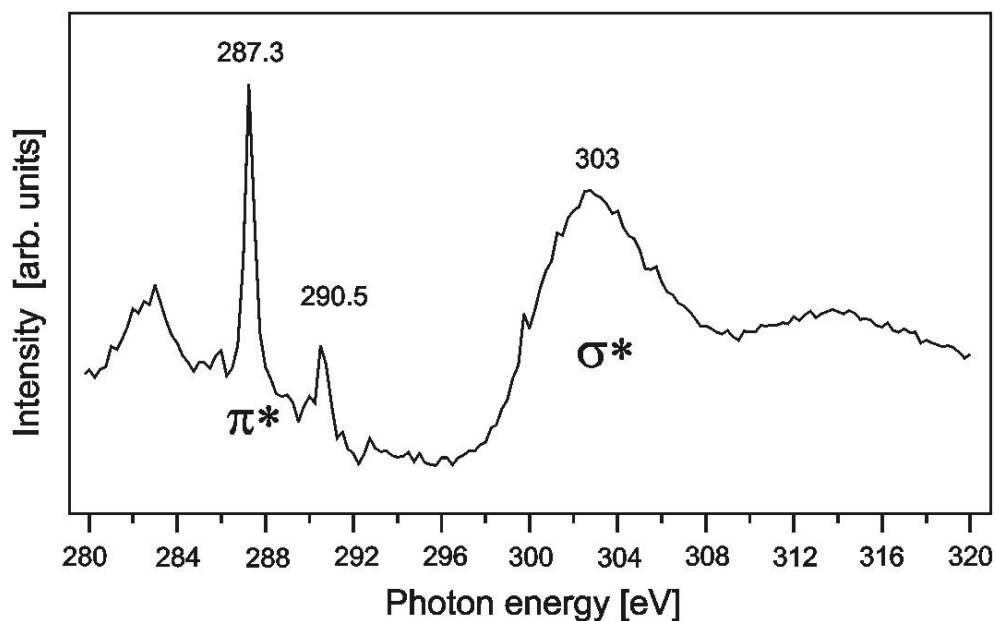
Figure 10.6: NEXAF spectrum of 20 L CO/-V terminated $V_2O_3(0001)/Au(111)$ taken in the Auger yield mode at 90 K and with light incident normal to the surface.

molecules are nearly parallel to the surface as for the -V=O surface discussed above. Nevertheless, as we will see with the next results, the assignment of the features observed in UPS for the -V surface is not really straightforward. One should therefore be careful with the interpretation of this angular dependence.

Figure 10.6 presents the NEXAFS result for CO on the -V terminated surface at 90 K. The feature at about 283 eV corresponds to photoelectrons originating from the V 4s level and is therefore not the object of our interest here. Two sharp features at 287.3 and 290.5 eV and a broader feature at about 303 eV are observed. The first one and the latter are typical for the π^* and σ^* resonance of the CO molecule, respectively [34]. The sharpness of the feature at 290.5 eV indicates that it corresponds to a π^* resonance. Comparing with NEXAFS data of CO_2 on $Cr_2O_3(0001)$ [104] or on Ni(110) [144], we can assign this feature to CO_2.

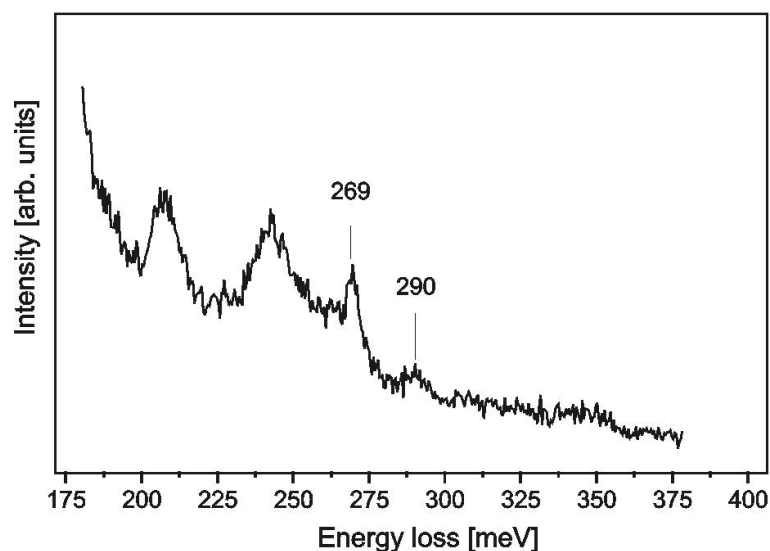The formation of CO_2 upon CO adsorption on -V terminated $V_2O_3(0001)$

Figure 10.7:   HREEL   spectrum   of   10   L   CO/-V   terminated
$V_2O_3(0001)/W(110)$ at 90 K

is confirmed by the HREELS result displayed in figure 10.7. One can see
there, in addition to the feature at 269 meV (2166 cm^{-1}), a feature at about
290 meV (2336 cm^{-1}) which we assign to CO_2. This is even more striking
when comparing those data to the IRA spectra presented in figure 10.8.
The feature at 290 meV is not to be seen -probably for the same reasons
as in the case of CO_2 adsorption discussed in chapter 9- but features at low
energy similar to those observed for CO_2 on -V $V_2O_3(0001)$ are obvious.
There, we found two features at 158 (1273 cm^{-1}) and 161 meV (1297 cm^{-1})
corresponding to the symmetrical CO stretch of the bent CO_2 molecule. This
suggests that there are two slightly different bent CO_2 species on the surface.
The features at 261.5 (2106 cm^{-1}) and 269 meV (2166 cm^{-1}) are assigned to
the adsorbed CO molecule. A new feature arises at 126.5 meV (1019 cm^{-1})
which remains at 165 K when no CO nor CO_2 is on the surface anymore.
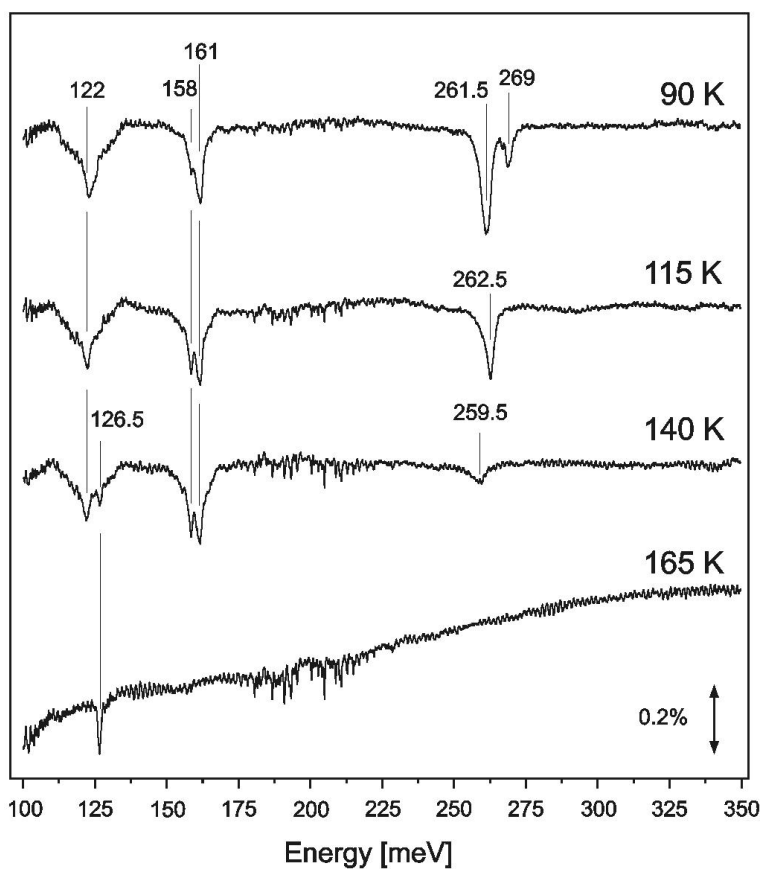This feature corresponds to a V=O species.

Figure 10.8: IRA spectrum of 50 L CO/-V terminated $V_2O_3(0001)/W(110)$ taken at the indicated temperatures

10.4 Discussion

The results presented in the previous sections show that CO adsorbs molecularly on the V=O surface. The features corresponding to the CO orbitals in the UP spectra show an angular dependence which we assign to a strongly tilted adsorption geometry. The case is much more complicated for the -V surface. We showed the formation on this surface of CO_2 that is in a bent configuration, as discussed in chapter 9. The resulting UP spectrum consequently shows unresolved features corresponding to the superposition of the signals coming from the different molecules present on the surface. At variance with the -V=O surface, negative features just below the Fermi level and in the whole O 2p band are observed in the UP difference spectra for the -V surface. This corroborates the assumption of the formation of a $CO_2^{\delta-}$ species. The formation of V=O upon heating and desorption of the CO and CO_2 also confirms the adsorption configuration of the bent CO_2 discussed in section 9.4 with the carbon atom on the top and the oxygen atoms interacting with the vanadium cations.

The question which arises at this stage is: how does the CO_2 molecule form? Does it form via the Boudouard equilibrium:

$$2CO \rightleftharpoons CO_2 + C \qquad (10.1)$$

or via reduction of the substrate:

$$CO + O_{lattice} \rightleftharpoons CO_2 \qquad (10.2)$$

The first possibility implies dissociation of CO, leading to carbon deposition on the surface. CO is found to dissociate on V(111) where the dissociation products remain on the surface above 200 K [145]. We could not detect the presence of carbon on the surface after CO adsorption. The second formation path should lead to changes of the electronic structure of the substrate detectable by UPS. Toledano et al. [141] observed a dramatic surface reduction of Cr-V_2O_3 upon CO adsorption at 300 K. We did not observe any change in the UP spectra between the clean surface prior to CO adsorption and after the adsorbate has been heated. Nevertheless, the feature at 261.5 meV (2106

cm^{-1}) that we measured by IRAS is not typical for metal oxides. This can be explained considering that a reduced V cation will have more electrons available for $2\pi^*$ back donation which in turn will decrease the CO bond strength and thus its stretch frequency. The feature at 261.5 meV therefore tends to prove that the CO_2 molecule forms via 10.2. However, interactions with other CO molecules of the adlayer and/or with the CO_2 molecules (or maybe with carbon atoms) can lead to shifts which are difficult to interpret properly due to the complexity of the situation. One should mention also the probable presence of defects on the surface which can always play an important role in adsorption experiments [6], for instance leading to shifts of the stretch frequencies [146]. Therefore, the formation path of the CO_2 molecule cannot be clearly determined.

Chapter 11

Summary

In this work, we firstly showed that it is possible to grow thin $V_2O_3(0001)$ films on Au(111) and W(110). The preparation process consists of an evaporation of metallic vanadium in an oxygen atmosphere, followed by an annealing at 700 K in 5.10^{-8} mbar of oxygen. The low energy electron diffraction (LEED) patterns obtained for both substrates exhibit sharp spots, indicating a well-defined surface structure. The stoichiometry of the film has been characterized by X-ray photoelectron spectroscopy (XPS) and near edge X-ray absorption fine structure spectroscopy (NEXAFS). The XP spectrum in the binding energy range 500-540 eV shows three features corresponding to the V $2p_{3/2}$, V $2p_{1/2}$ and O 1s lines, respectively. Relevant parameters for the determination of the stoichiometry of the oxide are the distance between the O 1s and V 2p signals, the Full Width at Half Maximum (FWHM) and the shape of the spectra. Our spectra show good agreement with those found in the literature for V_2O_3 single crystals. V L-edge NEXAFS spectra present noticeable chemical shifts characteristic of the different vanadium valencies and their shape depends implicitly on the local symmetry of the vanadium cation. Each vanadium oxide type therefore displays a typical spectrum. A comparison of our spectrum to reference spectra permits the identification of our vanadium oxide thin film to V_2O_3.

We inferred with infrared absorption spectroscopy (IRAS) the existence of two possible terminations of the $V_2O_3(0001)$ surface. These two terminations differ only by the presence or not of oxygen atoms on the top of the

surface, forming vanadyl groups with the surface vanadium atoms. The first termination, called -V=O termination, is obtained after the preparation process. The second termination - the -V termination - is obtained by heating the -V=O surface up to 600 K with electron bombardment.

We studied with UV photoelectron spectroscopies (UPS), XPS and NEXAFS the electronic structure of our $V_2O_3(0001)$ thin films. The UP spectra of the -V=O terminated surface clearly show a gap for the -V=O terminated surface. These data therefore evidence a metal to insulator transition induced by the formation of the vanadyl groups on the surface. This result is confirmed by our NEXAFS O K edge and XPS results. The NEXAF O K edge spectra consist of two features. The first one is attributed to the tansition to the unoccupied V 3d e_g^Π and a_{1g} (t_{2g}) states with O 2p character and the second one to the unoccupied V 3d e_g^σ states. For the -V=O termination, both features of the spectrum exhibit a shift towards higher energy relative to the spectrum for the -V termination. This shift can be explained by the changes in the electronic structure due to the metal to insulator transition. The XP spectra exhibit enhanced satellite features in the case of the -V=O termination, which can be attributed to poorly screened final states. We also observed a shift of the O 2p band towards lower binding energies for the -V=O terminated surface relative to the -V terminated surface. We tried to explain this phenomenon with a band bending model. Finally, we proposed two models for the surface geometry of the -V=O terminated surface. In the first one, the oxygen atoms sit on top of the vanadium atoms. In the second one, the oxygen atoms sit on quasi regular bulk positions.

We performed high resolution electron energy loss spectroscopy (HREELS) measurements and presented a phonon spectrum for each termination. Differences in phonon intensities observed between both surface terminations can be interpreted as a screening effect of electronic carriers. We compared our spectra with a spectrum of the isomorphic $Cr_2O_3(0001)$ and found out that the metal-oxygen bond is not so strong in V_2O_3 as in Cr_2O_3.

We studied the water adsorption properties of both surface terminations. The experiment consists of the adsorption of water at 90 K, yielding the formation of ice on the sample surface. The sample then is heated up to

190 K. The species present on the surface at this temperature are analyzed with UPS, XPS and HREELS. The adsorption path seems to depend on both the termination and the exposure. We observed molecularly adsorbed water on both surface terminations for low exposures. The adsorbed water shows only weak interaction with the substrate. For large exposures, water dissociates and OH^- groups were detected. When the OH^- desorb of the primary -V=O terminated surface, the surface left is -V terminated. In the case of the -V=O terminated surface, the water molecule is assumed to adsorb on the surface vanadium atom through its oxygen atom. The oxygen double bonded to the vanadium can interact with the hydrogen of the water molecule to form a OH radical, breaking its double bond to the vanadium. This dissociation mechanism may imply charge redistribution, explaining why the V 3d emission in UPS increases upon water adsorption. This model explains why the vanadyl oxygen atoms desorb with the OH groups. For the -V terminated surface, we observed a charge transfer from the V 3d substrate to the adsorbate, producing OH^- groups. Therefore, we proposed a model in which the vanadium a_{1g} or e_g^{Π} orbital forms a σ bond with oxygen lone-pair orbitals of OH^-.

We performed CO_2 adsorption experiments with UPS, XPS, HREELS and IRAS. The UP results for the -V=O surface exhibit small features which we assigned to physisorbed CO_2. The CO_2 adsorption on the -V terminated surface is more complex. The analyze of the IRAS results leads us to the conclusion that CO_2 adsorbs in a bent configuration. With UPS and XPS, we could evidence the formation of carbonates upon heating up to 200 K.

The CO adsorption properties follow a similar trend as for CO_2 : only small quantities adsorb on the -V=O surface while the -V surface seems to be much more reactive. On the -V=O surface, CO adsorbs molecularly and we concluded from the angle resolved UPS data that the CO molecule is strongly tilted on the surface. With NEXAFS and IRAS, we showed the formation of CO_2 on the -V surface.

To our knowledge, we are the first to report a surface effect resulting in a metal to insulator transition. This very complex phenomenon is very exciting for the surface scientist. Further work on $V_2O_3(0001)$ should therefore involve

theorists in order to explain properly why the formation of vanadyl groups on the surface induces a metal to insulator transition. A simulation of the angle resolved UPS data could determine which model for the surface geometry is correct. Further experimental work could be thermal desorption spectroscopy (TDS) and IRAS with isotopes in order to identify the formation path of CO_2 by CO adsorption on the -V terminated surface.

Appendix A

Vanadium Oxides

Figure A.1 displays the vanadium-oxygen phase diagram. The system vanadium-oxygen exhibits a multitude of discrete phases. Their stoichiometry can in an essential way influence their physical properties. In this appendix, we want to shortly present the crystal structure and main physical properties of the main phases.

A.1 VO

VO has a NaCl-like cubic structure as figure A.2 shows. This crystal structure remains the same in the region from $VO_{0.8}$ to $VO_{1.3}$. The conductivity of VO_x decreases as x increases. For constant x, the conductivity increases with the temperature but still exhibits semiconductor character [147].

A.2 VO$_2$

VO$_2$ experiences a metal-insulator transition at 340K.

Above the transition temperature, VO$_2$ is isomorphic to TiO$_2$, i.e. it has the rutile structure with the space group $P4_2|mnm$. The corresponding lattice structure is shown in figure A.3. The lattice constants for the tetragonal primitive cell are $a_R = 0.4551nm$ and $c_R = 0.2851nm$ [147]. The vanadium atoms sit in a octahedral oxygen environment. The octahedra share sides
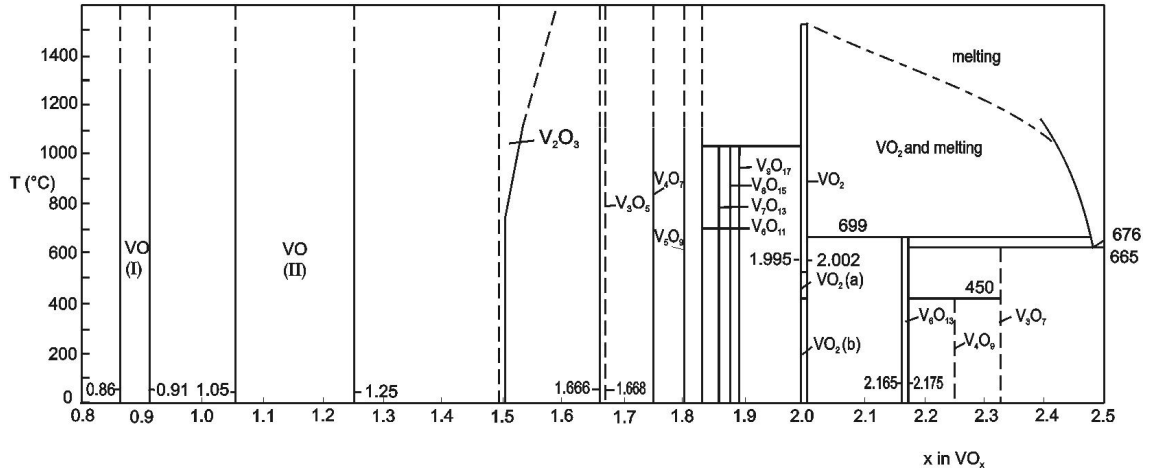
Figure A.1: Phase diagram of the system vanadium-oxygen (from [147])
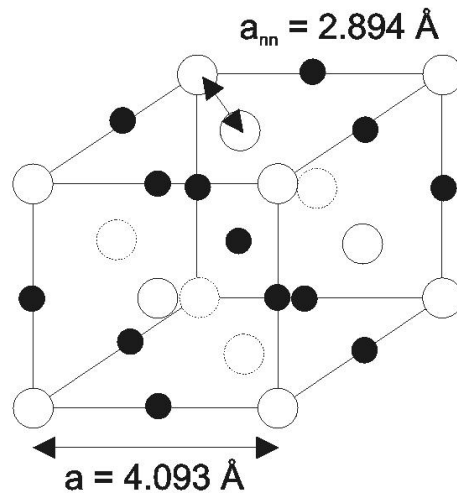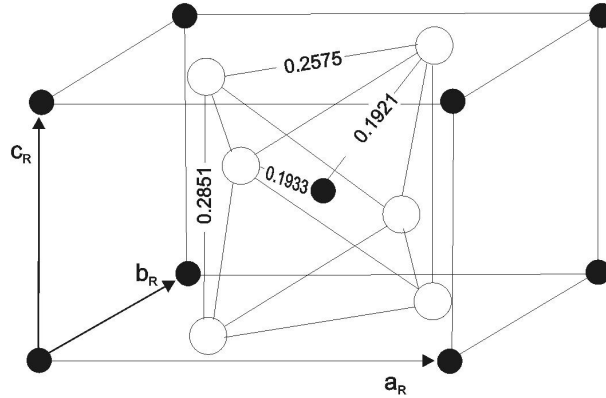

Figure A.2: Crystal structure of VO

Figure A.3: Crystal structure of VO_2

along the c_R axis and thus the shortest V-V distance is along that direction and is equal to $d_{V-V} = 0.2851 nm$.

Below the transition temperature, the tetragonal rutile structure distorts and becomes monoclinic, isomorphic to MoO_2 (space group $P2_1|c$). The size of the primitive cell is doubled. The compact packing of the oxygen atoms remains roughly the same through the transition. The main change concerns the vanadium atoms which move away from the center of the octahedra.

A.3   V₂O₅

Figure A.4 shows the lattice structure of V_2O_5. In principle, the vanadium atoms sit in the octahedral sites of a compact oxygen lattice. Each vanadium atom is surrounded by five oxygen atoms. These atoms form a distorted trigonal bipyramid. The orthorhombic lattice parameters are: a = 1.151 nm, b = 0.4369 nm and c = 0.3563nm. The V-O distances (corresponding to the numbering of figure A.4) are: V-O_1 = 0.158 nm, V-O_2 = 0.202 nm, V-O_3 = 0.178 nm, V-O_4 = 0.188 nm and V-O_6 = 0.278 nm.

V_2O_5 is a so-called d^0 oxide, that is to say that formally, no 3d electrons are present in the V 3d shells. The consequence is an insulating state, as discussed in chapter 2.
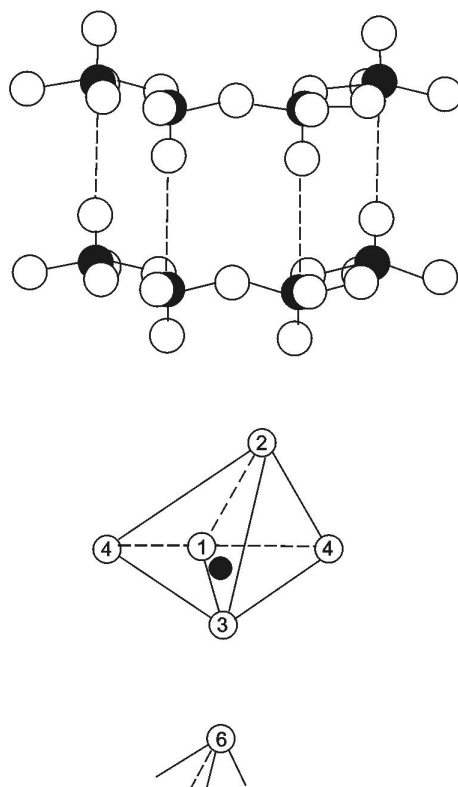
Figure A.4: Crystal structure of V_2O_5

A.4 $\mathbf{V}_n\mathbf{O}_{2n-1}$

In VO, V_2O_3, VO_2 and V_2O_5 vanadium has the formal valency 2,3,4 and 5, respectively. There are many oxides with mixed valency between V_2O_3 and V_2O_5. Their general formula is V_nO_{2n-1} and V_nO_{2n+1}. In these oxides, vanadium is in two different valency states at the same time. The oxides, corresponding to the formula V_nO_{2n-1} with $3 \leq n \leq 8$, are called the Magnéli phases. Except V_7O_{13}, each of them undergoes a metal-insulator transition [147]. The Magnéli phases are constituted by octahedral blocks which are connected through edges and sides as it is the case in the rutile structure. These rutile blocks are spread regularly in two directions through the crystal. They form layers in the third direction which are shifted relative to each other. Figure A.5 schematically illustrates this structure for the example of V_5O_9. These phases can be formulated by: $V_nO_{2n-1} = V_2O_3 + (n-2)VO_2$ with $3 \leq n \leq 8$.

A.5 $\mathbf{V}_n\mathbf{O}_{2n+1}$

There are three oxides between VO_2 and V_2O_5: V_6O_{13}, V_4O_9 and V_3O_7. Although they can be formulated by the general formula V_nO_{2n+1}, they do not exhibit structures analogous to the Magnéli phases. Here, we only want to present shortly the structure of V_3O_7.

V_3O_7 has a monoclinic crystal structure -space group $C2/c$- with twelve formula units per unit cell. 12 vanadium atoms are in a (distorted) octahedral environment, 16 are in trigonal bi-pyramids and 8 in quadratic pyramids. Figure A.6 shows the arrangement of VO_6 and VO_5-octahedra in V_3O_7. In the octahedra V1 and V2, vanadium is in the V^{4+} state, while its valency is +5 in the other polyhedra.
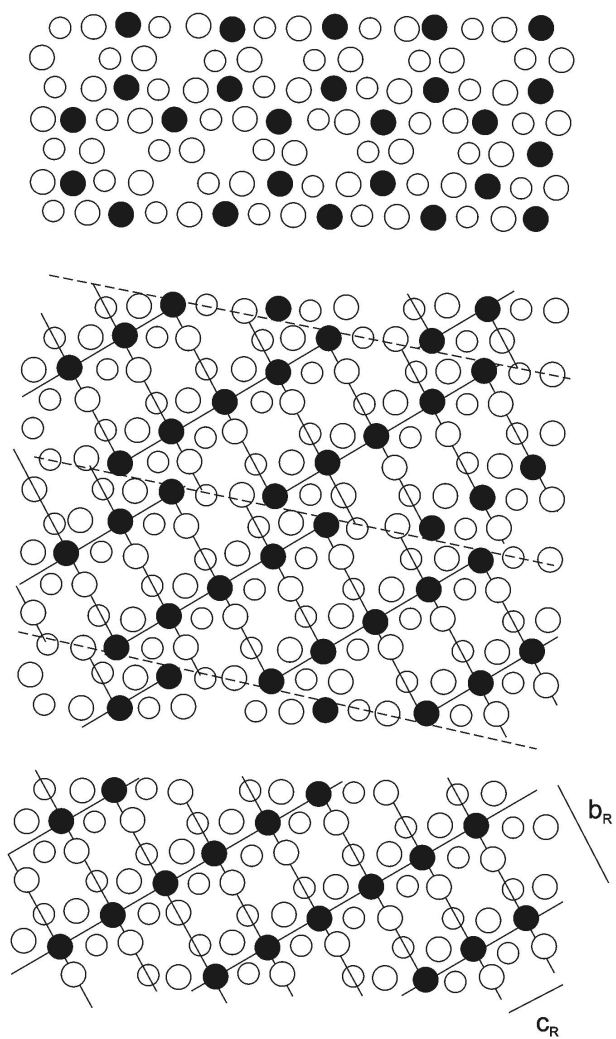
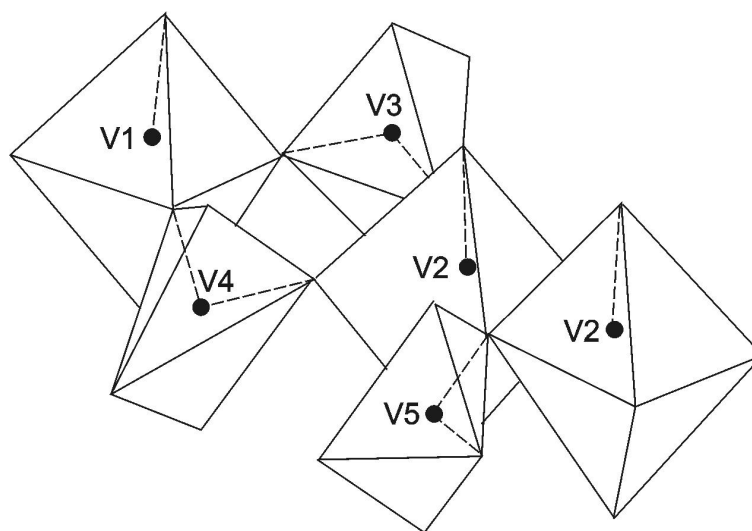Figure A.5: Schematic structure of V_2O_3 (top), V_5O_9 (middle) and VO_2 (bottom)

Figure A.6: Arrangement of VO_6-octahedra and VO_5-polyedra in V_2O_3

Appendix B

Zusammenfassung

Ziel dieser Arbeit war es, die Reaktivität von $V_2O_3(0001)$ zu untersuchen. Da V_2O_3 unterhalb von 150 K ein Isolator ist, wurden dünne Filme auf metallischen Substraten gezüchtet, um spektroskopische Methoden anwenden zu können. In dieser Arbeit wird sich zunächst mit dem epitaktischen Wachstum von V_2O_3-Filmen auf Au(111) und W(110) befaßt. Der Präparationsprozess besteht aus zwei Schritten: metallisches Vanadium wird zunächst in einer Sauerstoffatmosphäre aufgedampft, anschließend wird der Film bei 5.10^{-8} mbar Sauerstoffdruck und 700 K getempert. Stöchiometrie und Geometrie der dünnen Filme wurden mit Röntgenphotoelektronenspektroscopie (XPS), Röntgenabsorptionsspektroskopie (NEXAFS) und Beugung niederenergetischer Elektronen (LEED) charakterisiert. Wir haben gezeigt, dass die Oberfläche zwei Terminierungen aufweist, die sich durch die An- bzw. Abwesenheit von zusätzlichen Sauerstoffatomen auf der Oberfläche unterscheiden. Diese Sauerstoffatome bilden Vanadylgruppen mit den Oberflächenvanadiumatomen, deren Streckschwingung mit Infrarotabsorptionsspektroskopie (IRAS) detektiert werden kann. Die sogenannte -V=O terminierte Oberfläche erhielten wir nach dem oben erwähnten Präparationsprozess. Die -V terminierte Oberfläche ergibt sich aus der -V=O Oberfläche durch Heizen auf 600 K mit Elektronstoßheizung.

Die elektronische Struktur des $V_2O_3(0001)$ dünnen Filmes wurde mittels UV-Photoelektronenspektroskopie (UPS), XPS und NEXAFS untersucht. Wir haben bewiesen, dass die Bildung von Vanadylgruppen an der Oberfläche

einen Metall-Isolator Übergang hervorruft. Zwei Modelle für die -V=O Oberflächengeometrie wurden diskutiert.

Für jede Oberflächenterminierung wurde ein Elektronenenergieverlustspektrum (HREELS) gezeigt und mit einem Spektrum des isomorphischen Cr_2O_3 verglichen.

Wasseradsorptionsexperimente zeigen, dass Wasser sowohl molekular als auch dissoziativ auf beiden Oberflächen adsorbiert. Die Dissoziationswahrscheinlichkeit hängt von der Terminierung und von der Bedeckung ab. Sie ist am höchsten bei großer Bedeckung auf der -V=O Oberfläche.

CO_2 Adsorption wurde mit UPS, XPS, HREELS und IRAS untersucht. CO_2 physisorbiert auf der -V=O Oberfläche. Den IRA Spektren entnehmen wir, dass CO_2 auf der -V Oberfläche als gewinkelte $CO_2^{\delta-}$-Spezies adsorbiert. Heizen dieser Spezies auf 200 K führt zu Karbonatbildung.

Die Adsorption von CO verhält sich ähnlich wie die von CO_2: nur kleine Menge adsorbieren auf der -V=O Oberfläche, während die -V Oberfläche viel reaktiver zu sein scheint. Winkelaufgelöste UPS Messungen deuten auf eine flache CO Adsorptionsgeometrie auf der -V=O Oberfläche hin. NEXAF- und IRA-Spektren zeigen dagegen, dass bereits bei 90 K sich CO_2 auf der -V Oberfläche bildet.

Mit den präsentierten Experimenten konnten dünne Schichten von V_2O_3 auf Au(111) bzw. W(110) im Hinblick auf ihre geometrische und elektronische Struktur charakterisiert werden. Zudem konnten grundlegende Experimente zur Adsorption durchgeführt werden, die maßgeblich für die weitere Forschung an diesem System sind.

Bibliography

[1] J. Mendialdua, R. Casanova, and Y. Barbaux. *J. Electron Spectrosc. Rel. Phenom.*, 71:249–261, 1995.

[2] B. Tepper, B. Richter, A.-C. Dupuis, H. Kuhlenbeck, C. Hucho, P. Schilbe, M.A. bin Yarmo, and H.-J. Freund. *Surf. Sci.*, 496:64–72, 2002.

[3] I.V. Markov. *Crystal growth for beginners : fundamentals of nucleation, crystal growth and epitaxy.* World Scientific, 1995.

[4] J. A. Venables. *The Chemical Physics of Solid Surfaces*, volume 8 : Growth and properties of ultrathin epitaxial layers, pages 1–45. Elsevier, 1997. Edited by D.A. King and D.P. Woodruff.

[5] P.A. Cox. *Transition Metal Oxides : An Introduction to their Electronic Structure and Properties.* Clarendon Press - Oxford, 1992.

[6] V.E. Henrich and P.A. Cox. *The Surface Science of Metal Oxides.* Cambridge University Press, 1994.

[7] C. Cohen-Tannoudji, B. Diu, and F. Laloe. *Quantum mechanics.* Hermann and John Wiley & Sons, 1977.

[8] P. Schuster. *Ligandenfeldtheorie.* Verlag Chemie, 1973.

[9] P.W. Atkins. *Molecular Quantum Mechanics.* Oxford Univ. Pr., 3. edition, 1997.

[10] C. Noguera. *Physics and chemistry at oxide surfaces.* Cambridge University Press, 1995.

[11] M. Lannoo and P. Friedel. *Atomic and Electronic Structure of Surfaces.* Springer-Verlag, 1991.

[12] F.M.F. de Groot. *J. Electron Spectr. Rel. Phenom.*, 67:529–622, 1994.

[13] M. Imada, A. Fujimori, and Y. Tokura. *Rev. Mod. Phys.*, 70(4):1039, 1998.

[14] H. Ibach and H. Lüth. *Festkörperphysik.* Springer-Verlag, second edition, 1988.

[15] R. Hoffmann. *Solids and Surfaces : A Chemist's View of Bonding in Extended Structures.* VCH Publishers, 1988.

[16] O. Madelung. *Grundlagen der Halbleiterphysik.* Springer-Verlag, 1970.

[17] J. Zaanen, G.A. Sawatzky, and J.W. Allen. *Phys. Rev. Lett.*, 55:418, 1985.

[18] P.W. Tasker. *J. Phys. C:Solid State Phys.*, 12:4977, 1979.

[19] E. Durand. *Electrostatique et Magnétostatique.* Masson et Cie Editeurs, 1953.

[20] K. Kopitzki. *Einfürung in die Festkörperphysik.* B.G. Teubner Stuttgart, 1993.

[21] R. Fuchs and K.L. Kliewer. *Phys. Rev.*, 140:A2076–A2088, 1965.

[22] K. Hauffe and S.R. Morrison. *Adsorption.* Walter de Gruyter & Co., 1973.

[23] V.E. Henrich and P.A. Cox. *Appl. Surf. Sci.*, 72:277–284, 1993.

[24] S. Hüfner. *Photoelectron Spectroscopy : Principles and Applications.* Springer-Verlag, 1995.

[25] W. Ludwig and C. Falter. *Symmetries in Physics.* Springer-Verlag, 1988.

[26] H. Lüth. *Surfaces and Interfaces of Solids.* Springer-Verlag, 1993.

[27] G. Ertl and J. Küppers. *Low Energy Electrons and Surface Chemistry.* VCH Verlagsgesellschaft, 2., completely rev. edition, 1985.

[28] B.S. Wherrett. *Group Theory for Atoms, Molecules and Solids.* Prentice-Hall International, 1986.

[29] E.W. Plummer and W. Eberhardt. *Adv. Chem. Phys.*, 49:533, 1982.

[30] P.K. Ghosh. *Introduction to Photoelectron Spectroscopy.* John Wiley & Sons, 1983.

[31] R.J. Lad and V.E. Henrich. *Phys. Rev. B*, 38:10860, 1988.

[32] W. Eberhardt and F.J. Himpsel. *Phys. Rev. B*, 21:5572, 1980.

[33] G. Wendin. *Breakdown of the One-Electron Pictures in Photoelectron Spectra.* Springer-Verlag, 1981.

[34] J. Stöhr. *NEXAFS Spectroscopy.* Springer-Verlag, 1992.

[35] J.G. Chen. *Surf. Sci. Reports*, 30:1–152, 1997.

[36] F.M.F. de Groot, J.C. Fuggle, B.T. Thole, and G.A. Sawatzky. *Phys. Rev. B*, 42:5459, 1990.

[37] M. Abbate, H. Pen, M.T. Czyzyk, F.M.F. de Groot, J.C. Fuggle, Y.J Ma, C.T. Chen, F. Sette, A. Fujimori, Y. Ueda, and K. Kosuge. *J. Electron Spectr. Rel. Phenom.*, 62:185–195, 1993.

[38] H.-J. Freund and M. Neumann. *Appl. Phys. A*, 47:3–23, 1988.

[39] T. Gustafsson and E.W. Plummer. *Photoemission and the Electronic Properties of Surfaces*, chapter 12 : Valence Photoemission from Adsorbates. John Wiley & Sons, 1978. Edited by B. Feuerbacger, B. Fitton and R.F. Willis.

[40] C.E. Meloan. *Elementary Infrared Spectroscopy*. The Macmillan Compagny, 1963.

[41] J.T. Yates and T.E. Madey. *Vibrational Spectroscopy of Molecules on Surfaces*. Plenum Press, 1987.

[42] H. Ibach and D.L. Mills. *Electron Energy Loss Spectroscopy and Surface Vibrations*. Academic Press, 1982.

[43] H. Ibach. *J. Electron Spectrosc. Relat. Phenom.*, 64:819, 1993.

[44] M. Della Negra, M. Sambi, and G. Granozzi. *Surf. Sci.*, 436:227–236, 1999.

[45] M. Della Negra, M. Sambi, and G. Granozzi. *Surf. Sci.*, 461:118–128, 2000.

[46] K. Kishi and K. Fujiwara. *J. Electron Spectr. Rel. Phenom.*, 85:123–134, 1997.

[47] K. Kishi, Y. Hayakawa, and K. Fujiwara. *Surf. Sci.*, 356:171–180, 1996.

[48] M.A. van Hove, R.J. Koestner, P.C. Stair, J.P. Bibérian, L.L. Kesmodel, I. Bartoš, and G.A. Somorjai. *Surf. Sci.*, 103:189–217, 1981.

[49] K.H. Rieder, T. Engel, R.H. Swendsen, and M. Manninen. *Surf. Sci.*, 127:223–242, 1983.

[50] G.A. Sawatzky and D. Post. *Phys. Rev. B*, 20:1546, 1979.

[51] B. Richter. PhD thesis, Humboldt Universität Berlin, 2002.

[52] Z. Zhang and V.E. Henrich. *Surf. Sci.*, 321:133–144, 1994.

[53] R. Zimmermann, P. Steiner, R. Claessen, F. Reinert, S. Hüfner, P. Blaha, and P. Dufek. *J. Phys.: Condens. Matter*, 11:1657–1682, 1999.

[54] K.E. Smith and V.E. Henrich. *Phys. Rev. B*, 50:1382, 1994.

[55] A.E. Bocquet, T. Mizokawa, K. Morikawa, A. Fujimori, S.R. Barman, K. Maiti, D.D. Sarma, Y. Tokura, and M. Onoda. *Phys. Rev. B*, 53:1161, 1996.

[56] R.L. Kurtz and V.E. Henrich. *Phys. Rev. B*, 28:6699, 1983.

[57] G. van der Laan and I.W. Kirkman. *J. Phys.:Condens. Matter*, 4:4189–4204, 1992.

[58] S. Surnev, G. Kresse, M. Sock, M.G. Ramsey, and F.P. Netzer. *Surf. Sci.*, 495:91–106, 2001.

[59] H.-J. Freund, B. Dillmann, O. Seiferth, G. Klivenyi, M. Bender, D. Ehrlich, I. Hemmerich, and D. Cappus. *Cat. Tod.*, 32:1–10, 1996.

[60] B. Dillmann, F. Rohr, O. Seiferth, G. Klivenyi, M. Bender, K. Homann, I.N. Yakovkin, D. Ehrlich, M. Bäumer, H. Kuhlenbeck, and H.-J. Freund. *Faraday Discuss.*, 105:295, 1996.

[61] R.M. Moon. *Phys. Rev. Lett.*, 25:527, 1970.

[62] M. Altarelli. *J. Mag. Mag. Mat.*, 233:1–7, 2001.

[63] W. Bao, C. Broholm, G. Aeppli, S.A. Carter, P. Dai, T.F. Rosenbaum, J.M. Honig, P. Metcalf, and S.F. Trevino. *Phys. Rev. B*, 58:12727, 1998.

[64] J.W. Taylor, T.J. Smith, K.H. Andersen, H. Capellmann, R.K. Kremer, A. Simon, Schärpf, K-U. Neumann, and K.R.A Ziebeck. *Eur. Phys. J. B*, 12:199–207, 1999.

[65] C. Castellani, C.R. Natoli, and J. Ranninger. *Phys. Rev. B*, 18:4945, 4967 and 5001, 1978.

[66] L. Paolasini, C. Vettier, F. De Bergevin, F. Yakhou, D. Mannix, W. Neubeck, A. Stunault, M. Altarelli, M. Fabrizio, P.A. Metcalf, and J.M. Honig. *Physica B*, 281-282:485–486, 2000.

[67] M. Fabrizio, M. Altarelli, and M. Benfatto. *Phys. Rev. Lett.*, 80:3400, 1998.

[68] L. Paolasini, C. Vettier, F. De Bergevin, F. Yakhou, D. Mannix, A. Stunault, W. Neubeck, M. Altarelli, M. Fabrizio, P.A. Metcalf, and J.M. Honig. *Phys. Rev. Lett.*, 82:4719, 1999.

[69] W. Bao, C. Broholm, G. Aeppli, P. Dai, J.M. Honig, and P. Metcalf. *Phys. Rev. Lett.*, 78:507, 1997.

[70] P. Hertel and J. Appel. *Phys. Rev. B*, 33:2098–2113, 1986.

[71] V.A. Ivanov. *J. Phys.:Condens. Matter*, 6:2065–2076, 1994.

[72] S.Yu. Ezhov, V.I. Anisimov, D.I. Khomskii, and G.A. Sawatzky. *Phys. Rev. Lett.*, 83:4136–4139, 1999.

[73] J.B. Goodenough. *Prog. Solid State Chem.*, 5:145, 1971.

[74] I. Chatterjee. *J. Phys.:Condens. Matter*, 13:109–114, 2001.

[75] M. Catti, G. Sandrone, and R. Dovesi. *Phys. Rev. B*, 55:16122, 1997.

[76] M. Catti and G. Sandrone. *Faraday Discuss.*, 106:189–203, 1997.

[77] P.J. Brown, M.M.R. Costa, and K.R.A. Ziebeck. *J. Phys.:Condens. Matter*, 10:9581–9589, 1998.

[78] J.-H. Park, L.H. Tjeng, A. Tanaka, J.W. Allen, C.T. Chen, P Metcalf, J.M. Honig, F.M.F. de Groot, and G.A. Sawatzky. *Phys. Rev. B*, 61:11506, 2000.

[79] L.F. Mattheiss. *J. Phys.:Condens. Matter*, 6:6477–6484, 1994.

[80] J.C. Slater. *Phys. Rev.*, 82:538, 1951.

[81] N.F. Mott. *Phil. Mag.*, 6:287, 1961.

[82] F. Mila, R. Shiina, , F.-C Zhang, A. Joshi, M. Ma, V. Anisimov, and T.M. Rice. *Phys. Rev. Lett.*, 85:1714, 2000.

[83] R. Shiina, F. Mila, F.-C Zhang, and T. M. Rice. *Phys. Rev. B*, 63:144422, 2001.

[84] K.E. Smith and V.E. Henrich. *Phys. Rev. B*, 38:5965, 1988.

[85] R. Zimmermann, R. Claessen, F. Reinert, P. Steiner, and S. Hüfner. *J.Phys.: Condens. Matter*, 10:5697–5716, 1998.

[86] K.E. Smith and V.E. Henrich. *Solid State Comm.*, 68:29–32, 1988.

[87] S. Shin, S. Suga, M. Taniguchi, M. Fujisawa, H. Kanzaki, A. Fujimori, H. Daimon, Y. Ueda, K Kosuge, and S. Kachi. *Phys. Rev. B*, 41:4993, 1990.

[88] K.E. Smith and V.E. Henrich. *Phys. Rev. B*, 38:9571, 1988.

[89] K.E. Smith and V.E. Henrich. *J. Vac. Sci. Technol. A*, 6:831, 1988.

[90] E. Goering, M. Schramme, O. Müller, H. Paulin, M. Klemm, M.L. denBoer, and S. Horn. *Physica B*, 230-232:996–998, 1997.

[91] K. Hermann and M. Witko. *The Chemical Physics of Surfaces*, volume 9 : Oxide Surfaces, pages 136–198. Elsevier, New York, 2001. Edited by D.P. Woodruff.

[92] M. Demeter, M. Neumann, and W. Reichelt. *Surf. Sci.*, 454-456:41–44, 2000.

[93] V. Maurice, S. Cadot, and P. Marcus. *Surf. Sci.*, 458:195–215, 2000.

[94] T. Uozomi, A. Okada, R. Zimmermann, S. Steiner, Y. Tezuka, and S. Shin. *J. Electron Spectrosc. Relat. Phenom.*, 83:9–20, 1997.

[95] A. Fujimori, M. Saeki, N. Kimizuka, M. Taniguchi, and S. Suga. *Phys. Rev. B*, 34:7318, 1986.

[96] G. van der Laan, C. Westra, C. Haas, and G.A. Sawatzky. *Phys. Rev. B*, 23:4369, 1981.

[97] F.M.F. de Groot, M. Grioni, J.C. Fuggle, J. Ghijsen, G.A. Sawatzky, and H. Petersen. *Phys. Rev. B*, 40:5715, 1989.

[98] O. Müller, J.P. Urbach, E. Goering, T. Weber, R. Barth, H. Schuler, M. Klemm, S. Horn, and M.L. denBoer. *Phys. Rev. B*, 56:15056, 1997.

[99] H. Abe, M. Terauchi, M. Tanaka, and S. Shin. *Jpn. J. Appl. Phys.*, 37:584–588, 1998.

[100] K. Held, G. Keller, V. Eyert, D. Vollhardt, and V.I. Anisimov. *Phys. Rev. Lett.*, 86:5345, 2001.

[101] K. Wolter. PhD thesis, Technische Universität Berlin, 2001.

[102] C.A. Coulson. *Die chemische Bindung*. S. Hirzel Verlag Stuttgart, 1969.

[103] J.W. Gadzuk. *Phsy. Rev. B*, 10:5030–5044, 1974.

[104] C. Xu. PhD thesis, Ruhr Universität Bochum, 1991.

[105] R.D. Ramsier and J.T. Yates. *Surf. Sci. Rep.*, 12:243–378, 1991.

[106] P. Avouris and R.E. Walkup. *Annu. Rev. Phys. Chem.*, 40:173–206, 1989.

[107] G. Kotliar and G. Moeller. *Spectroscopy of Mott Insulators and Correlated Metals : proceedings of the 17th Taniguchi Symposium*, pages 15–27. Springer-Verlag, 1995. Edited by A. Fujimori and Y. Tokura.

[108] A. Fujimori, K. Morikawa, T. Mizokawa, T. Saitoh, M. Nakamura, Y. Tokura, I. Hase, and I.H. Inoue. *Spectroscopy of Mott Insulators and Correlated Metals : proceedings of the 17th Taniguchi Symposium*, pages 174–184. Springer-Verlag, 1995. Edited by A. Fujimori and Y. Tokura.

[109] A. Fujimori, I. Hase, H. Namatame, Y. Fujishima, Y. Tokura, H. Eisaki, K. Uchida, S. ad Takegahara, and F.M.F. de Groot. *Phys. Rev. Lett.*, 69:1796, 1992.

[110] A. Fujimori, I. Hase, Y. Tokura, M. Abbate, F.M.F. de Groot, J.C. Fuggle, H. Eisaki, and S. Uchida. *Physica B*, 186-188:981–985, 1993.

[111] K. Morikawa, T. Mizokawa, K. Kobayashi, A. Fujimori, H. Eisaki, S. Uchida, F. Iga, and Y. Nishihara. *Phys. Rev. B*, 52:13711, 1995.

[112] I.H. Inoue, I. Hase, Y. Aiura, A. Fujimori, Y. Haruyama, T. Maruyama, and Y. Nishihara. *Phys. Rev. Lett.*, 74:2539, 1995.

[113] I.L. Botto, M.B. Vassallo, E.J. Baran, and G. Minelli. *Mat. Chem. Phys.*, 50:267–270, 1997.

[114] A.S. Barker. *Phys. Rev.*, 132:1474–1481, 1963.

[115] H. Bialas and H.J. Stolz. *Z. Physik B*, 21:319–324, 1975.

[116] R. Cataliotti. *J. Chem. Phys.*, 72:3304–3308, 1979.

[117] H. Schober, T. May, B. Dorner, D. Strauch, U. Steigenberger, and Y. Morrii. *Z. Phys. B*, 98:197–205, 1995.

[118] D.R. Renneke and D.W. Lynch. *Phys. Rev.*, 138:A530–A533, 1965.

[119] G. Lucovsky, R.J. Sladek, and J.W. Allen. *Phys. Rev. B*, 16:4716–4718, 1977.

[120] G. Lucovsky, R.J. Sladek, and J.W. Allen. *Phys. Rev. B*, 16:5452–5459, 1977.

[121] S. Onari, T. Arai, and K. Kudo. *Phys. Rev. B*, 16:1717–1721, 1977.

[122] Q. Guo, D.Y. Kim, S.C. Street, and D.W. Goodman. *J. Vac. Sci. Technol. A*, 17:1887, 1999.

[123] K. Kimura, S. Katsumata, Y. Achiba, T. Yamazaki, and S. Iwata. *Handbook of He I photoelectron spectra of fundamental organic molecules*. Japan Scientific Societies Press, Tokyo, 1981.

[124] M.A. Henderson, S.A. Joyce, and J.R. Rustad. *Surf. Sci.*, 417:66–81, 1998.

[125] M.A. Henderson and S.A. Chambers. *Surf. Sci.*, 449:135–150, 2000.

[126] D.S. Toledano, P. Metcalf, and V.E. Henrich. *Surf. Sci.*, 472:21–32, 2001.

[127] P.A. Thiel and T.E. Madey. *Surf. Sci. Rep.*, 7:211–385, 1987.

[128] L. Giordano, J. Goniakowski, and J. Suzanne. *Phys. Rev. Lett.*, 81:1271, 1998.

[129] R.L. Kurtz, R. Stockbauer, T.E. Madey, E. Román, and J.L. De Segovia. *Surf. Sci.*, 218:178–200, 1989.

[130] J.-H. Fock, H.-J. Lau, and E.E. Koch. *Chem. Phys.*, 83:377, 1984.

[131] J.A. Connor, M. Considine, and I.H. Hillier. *J. Chem. Soc. Faraday Trans.II*, 74:1285–1291, 1978.

[132] J. Wambach, G. Odörfer, H.-J. Freund, H. Kuhlenbeck, and Neumann. *Surf. Sci.*, 209:159, 1989.

[133] O. Seiferth. PhD thesis, Ruhr Universität Bochum, 1997.

[134] A.A. Davydov. *Infrared Spectroscopy of Adsorbed Species on the Surface of Transition Metal Oxides*. John Wiley & Sons, 1984.

[135] J. Mascetti and M. Tranquille. *Surf. Sci.*, 156:201–205, 1985.

[136] H.-J. Freund and M.W. Roberts. *Surf. Sci. Rep.*, 25:225, 1996.

[137] A.D. Walsh. *J. Chem. Soc.*, pages 2260–2266, 1953.

[138] B. Bartos, H.-J. Freund, H. Kuhlenbeck, M. Neumann, H. Lindner, and K. Müller. *Surf. Sci.*, 179:59–89, 1987.

[139] Y. Fukuda and I. Toyoshima. *Surf. Sci.*, 158:482–489, 1985.

[140] S.V. Didziulis, P. Frantz, L.C. Fernandez-Torres, R.L. Guenard, O. El-bjeirami, and S.S. Perry. *J. Phys. Chem. B*, 105:5196–5209, 2001.

[141] D.S. Toledano, V.E. Henrich, and P. Metcalf. *J. Vac. Sci. Technol. A*, 18:1906–1914, 2000.

[142] C. Xu, B. Dillmann, H. Kuhlenbeck, and H.-J. Freund. *Phys. Rev. Lett.*, 67:3551–3554, 1991.

[143] J.W. Davenport. *Phys. Rev. Lett.*, 36:945–949, 1976.

[144] G. Illing, D. Heskett, E.W: Plummer, H.-J. Freund, J. Somers, Th. Lindner, A.M. Bradshaw, U. Buskotte, M. Neumann, U. Starke, K. Heinz, P.L. De Andres, D. Saldin, and J.B. Pendry. *Surf. Sci.*, 206:1, 1988.

[145] M. Beutl, J. Lesnik, E. Lundgren, C. Kovicka, P. Varga, and K.D. Rendulic. *Surf. Sci.*, 447:245–258, 2000.

[146] P. Hollins. *Surf. Sci. Rep.*, 16:51–94, 1992.

[147] W. Brückner, H. Oppermann, W. Reichelt, J.I. Terukow, F.A. Tschudnowski, and E. Wolf. *Vanadiumoxide*. Akademie-Verlag Berlin, 1983.